Faculty of Science
Department of Physics
Research Group Theoretische Materialphysik

Dissertation

zur Erlangung des akademischen Grades

Doktor der Naturwissenschaften
(Dr. rer. nat.)

Modelling Electron Exchange and Correlation for Catalyst Electronic Structure Simulations

by

SABUHI BADALOV

Paderborn, Germany
October 24, 2022

Promotionskommission

Vorsitzender: Prof. Dr. Tim Bartley [a]

Erstgutachter: Prof. Dr. Wolf Gero Schmidt [b]

Zweitgutachter: Prof. Dr. Simone Sanna [c]

Vertreter des Mittelbaus: Dr. Christof Eigner [d]

---

[a] Mesoscopic Quantum Optics, Department Physik, Universität Paderborn
[b] Theoretische Materialphysik, Department Physik, Universität Paderborn
[c] Institute for Theoretical Physics, Justus-Liebig-Universität Gießen
[d] Integrierte Quantenoptik, Department Physik, Universität Paderborn

Erklärung

Ich versichere, dass ich die Arbeit ohne fremde Hilfe und ohne Benutzung anderer als der angegebenen Quellen angefertigt habe und dass die Arbeit in gleicher oder ähnlicher Form noch keiner anderen Prüfungsbehörde vorgelegen hat und von dieser als Teil einer Prüfungsleistung angenommen worden ist. Alle Ausführungen, die wörtlich oder sinngemäß übernommen worden sind, sind als solche gekennzeichnet.

Virtus et Sapientia

Dedicated to
My Beloved Family!!!

Acknowledgements

Much like various types of exchange and correlation shape the collective response of a many-body system, having interactions with different people during my time at the University of Paderborn shaped me as a physicist. I am grateful to everyone who helped me throughout the doctorate, and so before starting with a discussion of modelling exchange and correlation of actual photocatalyst materials, I would like to thank everyone whose support made this the doctorate thesis formation.

First and foremost, the successful completion of this project would never have been possible without the guidance and support of my supervisor Prof. Dr Wolf Gero Schmidt has provided me with a great deal of knowledge, advice, and encouragement throughout the entire project. His broad knowledge and his logical way of thinking have great importance to me. During the last three and a half years with Gero, I have expanded my understanding of computational material physics and gained valuable experience with *ab initio* material modelling. I am incredibly grateful that he equipped me with all the resources required to maintain this research, and I am particularly indebted to his care in reading this manuscript. Besides all the support he gave me, his passion for science, insistence on long-term exploration, and patience with all students and researchers serve as the best example to all heads of the research groups.

Many thanks to my great thesis committee members; Prof. Dr Tim Bartley for having accepted to chair the jury of this thesis; Prof. Dr Simone Sanna for having accepted to review the manuscript and to participate in the jury of this thesis; Dr Christof Eigner for having accepted to be members of the jury of this thesis.

I also would like to thank our experimental cooperation partners at the Clausthal University of Technology, especially Prof. Dr René Wilhelm and his doctoral student Armin Meier for supplying me with new organic molecules' UV/Vis spectroscopy and other results.

I want to acknowledge Dr Uwe Gerstmann and Dr Timur Biktagirov for their support and fruitful discussions. Your deep understanding of computational physics helped me plan and carry out the calculations during my research study.

I would like to thank all past or recent members of our group "Theoretische Materialphysik", whom I have enjoyed working with, namely, Maximilian Kulke, Christian Braun, Hazem Aldahak, Agnieszka Kozub, Sergej Neufeld, Isaac Azahel Ruiz Alvarado, Adriana Bocchini, Lukas Meier, Falko Schmidt, Marvin Krenz, Mitisha Jain, Yannick Noel Freitag and Katharina Lorena Franzke for the scientific discussions, and who allowed me to fill the days with coffee and lunch breaks. I also thank Simone Lange (the best administrative assistant I have seen so far) for keeping the Department of Physics running through outstanding administrative work and helping me with all the other registration and forms, making me feel at home in Paderborn, Germany.

I gratefully acknowledge the following funding resources that support my research at the University of Paderborn from the Deutsche Forschungsgemeinschaft under project number: SCHM 1361/25. The simulation work was carried out using computational resources from the Paderborn Centre for Parallel Computing and the Höchstleistungs-Rechenzentrum Stuttgart.

Finally, I would like to thank my family. I want to mention my father Vatan, mother Dilafruz and my

sister Fidan who supported me throughout my studies and during my doctoral studies. I am grateful to my son Mustafa for being such a joyful and cheerful child and motivating me to finalise my doctorate in three and a half years. I also would like to thank my caring and lovely wife Aysel, for all her love, moral support and especially for taking over the parenting responsibilities in the final stage of the doctorate when I was writing my thesis.

Zusammenfassung

Aufgrund ihres hohen Oberflächen-Volumen-Verhältnisses sind nanostrukturierte Metalloxide und ihre Verbundwerkstoffe mit kohlenstoffbasierten niedrigdimensionalen Materialien und organischen Molekülen vielversprechend für den Einsatz in verschiedenen industriellen Anwendungen wie Photokatalyse, Photovoltaik und Sensoren. Für viele industrielle Anwendungen ist das theoretische Materialdesign auf atomarer Ebene kostengünstiger, sauberer und effizienter als experimentelle Techniken. Moderne Implementierungen mit Methoden, die auf der Dichtefunktionaltheorie basieren, ebnen den Weg für die Entdeckung und Entwicklung neuer Materialien. Diese Berechnungen ermöglichen die Erforschung und Vorhersage zahlreicher Eigenschaften und grundlegender wissenschaftlicher Phänomene. Die Modellierung auf atomarer Ebene und die Verbesserung der elektronischen Struktur durch das Vorhandensein neuer Elemente oder die Bildung von Defekten sowie die Umwandlung von Volumenmaterialen in Nanostrukturen sind entscheidende Schritte bei der Entwicklung effizienter industrieller Materialien. Die bei der Modellierung auf atomarer Ebene verwendeten Näherungsfunktionale haben jedoch eine begrenztere Gültigkeit als die konzeptionell exakte Dichtefunktionaltheorie. Daher ist es von entscheidender Bedeutung, effiziente und genaue theoretische Ansätze zu finden und zu entwickeln, die sich für die Untersuchung ähnlicher Systeme eignen, die im Mittelpunkt zahlreicher chemiscker Reaktionen stehen.

In dieser Arbeit werden die effizienten und genauen Elektronenaustausch- und Korrelationsansätze zur Verminderung des Wechselwirkungsfehlers innerhalb der Dichtefunkionaltheorie für Titan, Titan-Graphen-Verbundwerkstoffe und organischen Molekülen Katalysatorsystemen ermittelt und untersucht. Zu diesem Zweck habe ich mich hauptsächlich auf Hybridfunktionale, die Hubbard-Korrektur und die eingeschränkte Dichtefunktionaltheorie konzentriert. Zunächst werden die Auswirkungen und die Rolle von Hubbard U und hybriden Funktionsansätzen bei der Beschreibung der strukturellen, elektronischen und optischen Eigenschaften der drei Hauptphasen von TiO_2-Kristallen vorgestellt. Die Kombination von großmaßstäblicher elektronischer Strukturmodellierung mit zielgerichteten Ansätzen wurde vorgeschlagen, um ungeordnete Systeme über Titandünnschichten zu untersuchen. Als nächstes wurden die elektronischen und Anregungseigenschaften der Titancluster und ihrer Graphenkomposite mit Hilfe der "Constrained" Dichtefunktionaltheorie untersucht. Es wurde festgestellt, dass die elektronische Struktur und insbesondere die Anregungsenergien der nackten Cluster und der Titanoxid/Graphen-Komposite in Abhängigkeit von der Größe der jeweiligen Bestandteile erheblich variieren. Dies gilt insbesondere für die Energie und die räumlichen Lokalisationen der höchsten besetzten und niedrigsten unbesetzten Molekülorbitale. Neben einer erheblichen Verengung der Bandlücke wird in einigen Fällen eine ausgeprägte Trennung von photoangeregten Elektronen und Löchern vorhergesagt. Schließlich wurde eine Reihe neuer organischer Donor-π-Akzeptorfarbstoffe mit Hilfe von bereichsgetrennten hybriden Austauschkorrelationsfunktionen in der Dichtefunktionaltheorie und der zeitabhängigen Dichtefunktionaltheorie untersucht. Diese Studie bestätigt, dass sie ein intramolekulares Ladungstransferverhalten aufweisen. Darüber hinaus wird die überragende Leistung der bereichsgetrennten Hybridfunktion bei der Beschreibung der Anregungseigenschaften dieser Moleküle mit anderen Austausch-Korrelationsfunktionen und Experimenten verglichen. Insgesamt wird gezeigt, dass Hybridfunktionale, Hubbard-Korrektur und eingeschränkte Dichtefunktionaltheorie-Ansätze erfolgreich eingesetzt werden können, um das Standard-Austausch-Korrelationsfunktional, das im Dichtefunktionalrahmen verwendet wird, zu ergänzen.

Abstract

Owing to their high surface-to-volume ratio, nanostructure metal oxides and their composites with carbon-based low-dimensional materials and organic molecules have a great deal of promise for usage in various industrial applications such as photocatalysis, photovoltaics, and sensors. For many industrial applications, theoretical atomic-scale material design is more cost-effective, cleaner and more efficient than experimental techniques. Modern implementations with methods based on the density-functional theory pave the way for discovering and developing new materials. These calculations enable the exploration and prediction of numerous characteristics and fundamental scientific phenomena. Atomic-scale modelling and improvement of the electronic structure by the presence of new elements or the formation of defects and the conversion of bulk materials to nano-structures are critical steps in developing efficient industrial materials. However, the approximate functionals used in atomic-scale modelling have more limited validity than the conceptually exact density-functional theory. Hence, it is essential to identify and develop efficient and accurate theoretical approaches suitable for studying similar systems at the heart of numerous vital reactions.

In this thesis, the efficient and accurate electron exchange and correlation approach to avoid density-functional theory's erroneous behaviours related to the self-interaction error are identified and investigated for titanium, titanium graphene composite, and organic molecular catalyst systems. Following this objective, the focus lies mainly on hybrid functionals, Hubbard correction, and constrained density-functional theory. First, the effect and role of Hubbard U and hybrid functional approaches in describing the structural, electronic, and optical properties of the three major phases of TiO_2 crystals are presented. The combination of large-scale electronic structure modelling with pinpointed approaches has been proposed to investigate *disordered* systems via titania thin film. Next, the electronic and excitation properties of the titanium clusters and their graphene composites are investigated using constrained density-functional theory. The electronic structure and, in particular, the excitation energies of the bare clusters and the titania/graphene composites are found to vary significantly depending on the size of the respective constituents. This holds in particular for the energy and the spatial localisations of the highest occupied and lowest unoccupied molecular orbitals. Along with a substantial gap narrowing, a pronounced separation of photo-excited electrons and holes is predicted in some instances. Finally, a series of new organic donor-π-acceptor dyes have been studied using range-separated hybrid exchange-correlation functionals in density-functional theory and time-dependent density-functional theory, and this study confirms that they exhibit intramolecular charge transfer behaviour. Additionally, the superior performance of range-separated hybrid functionals in describing these molecules' excitation properties is compared against other exchange-correlation functionals and experiments. Altogether, it is shown that hybrid functionals, Hubbard correction, and constrained density-functional theory approaches can be used fruitfully to augment the standard exchange-correlation functional used in the density-functional framework.

Table of Notations

The following list describes the significance of various abbreviations and acronyms used throughout the thesis. The page on which each one is defined or first used is also given. Nonstandard acronyms that are used in some places to abbreviate the names of certain materials structures are not in this list.

List of Acronyms

DFT	Density Functional Theory	3
MB	Many-Body	3
XC	Exchange-Correlation	3
CDFT	Constrained Density-Functional Theory	3
DFT+U	Hubbard U corrected Density-Functional Theory	3
SIE	self-interaction error	3
TDDFT	Time-Dependent Density Functional Theory	4
HK	Hohenberg-Kohn	4
KS	Kohn-Sham	4
RS	range-separated	4
D-π-A	donor-π bridge-acceptor	4
SE	Schrödinger Equation	5
BO	Bohr-Oppenheimer	6
HF	Hartree-Fock	7

IE	Ionisation Energy	7
SCF	self-consistent field	7
LDA	Local Density Approximation	11
GGA	Generalised Gradient Approximation	11
LSDA	Local Spin Density Approximation	11
Meta-GGA	Meta-Generalised Gradient Approximation	12
PBE	Perdew-Burke-Ernzerhof–an exchange-correlation functional	12
$\mathbf{PBE_{sol}}$	Perdew-Burke-Ernzerhof functional derivative for solids	12
LYP	Lee–Yang–Parr	12
B88	Becke-1988	12
B97	Becke-1997	12
ΔSCF	delta self-consistent field	12
EA	Electron Affinity	12
HOMO	Highest Occupied Molecular Orbital	13
LUMO	Lowest Unoccupied Molecular Orbital	13
LR	long-range	13
GW	Single-Particle Green Function with Screened Coulomb Interaction (ω)	14
BSE	Bethe-Salpeter screened equation	14
BZ	Brillouin zone	17
LFE	Local Field Effect	18
IPA	Independent-Particle Approximation	18
RPA	Random-Phase Approximation	18
ALDA	Adiabatic Local Density Approximation	18

VASP	Vienna *ab initio* simulation package	18
QE	Quantum ESPRESSO	18
ORCA	ORCA quantum chemistry program	18
AO	Atomic Orbital	18
PW	Plane-Wave	18
PP	*Pseudopotential*	18
PAW	Projected Augmented Wave Method	19
def2-TZVP	Gaussian basis sets of triple zeta valence	19
MP	Monkhorst-Pack	20
NC-PP	*norm-conserving pseudopotential*	20
US-PP	*ultra-soft pseudopotential*	21
vdW	van der Waals	21
SIC	self-interaction error correction	24
DFPT	Density Functional Perturbation Theory	25
B3LYP	Becke 3-parameter Lee–Yang–Parr	26
EXX	"exact exchange"	26
PBE0	zero parameter hybrid functional based on PBE	26
VWN	Vosko-Wilk-Nusair	26
TPSSh	hybrid functional based on Tao–Perdew–Staroverov–Scuseria functional	26
SR	short-range	27
HSE	Heyd–Scuseria–Ernzerhof	27
CAM	Coulomb attenuating method	28
ωB97	hybrid functional based on Becke-1997 functional	28

R	Rutile	29
A	Anatase	29
B	Brookite	29
ICT	intramolecular charge transfer	29
DQ	diquat	29
UV	Ultraviolet	30
VB	valence band	30
CB	conduction band	30
D	Direct	31
ID	Indirect	31
PDOS	Partial Density of States	31
GR	Graphene	37
GQD	Graphene Quantum Dot	38
DOS	Density of States	41
TPA	triphenylamine	44
TPT	thienylphenylthienyl	44
TT	bithiophene	44
TBtdT	thienyl-benzothiadiazo-thienyl	44
BPNO	bipyridine-oxide	44
PF_6	hexafluorophosphate anion	59

List of Figures

List of Tables

Contents

"The Being of the universe, at first hidden and concealed, has no power which can offer resistance to the search for knowledge; it has to lay itself open before the seeker - to set before his eyes and give for his enjoyment, its riches and its depths."

— Georg Wilhelm Friedrich Hegel,
Lecture on the History of Philosophy,
Heidelberg, 28 October 1816.

1

General Introduction

1.1 The need for renewable energy, and clean water and air

As global population and economic growth accelerate, clean and sustainable energy generation and environmental problems have risen to prominence as humanity's top challenges and issues in the 21st century. Hence, the exponential development of the human population and the intensification of agricultural and industrial activities have resulted in an ever-increasing demand for the Earth's finite fresh water supply. Protecting natural water supplies and developing innovative technologies for water and wastewater treatment go on to be critical environmental challenges of the 21st century in this setting. On the other hand, growing awareness of the Earth's finite supply of raw fossil resources is spurring countless initiatives to develop benign and sustainable alternatives.[1] Apart from increasing the use of renewables as a primary chemical feedstock, one of the most significant difficulties facing science and engineering is meeting the world's expanding energy demand. As a result, it is vital to create efficient technologies for converting energy from renewable sources.[2]

As the main energy source supplied from extraterrestrial space, solar energy has the potential to exceed the overall world energy demand significantly.[3] Given the expected longevity of the Sun, solar energy must be regarded as the ultimate renewable resource that can be harvested on Earth.[4] Despite this, the energy source's intermittent and diurnal nature poses significant harvesting, storage, and consumption issues.[5] There are now a variety of technologies that can be utilised to overcome these challenges. For example, high-capacity batteries integrated into photovoltaic cells can play a role in converting solar energy into electricity and stabilising future power grids.[6] Another technique of solar energy harvesting and storage concerns photochemical reactions such as photocatalytic water-splitting producing hydrogen.[7] Hydrogen is particularly interesting among the different energy sources since it enables the efficient conversion of chemical energy to electrical energy via a fuel cell, with the sole result being water. Furthermore, a notable advantage of a hydrogen economy is the substantial reduction in greenhouse gas emissions.[8] Consequently, it has become necessary to study and develop innovative systems for societal growth. Also, the photocatalyst can be used for various purposes, including degradation of various organic pollutants in wastewater, antibacterial activity, and air purification. Given this information, photocatalyst systems are likely to be a powerful remedy.

1.2 Photocatalyst

Since the beginning of the 20th century, scientists have desired to design artificial systems that mimic natural photosynthesis to harvest and convert solar energy directly into usable or storable energy resources. Solar energy as an energy source for organic synthesis is not a unique concept, first introduced in 1912 by Ciamician.[9] However, the widespread use of the word photocatalysis and substantial advances in this subject began in the 1970s, following Fujishima and Honda's discovery of water photolysis on TiO_2 electrodes.[10] Following this, the photocatalytic oxidation capabilities were investigated for the oxidation or degradation of hazardous organics in polluted water, air, or soils.[11, 12] In 1977, the photocatalytic degradation of inorganic cyanide and sulphite was also displayed in water, utilising some semiconductor powders for wastewater treatment and environmental pollutant remediation.[13]

Following wastewater treatment, photocatalytic CO_2 reduction was described in 1979, providing a unique method for reducing CO_2 to hydrocarbons and CO.[14] Yamagata *et al*. reported the photocatalytic oxidation of alcohols on TiO_2 in 1988, demonstrating that oxygen engaged in a radical chain process during the oxidation of ethanol to acetaldehyde, paving the way for selective organic oxidation.[15] Additionally, the TiO_2's photoinduced hydrophilicity has enabled the application of photocatalysis as the self-cleaning and anti-fogging technology for developing building materials.[16] Furthermore, photocatalysis is increasingly garnering the interest of researchers in chemical biology, materials science, and drug development, who understand that these processes provide prospects for innovation in fields other than conventional organic synthesis.[17, 18] Along the way, photocatalysis has drawn much attention in recent years as a means of protecting the environment and generating clean energy and could be widely employed in many real-world applications.[19] So far, detailed information about noteworthy improvements in photocatalysis can be found in the following Refs. [20–22].

1.2.1 Basic Principle of Heterogenous Photocatalysis

This part discusses the principles of photocatalytic reactions, a surge of developments in photocatalyst materials, and the factors affecting photocatalytic activity. The semiconductor materials' characteristic electronic structures have been identified as the most promising candidate for absorbing solar energy.

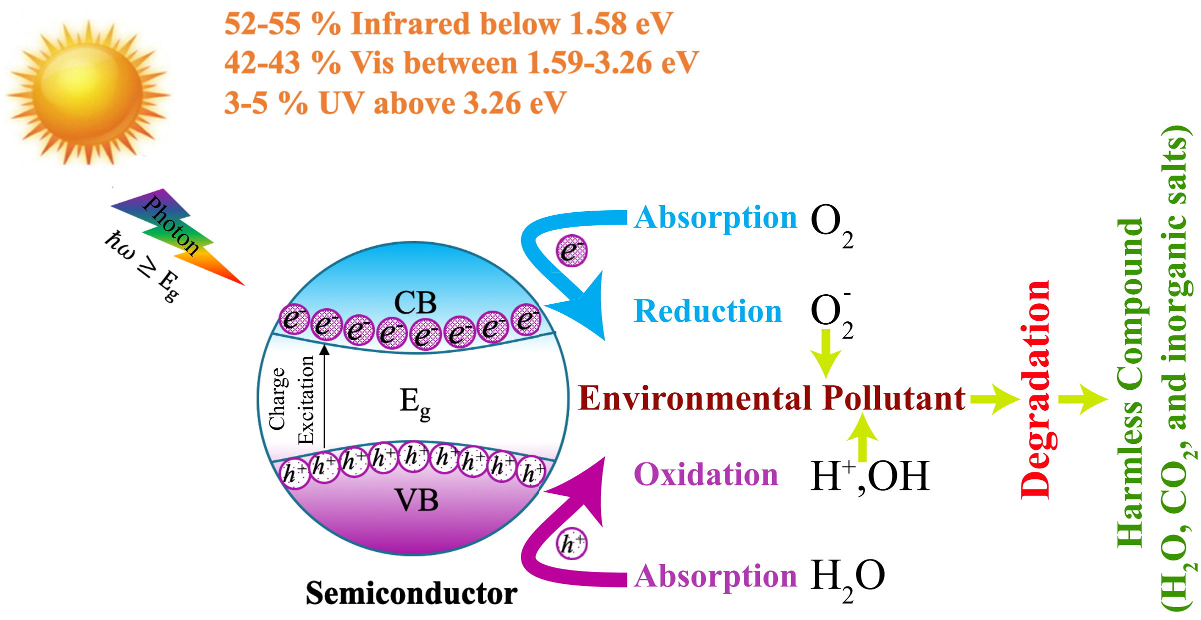

Figure 1.1: Schematic representation of Heterogeneous Photocatalytic Reactions in Semiconductor.

A fundamental mechanism of photo-excited reactions is shown in Figure 1.1. A photocatalyst semiconductor system absorbs incident photons with higher energy than its band gap and produces photo-excited electron-hole pairs; that is, the excited electrons jump to the conduction band, leaving photo-generated holes in the valence band. Afterwards, electrons and holes transfer to their corresponding surface-active sites, respectively. As a result, the semiconductor's conduction band can have more negative potential than the chemical species' reduction potential, and the semiconductor's valence band can have more positive than the chemical species' oxidation potential. These characteristics allow photo-reduction and photo-oxidation processes.[23]

A significant advantage of semiconductors is their chemical and thermal stability and their non-degradation during photocatalytic processes. Moreover, this heterogeneous photocatalysis can be recyclable by filtering or centrifugation. However, an appropriate band gap and band position values are necessary to trigger this reaction, and it is also highly desirable that these materials are inexpensive and non-toxic. Even if the band gap and band position of compounds need to be adjusted to the working conditions, especially for visible-light-driven heterogeneous photocatalytic activity, the fast recombination rate of electron-hole pairs which is known to inhibit catalytic behaviour, must also be mitigated or prevented. Several experimental and theoretical techniques are used to improve photocatalytic activity; for example, the separation of charge carriers can be improved by forming direct connections between existing photocatalyst compounds with carbon allotropes or another semiconductor, as the heterostructuring and surface hybridisation.[24] In addition, modification of the crystal structure[a][25] and particle's size[b][26] can also help in the development of advanced photocatalyst models.

1.3 Motivations and Objectives

Despite the developments of highly efficient materials technology being primarily experimental in the 20th century, recent advances in computer technology have significantly impacted the study of nanostructured materials, not only in the fundamental understanding of structure-property relationships[27–30] but also in its manifested growing technology applications.[29–35] The breakthrough discovery of Density Functional Theory (DFT)[c],[36–38] which addresses the Many-Body (MB) issue using non-interacting electron density and XC functionals, has become widely used for providing fundamental insight, aiding in interpreting experimental data and developing novel materials.[32–34] More recent examples of this progress include topological Dirac/Weyl materials,[39–41] the physics of diverse 2D materials[42–44] and their co-integration in valleytronics,[45] twistronic,[46] slidetronics,[47] and spintronic[48] heterostructure, the underlying physical processes in organic electronics,[49–51] and the development of visible-light-responsive heterojunction photovoltaics[52–54] and photocatalyst[55–60] systems.

Although it is accepted as an accurate and cost-effective method in physics, chemistry, materials science, and biology to study nanostructure materials,[32–35] the XC functional holds the key to the success or failure of DFT. Indeed, the exact form of XC concerning the density remains unknown, and approximations are necessary for it. For several predicted properties, the remarkable failures have been related to the self-interaction error (SIE) of commonly employed basic approximate XC functionals. Reducing the SIEs at a reasonable computational cost can accurately simulate the exact behaviour of large-scale and disordered systems. As such, the established and computationally efficient Constrained Density-Functional Theory (CDFT), Hubbard U corrected Density-Functional Theory (DFT+U), and hybrid functional methods are now frequently applied to these systems to recover the absent physical characteristics.

---

[a] Creating surface defects can trap charge carriers and act as recombination centres.

[b] Small particle size has a high specific surface area; the smaller the particles are, the shorter the distance the charge carriers need to travel to the surface.

[c] Actually, the brilliance of DFT is that its formalism is exact yet efficient, with a single determinant defining the electron density; all the complexity is concealed in a single term, the Exchange-Correlation (XC) functional.

1.4 Structure of this thesis

The remainder of this thesis encompasses the research study spanning the following four chapters and appendix:

Chapter 2 reviews all computational methods used throughout the thesis, the corresponding theoretical background and the key developments that have contributed to the formulation of the contemporary Kohn-Sham (KS)-DFT, including the Hohenberg-Kohn (HK) theorems, the KS equations and the construction of approximate standard XC functionals. Furthermore, the CDFT and Time-Dependent Density Functional Theory (TDDFT) are reviewed in this chapter. Additionally, numerical technical aspects are also discussed to point out how the problem can be solved in practice.

Chapter 3 presents the drawback of DFT by discussing the SIE. Additionally, the Hubbard-corrected DFT and the hybrid functional are presented based on how the SIE is effectively eliminated.

Chapter 4 presents different systems that were addressed using various methodologies. In the first case, it is shown how the application of Hubbard U correction and the hybrid functional approach significantly reduces the errors exhibited by the standard XC functional in describing three major phases of TiO_2. Following it, optimised parameters in both methodologies are used to investigate thin film titania. In the second case, the electronic structure and, in particular, the excitation energies of the bare titania clusters and the titania/graphene composites are analysed using DFT, the hybrid functional approach, and CDFT. It is shown that the electronic structure and, in particular, the excitation energies of the bare clusters and the titania/graphene composites vary largely depending on the size of the respective constituents. This holds in particular for the energy and the spatial localisation of the highest occupied and lowest unoccupied molecular orbitals. In addition to a substantial gap narrowing, a pronounced separation of photo-excited electrons and holes is predicted in some circumstances. In the third case, a series of new organic donor-π bridge-acceptor (D-π-A) dyes as a novel electron-acceptor-unit are investigated using the range-separated (RS) hybrid functional approach and TDDFT, and this study confirms they exhibit intramolecular charge transfer behaviour. Additionally, the superior performance of RS hybrid functional in describing excitation properties of these molecules is also compared against experimental result.

Chapter 5 summarises the work presented in this thesis and provides a perspective for further studies based on the thesis's understanding.

Finally, Appendix contains supplementary information necessary for the discussions in this thesis.

> *"It can scarcely be denied that the supreme goal of all theory is to make the irreducible basic elements as simple and as few as possible without having to surrender the adequate representation of a single datum of experience."*
>
> — Albert Einstein,
> *Lecture on the Method of Theoretical Physics,*
> *Oxford, 10 June 1933.*

2

Theoretical Foundations

The following chapter highlights the basic building blocks of MB theories relevant to the research presented in this thesis. These aspects are directly related to the description of electronic states in materials, which can be investigated using DFT and TDDFT formalisms. Later, some physical and numerical techniques will also be discussed.

2.1 The Schrödinger Equation

Since the geneses of quantum mechanics in the early 20th century, the possibility of understanding the universe or nature at its most microscopic and potentially most fundamental level has been a central subject of the study of physics. Understanding and describing a material's electrical characteristics need dealing with a system composed of many interacting electrons; this is referred to as the MB problem. This issue is completely governed by solving the MB Schrödinger Equation (SE), which reflects all possible interactions among the electronic structure of assemblies of atoms in a compound. A general MB time-independent SE has the following form:

$$\hat{\mathrm{H}}\Psi_{\mathrm{i}}(\{\mathbf{r}\},\{\mathbf{R}\}) = \mathrm{E}_{\mathrm{i}}\Psi_{\mathrm{i}}(\{\mathbf{r}\},\{\mathbf{R}\}), \tag{2.1}$$

where $\{\mathbf{r}\}$ and $\{\mathbf{R}\}$ denote, respectively, the sets of electronic and nuclei coordinates, and E_{i} and Ψ_{i} represent, respectively, the energy and wavefunction of the i^{th} state. The Hamiltonian $\hat{\mathrm{H}}$ plays a critical role in this equation since it includes all information regarding energy in a quantum system. The Hamiltonian for the system of electrons and nuclei will be as follows:

$$\hat{\mathrm{H}} = \underbrace{-\frac{\hbar^2}{2\mathrm{m_e}}\sum_i \nabla_i^2}_{\mathrm{T_{el}}} \underbrace{-\sum_{\mathrm{I}} \frac{\hbar^2}{2\mathrm{M_I}}\nabla_{\mathrm{I}}^2}_{\mathrm{T_{nuc}}} + \underbrace{\frac{1}{2}\sum_{i\neq j}\frac{e^2}{|\mathbf{r}_i-\mathbf{r}_j|}}_{\mathrm{V_{el-el}}} \underbrace{-\sum_{i,\mathrm{I}}\frac{Z_{\mathrm{I}} e^2}{|\mathbf{r}_i-\mathbf{R}_{\mathrm{I}}|}\nabla_{\mathrm{I}}^2}_{\mathrm{V_{el-nuc}}} + \underbrace{\frac{1}{2}\sum_{\mathrm{I}\neq \mathrm{J}}\frac{Z_{\mathrm{I}}Z_{\mathrm{J}}e^2}{|\mathbf{R}_{\mathrm{I}}-\mathbf{R}_{\mathrm{J}}|}}_{\mathrm{V_{nuc-nuc}}}, \tag{2.2}$$

where ħ, $\mathrm{m_e}$ and e represent the Planck constant, electron's mass, and charge, respectively.[a] M and Z denote the nucleus's mass and charge, respectively. The indexes i, j represent electrons, whereas I, J represent the nucleus. The electronic and nuclei coordinates are labelled by r and R. The first and second components in Hamiltonian (2.2) are the kinetic energies of electrons ($\mathrm{T_{el}}$) and nuclei ($\mathrm{T_{nuc}}$), respectively. The subsequent three terms are Coulomb interactions. The electron-nuclei interaction ($\mathrm{V_{el-nuc}}$) is the third term, the electron-electron interaction ($\mathrm{V_{el-el}}$) is the fourth term, and the nuclei-nuclei interaction ($\mathrm{V_{nuc-nuc}}$) is the last term.

---

[a] Hartree atomic units, with ħ = $\mathrm{m_e}$ = e = 1, are considered throughout this thesis, unless otherwise explicitly stated!

The Hamiltonian's complexity rises exponentially with the number of interacting particles, and the exact solution of the SE using the Hamiltonian (2.2) is so complicated that it cannot be used to describe realistic systems with a large number of interacting particles.[b] As a result, approximations must be employed to address the investigated systems more efficiently.

2.2 The Born-Oppenheimer Approximation

The initial thing becoming apparent is that the mass of nuclei is many orders of magnitude larger than that of electrons.[c] The nuclei move more slowly, and their kinetic energy is much smaller than that of electrons. In this context, the SE can be decoupled into a pair of equations, one representing the motion of electrons and the other describing the motion of nuclei. This approximation is referred to be Bohr-Oppenheimer (BO) or adiabatic approximation.[61] Hence, the initial wavefunction $\Psi(\mathbf{r},\mathbf{R})$ can be represented as the product of two wavefunctions that are solutions to the electrons' $\Psi_{\mathbf{R}}(\mathbf{r})$ and nuclei's $\Phi(\mathbf{R})$ wavefunctions as follows:

$$\psi(\mathbf{r},\mathbf{R}) = \Psi_{\mathrm{R}}(\mathbf{r})\Phi(\mathbf{R}). \tag{2.3}$$

For electrons, the MB SE will have the following form:

$$[\mathrm{T_{el}} + \mathrm{V_{el-el}} + \mathrm{V_{el-nuc}}]\Psi_{\mathrm{R}}(\mathbf{r}) = \mathrm{E_R}\Psi_{\mathrm{R}}(\mathbf{r}). \tag{2.4}$$

The index R is a fixed parameter indicating the position of the nuclei,[d] while the index r is a variable value indicating the position of the electrons. In Eqs. (2.3) and (2.4), r denotes ($\mathrm{r_1}$, $\mathrm{r_2}$, ...$\mathrm{r_n}$) and R denotes ($\mathrm{R_1}$, $\mathrm{R_2}$, ...$\mathrm{R_n}$). In further theories, the BO approximation is always considered, and the electrons move in a static external potential $\mathrm{V_{ext}(r)}$ formed by the nuclei. Hence, the Hamiltonian $\hat{\mathrm{H}}$ of the electronic system can further be considered as:

$$\hat{\mathrm{H}}_{\mathrm{el}} = -\sum_{\mathrm{i}} \nabla_{\mathrm{i}}^2 + \frac{1}{2}\sum_{\mathrm{i}\neq\mathrm{j}} \frac{1}{|\mathbf{r}_{\mathrm{i}} - \mathbf{r}_{\mathrm{j}}|} + \sum_{\mathrm{i}} \mathrm{V_{ext}}(\mathrm{r_i}). \tag{2.5}$$

2.3 Hartree and Hartree-Fock approximations from the Self-Consistent Field Theory

The BO approximation leaves us with the SE for electrons, which is still challenging to solve.[e] In order to deal with this problem, it is again necessary to resort to some approaches. In 1928, the first approximation method for solving the electronic problem was proposed by Hartree.[62] It is hypothesised that the many-electron wavefunction can be expressed as the product of single electron wavefunctions as follows:

$$\psi(\mathbf{r}_1,\mathbf{r}_2,\ldots,\mathbf{r}_{\mathrm{N_{el}}}) = \varphi_1(\mathbf{r}_1)\varphi_1(\mathbf{r}_2)\cdots\varphi_1(\mathbf{r}_{\mathrm{N_{el}}}), \tag{2.6}$$

and each of them satisfies the SE for a single particle in an effective potential. The Hartree method determines the effective potential using one-electron wave functions, and recurrent calculations are required

---

[b] Even for a small piece of matter, ~1 gram, the number of particles is about 10^{23}, making the exact solution of the SE impossible. The exact solution of the SE is only possible for basic systems such as atomic H and He, and the H^{2+} molecular ion!

[c] The mass of a proton is approximately 1836 times that of an electron.

[d] The index R has been omitted for the sake of simplicity in next sections!

[e] The central challenge in solving the SE using the BO approximation is that the wavefunction describing n electrons ($\mathrm{r_1}$, $\mathrm{r_2}$, ...$\mathrm{r_n}$) is an n-variable function. If one attempts to solve the issue numerically on a grid and uses, for example, a 10-point grid, the only x-coordinate demands a table 10×10; this is a 10×10×10 cube of information for 3 electrons. It is self-evident that in order to describe a single carbon atom in 3 dimensions, which is a critical element of all living organisms, a 9-dimensional table with 9 components is required. Additionally, the solution's quality will be quite compromised.

to find a self-consistent solution that minimises the total energy. However, this approximation includes the flaw of neglecting the anti-symmetry principle inherent in fermions. According to this theory, it is unknown which electrons are characterised by a particular orbital, allowing the orbitals to exchange. Further, the wavefunction's sign must be changed after each exchange. The anti-symmetric condition is not satisfied by the Hartree approximation.

Afterwards, this methodology was developed to incorporate the Pauli exclusion principle by expressing the total wave function in terms of Slater determinants[63]:

$$\psi_{\mathrm{el}}(\xi_1,\xi_2,\ldots,\xi_{\mathrm{N_{el}}}) = \frac{1}{\sqrt{\mathrm{N_{el}}!}} \begin{vmatrix} \varphi_1(\xi_1) & \varphi_2(\xi_1) & \cdots & \varphi_{N_{el}}(\xi_1) \\ \varphi_1(\xi_2) & \varphi_2(\xi_2) & \cdots & \varphi_{N_{el}}(\xi_2) \\ \vdots & \vdots & \ddots & \vdots \\ \varphi_1(\xi_{N_{el}}) & \varphi_2(\xi_{N_{el}}) & \cdots & \varphi_{N_{el}}(\xi_{N_{el}}) \end{vmatrix} \tag{2.7}$$

with $\xi_i = (\mathbf{r}_i, \sigma_i)$, $\mathbf{r}_i$ and σ_i represent the position and the spin of i^{th} electron, respectively. The improved form is referred to as the Hartree-Fock (HF) method, and it exactly incorporates the exchange terms while completely neglecting the MB correlation terms.[64] In general, this method is described as the self-consistent field (SCF) approximations, in which an electron is considered to move in the presence of an external interaction field created by other electrons and ions.[64]

Apart from calculating total energies, the HF method also approximates the Ionisation Energy (IE) of electron orbitals via Koopmans' theorem.[65] IE of an N-electron system is defined as the energy required to remove an electron:

$$\mathrm{IE^{HF}} = \mathrm{E^{HF}(N)} - \mathrm{E^{HF}(N-1)}, \tag{2.8}$$

where $\mathrm{E(N)}$ denotes the energy of a system of N electrons and $\mathrm{E(N-1)}$ denotes the energy of an $\mathrm{N-1}$ electron system. Based on this theorem, the IE is estimated by making the frozen orbital approximation, in which the electron is considered to be removed instantaneously, and the single particle electron orbitals of the $\mathrm{N-1}$ electron system are the same to those of the N electron system. Considering that the orbitals are frozen, the total energy of the $\mathrm{N-1}$ electron system from which an electron is removed is defined as follows:

$$\mathrm{E^{HF}(N-1)} = \mathrm{E^{HF}(N)} - \varepsilon_{\mathrm{n}}^{\mathrm{HF}}, \tag{2.9}$$

where $\varepsilon_{\mathrm{n}}^{\mathrm{HF}}$ is the eigenvalue associated with the $\mathrm{n^{th}}$ orbital.

Albeit HF approximation is one of the fundamental approximations for solving the MB SE, neglecting the effects of MB correlation terms is its first failure. In order to consider the Coulomb correlation, one must go beyond the single Slater representation. Methods developed to address this are well-known post-HF approaches, including the configuration interaction,[66] the Møller-Plesset second-order perturbation correction to the HF energy,[67] the coupled-cluster expansion,[68, 69] the complete active space SCF,[70] the complete active space perturbation theory[71] and the quantum Monte Carlo method[72] are often applicable only to molecules with a small number of active electrons, these approximations are impractical for MB structures.[73, 74]

Therefore, rather than obtaining information about each active electron in the system, it is more desirable to obtain information about expectation values or macroscopic quantities that do not require knowledge of the exact solution of Eq. (2.4). From this point of view, one can simplify the issue and its Hamiltonian by limiting the number of system variables to those of interest. This is analogous to the thermodynamic scenario, in which all systems are described in terms of macroscopic average quantities, irrespective of the exact microscopic configuration. Among the numerous approaches proposed in the literature, DFT and TDDFT are the most prominent examples of this MB problem simplification for treating equilibrium ground-state and dynamical properties, respectively.

2.4 Density-Functional Theory

DFT enables overcoming the difficulties mentioned above to analyse the geometry and ground-state electronic properties of various materials in a formally exact and computationally efficient manner.[36–38] This enables the exact determination of properties for a wide variety of systems, ranging from molecules and nanostructure to proteins and biological matter, as well as solids, surfaces, and interfaces.[f]

2.4.1 The Hohenberg-Kohn Theorems

Hohenberg and Kohn[g] showed in 1964 that the ground state energy of an electronic system is a unique function of the electron density. Additionally, it is demonstrated that, given an external potential, the ground-state energy can be derived by minimising the energy functional relating to the electron density. The energy functional is minimised when the density equals the correct ground-state electron density.[36] Their findings can be stated in two following theorems:

Theorem I (Existence Theorem): *Except for constants, the potential* $\mathrm{V_{ext}(r)}$ *of each system of interacting electrons is uniquely defined by the ground state particle density* $\mathrm{n_0(r)}$.[36]

Considering that $\mathrm{n_0(r)}$ determines $\mathrm{V_{ext}(r)}$ in the system, and $\mathrm{n_0(r)}$ will completely determine the ground state energy and all other electronic properties of the system. The only remaining problem is how to determine this density, and the following theorem is instructive.

Theorem II (Variational Principle): *It is possible to establish a universal functional for energy* $\mathrm{E[n]}$ *in terms of density* $\mathrm{n(r)}$*, which is valid for any external potential* $\mathrm{V_{ext}(r)}$*. For every* $\mathrm{V_{ext}(r)}$*, the exact ground state energy of the system is equal to its global minimum value, and the density* $\mathrm{n(r)}$ *that minimises the functional is equal to its exact ground state density* $\mathrm{n_0(r)}$.[36]

The total energy $\mathrm{E[n]}$ of the systems is a functional of electron density and can be expressed in the following form:

$$\mathrm{E[n] = T[n] + V[n] + \int V_{ext}(r)n(r)d^3r + E_{nuc-nuc} \equiv F[n] + \int V_{ext}(r)n(r)d^3r + E_{nuc-nuc}}, \tag{2.10}$$

where $\mathrm{T[n]}$, $\mathrm{V[n]}$, and $\mathrm{E_{nuc-nuc}}$ denote, respectively, the electronic kinetic energy, the electron-electron interaction energy and the nuclei's interaction energy, but $\mathrm{F[n]}$ denotes the internal energy functional. It is worth noting that the $\mathrm{F[n]}$ is a universal functional of the density for any system with a large number of electrons. Hence, if $\mathrm{F[n]}$ is known, the exact electron density of the ground state is simply found by minimising the energy functional. However, the HK theorems do not provide a practical solution of the SE for a many-electron system because the quantity $\mathrm{F[n]}$ is completely unknown. Therefore, the KS equations of the DFT reported in the next part have been practically used to realise the solution of the SE, and it has also formed the basis for developing all modern DFT codes.

---

[f] The advantage of DFT modelling method is based on the concept of describe the whole system using the electronic density distribution, a considerably simpler variable with only three degrees of freedom that corresponds to the complete MB wave function. This fundamental parameter is independent of the system's size, which enables the treatment of structures including hundreds of atoms without increasing the amount of data contained in simulations, as is the case with other methods based on the MB wave function.

[g] 1998 Nobel Prize in Chemistry for W. Kohn and J. A. Pople![38]

2.4.2 The Kohn-Sham Ansatz

The Thomas-Fermi-Dirac functional[h] was, in a sense, a precursor to DFT; Kohn and Sham developed the theory in 1965.[37] Their fundamental concept is to replace the complex MB problem of interacting electrons with an equivalent auxiliary independent-electron problem that is considerably easier to solve. In order to realise this approach, the HK functional F[n] can be separated into three components as follows:

$$F[n] = T_0[n] + E_H[n] + E_{xc}[n]. \tag{2.11}$$

Here, $T_0[n]$ is the kinetic energy of a system of non-interacting electrons in its ground state with the electronic charge density $n(r)$[i], and Hartree energy $E_H[n]$ is the electrostatic self-interaction energy for the charge density $n(r)$:

$$E_H[n] = \frac{1}{2}\int \frac{n(r)n(r')}{|r-r'|} d^3r d^3r', \tag{2.12}$$

and the remaining term $E_{xc}[n]$, referred to as the XC functional, defines all unfamiliarity about the exact form of the HK functional:

$$E_{xc}[n] = F[n] - T_0[n] - E_H[n]. \tag{2.13}$$

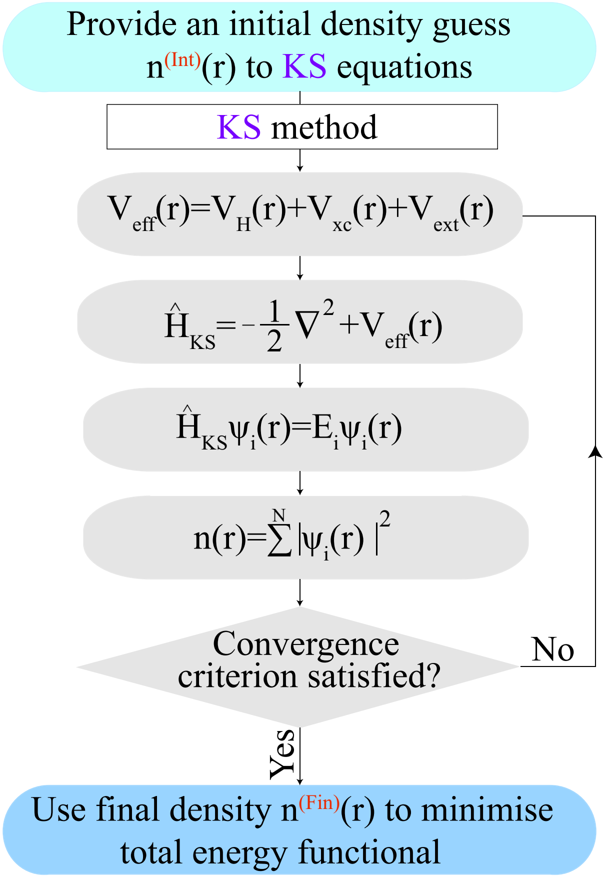

Figure 2.1: Schematic representation of the SCF iteration flowchart.

At the ground state charge density $n(r)$, the XC functional $E_{xc}[n(r)]$ is simply the difference between the sum of the electronic kinetic energy $T[n(r)]$ and the electron-electron Coulomb interaction energy $V[n(r)]$ for the fully interacting system and the sum of the electronic kinetic energy $T_0[n(r)]$ and the Hartree energy $E_H[n(r)]$ for the non-interacting system. It is hoped that the unknown term $E_{xc}[n(r)]$ is small enough to be approximated accurately. Based on the Eq. (2.11), the energy functional $E[n(r)]$ can be written in the following form:

$$E[n(r)] = T_0[n] + E_H[n(r)] + E_{xc}[n(r)] + \int V_{ext}(r)n(r)d^3r. \tag{2.14}$$

In order to determine the ground-state energy of the fully interacting system, the HK's Theorem II is used; that is, the energy functional $E[n(r)]$ in the Eq. (2.14) is minimised concerning the charge density $n(r)$ under the constraint of a constant electron number $N = \int n(r)d^3r$. As a consequence, the following equation is formed:

$$\frac{\delta T_0[n(r)]}{\delta n(r)} + \underbrace{\int \frac{n(r')}{|r-r'|}d^3r}_{V_H(r)} + \underbrace{\frac{\delta E_{xc}[n(r)]}{\delta n(r)}}_{V_{xc}(r)} + V_{ext}(r) = \mu, \tag{2.15}$$

---

[h] In this methodology, the electron-electron interaction V_{el-el} with a classical Hartree term and the kinetic energy T_{el} with a local density approximation based on that of a homogeneous electron gas. However, the technique has been shown to fail (for example, in replicating the right atomic shell shape and chemical bonding) because T[n]+V[n], which accounts for a significant part of the total energy, is difficult to approximate.[75–77]

[i] The electronic kinetic energy functional $T_0[n]$ is a well-defined functional of $n(r)$, based on the HK's Theorem I. For a non-interacting electrons' system, the HK functional $F_0[n]$ is simply presented by $T_0[n]$.

where $V_H(r)$ and $V_{xc}(r)$ are the Hartree potential and the unknown XC potential, respectively and μ is a Lagrange multiplier[78] associated with the constraint of a constant electron number N. If the HK's Theorem II is applied to a system of N non-interacting electrons moving in an effective potential $V_{eff}(r)$, defined as follows:

$$V_{eff}(r) = V_H(r) + V_{xc}(r) + V_{ext}(r), \tag{2.16}$$

the same equation as in the Eq. (2.14) is obtained. Based on the above findings, solving the fully interacting MB problem is identical to solving the problem of N non-interacting electrons moving in the effective potential $V_{eff}(r)$ defined by the Eq. (2.16), since both problems result in the same ground-state charge density $n(r)$. For N non-interacting electrons, the problem of N interacting electrons has now been simplified to the corresponding one-body SE as follows:

$$[-\frac{1}{2}\frac{d^2}{dr^2} + V_H(r) + V_{xc}(r) + V_{ext}(r)]\psi_i(r) = \varepsilon_i \psi_i(r), \tag{2.17}$$

where ε_i denotes the one-body KS energy, and $\psi_i(r)$ denotes the KS orbital corresponding to it. The ground-state charge density $n(r)$ is calculated from the lowest-lying KS orbitals $N_d = \frac{1}{2}$, defined as follows:

$$n(r) = 2\sum_{i=1}^{N_d} |\psi_i(r)|^2, \tag{2.18}$$

where N_d is the number of doubly occupied orbitals. Finally, the original fully interacting system's ground-state energy can be calculated as follows:

$$E[n(r)] = \sum_i \varepsilon_i - E_H[n(r)] + E_{xc}[n(r)] - \int V_{xc}(r)n(r)d^3r. \tag{2.19}$$

The renowned set of KS equations is celebrated by Eqs. (2.17-2.19), often solved self-consistently through iterative techniques, as shown in Figure 2.1. To get the ground state total energy of the whole system, one must include the Coulomb nuclei interaction term to the electronic ground state energies $E_0(n_0(r))$, defined by:

$$E_{Tot} = E[n(r)] + \frac{1}{2}\sum_{I \neq J} \frac{Z_I Z_J}{|\mathbf{R}_I - \mathbf{R}_J|}. \tag{2.20}$$

Nevertheless, to find the actual ground state of a system, one must also figure out the equilibrium atomic geometries, which are the ones where the forces on all the atoms are at their lowest. The force on the Ith atom is found by adding the gradient concerning $\mathbf{R}_I$ to the total energy, defined by:

$$\mathcal{F}_I = -\nabla_{R_I} E_{Tot} = \underbrace{-\nabla_{R_I} E_{nuc-nuc}}_{\text{nuclei force}} \underbrace{- \int n(r)\nabla_{R_I} V_{ext}(R_I;r)d^3r - \int \frac{\delta E[n(r)]}{\delta n(r)} \nabla_{R_I} n(r) d^3r}_{\text{electronic force}}, \tag{2.21}$$

where the nuclei force is determined primarily by the interaction between nuclei. However, the electronic force is governed by the external potential contribution, depending parametrically on the atomic positions and the variational force, occurring because of the implicit dependence of the electron density $n(r)$ on the atomic sites. In principle, the variational force disappears in the electronic ground state, so only the combination of nuclei force and atomic position-dependent external potential force, the so-called Hellmann-Feynman forces,[79] has a physical basis. Consequently, the Hellmann-Feynman forces must be disappeared to find the system's structural equilibrium.

So far, KS-DFT has continued to flourish under the auspicious stewardship of countless contributors; detailed information about improvements of original KS studies (for example, spin-polarised, finite temperature in thermal equilibrium, and current-density in strong electromagnetic field) can be found in Refs. [80–82].

2.5 Treatment of Electron Correlations in Density Functional Theory

Except for the BO approximation, all the previous equations (in Sections 2.2 and 2.4) have been formally exact. However, V_{xc} must be approximated due to the absence of its explicit functional. In this concept, a large number of approximations, varying in their forms and complexity, have been presented to calculate the XC functional. There is now an almost endless number of approximations with differing degrees of complexity. Perdew has developed a useful way for categorising the numerous and various E_{xc} functionals that exist, termed "Jacob's ladder", see Figure 2.2. The Hartree approach is on the ground and the exact XC functional "on heaven". Among them, the simplest approximations on the few rungs of this ladder (Local Density Approximation (LDA) and Generalised Gradient Approximation (GGA)), commonly used in DFT, are presented comprehensively in the following part.

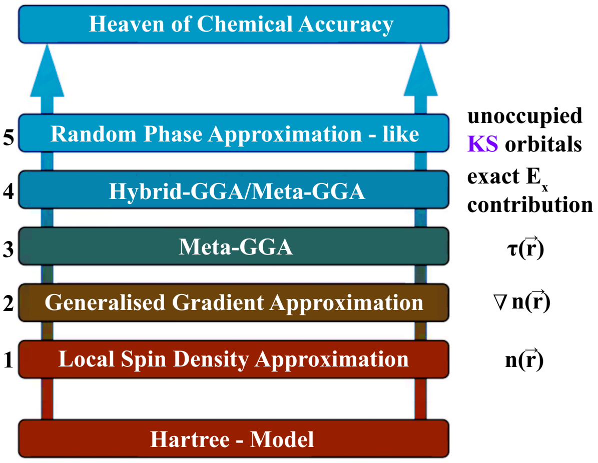

Figure 2.2: Schematic representation of Jacob's ladder like ranking of XC functionals, adapted from Ref. [83].

2.5.1 Local Density Approximation

In the LDA, the system is considered as a homogeneous electron gas interacting locally, similar to the Thomas-Fermi approach.[37] Here, the XC energy $E_{xc}[n(r)]$ per electron was the same as that of a homogeneous electron gas with the same charge density $n(r)$:

$$E_{xc}^{LDA}[n(r)] = \int n(r)\varepsilon_{xc}[n(r)]d^3r. \tag{2.22}$$

For a homogeneous interacting electron gas, the exchange part of ε_{xc} can be expressed analytically as a function of $n(r)$ using the Slater determinant of the KS wavefunctions,[77, 84] but the correlation part can be effectively determined using quantum Monte-Carlo method.[85] The functional derivative of Eq. (2.22) yields the LDA XC potential $V_{xc}^{LDA}(r)$ as:

$$V_{xc}^{LDA}(r) = \varepsilon_{xc}[n(r)] + n(r)\frac{d\varepsilon_{xc}(n)}{dn}\bigg|_{n=n(r)}. \tag{2.23}$$

This formalism can be easily extended to add electronic spin as:

$$E_{xc}^{LSDA}[n_\uparrow(r), n_\downarrow(r)] = \int n(r)\varepsilon_{xc}[n_\uparrow(r), n_\downarrow(r)]d^3r, \tag{2.24}$$

and it is called Local Spin Density Approximation (LSDA).[86, 87] This approximation becomes exact in principle when electronic charge densities have minor spatial variations. Furthermore, it performs excellent performance even for high inhomogeneous systems, which can be partially explained by utilising the XC hole's properties.[88] The structural and vibrational properties of weakly correlated systems have been demonstrated to be well reproduced by LDA. However, the cohesive energies of solids and the binding energies of molecules are frequently overestimated, resulting in an underestimate of bond lengths.[89]

2.5.2 Generalised Gradient Approximations

The first attempt that goes beyond the LDA is to include some form of non-locality via the gradient of the density.[90–92] Hence, GGA is preferred over LDA because it also considers the inhomogeneity of the charge density; that is, the XC energy $E_{xc}[n(r)]$ per particle depends on both the local charge density $n(r)$ and its gradient $\nabla n(r)$:

$$E_{xc}^{GGA}[n_{\uparrow}(r), n_{\downarrow}(r)] = \int n(r)\varepsilon_{xc}^{GGA}[n_{\uparrow}(r), n_{\downarrow}(r), \nabla n_{\uparrow}(r), \nabla n_{\downarrow}(r)]d^3r. \tag{2.25}$$

The Perdew-Burke-Ernzerhof–an exchange-correlation functional (PBE) is one well-known example of GGA functionals[j] in terms of its general applicability and highly reliable results for various systems.[98] Afterwards, the Perdew-Burke-Ernzerhof functional derivative for solids (PBE_{sol}) was proposed to improve the equilibrium properties of densely packed solids and their surfaces.[99]

Although GGA results are not always superior to LDA results for metals and surfaces, they sometimes correct errors observed in LDA, especially when electronic charge densities change rapidly. Despite the general success of LDA and GGA for exchange and correlation, there are also limitations and failures of the DFT in the following areas:

- the description of systems with localised electrons;[100]
- the description of the binding energy, being particularly evident in the evaluation of the semiconductor band gaps;[101]

and these failures are directly related to the SIE, discussed comprehensively in the following Chapter 3.

In order to avoid these failures, three different options are considered in this thesis. In the first option, CDFT is used, which enables one to treat the physical quantities as a difference between two total energies arising from two fully SCF calculations for different systems. It will be discussed in the following Section 2.6. The second option is to use the Hubbard U correction, proposed by James Hubbard, which provides a straightforward solution to the problem of strongly correlated electrons in materials. Furthermore, its simplicity does not preclude it from accurately predicting the complicated effects of some correlated systems. The third option is to use more precise XC functionals, namely hybrid functionals that integrate some proportion of HF exact exchange and have been proven to result in improved electronic characteristics of semiconducting materials. Detailed information about the Hubbard U correction and hybrid functional methodologies and their applications to some photocatalyst systems will be discussed in the next chapters.

2.6 Constrained Density-Functional Theory

Motivated by an extension of the Koopman theorem in HF theory, the delta self-consistent field (ΔSCF), also termed CDFT, enables one to treat the physical quantities as a difference between two total energies arising from two fully SCF calculations for different systems. Based on this method, the investigation of excited state energies using time-independent DFT can be traced back to the proof that stationary solutions of the ground state functional reflect excited states.[102–105] It is appropriate for systems with sufficiently localised charged excitations (IE and Electron Affinity (EA)) and neutral excitations (photon absorption). As ΔSCF inherits the advantageous computational scaling of the ground-state DFT, it has a substantially lower computational cost than other methodologies. Within the ΔSCF method, the IE, EA,

---

[j] Other GGA functionals such as the Lee–Yang–Parr (LYP)[93], Becke-1988 (B88)[94] and Becke-1997 (B97)[95] appear in the literature and have been used depending on research interest and motivation. Another extension of GGAs is to include terms based on the second $\nabla^2 n(r)$ or higher derivatives of the electron density in addition to terms based on the kinetic energy density $\tau(r)$.[96, 97] Such functionals, called Meta-Generalised Gradient Approximation (Meta-GGA), have shown better performance compared to conventional GGAs, so it is placed in the third rung of "Jacob's ladder", see Figure 2.2.

and the quasiparticle energy gap E^{QP} between the Highest Occupied Molecular Orbital (HOMO) and Lowest Unoccupied Molecular Orbital (LUMO) are calculated as follows:

$$IE_v = E(N-1) - E(N) \approx -E_{HOMO}, \tag{2.26}$$

$$IE_{ad} = E^*(N-1) - E(N), \tag{2.27}$$

$$EA_v = E(N) - E(N+1) \approx -E_{LUMO}, \tag{2.28}$$

$$EA_v = E(N) - E^*(N+1), \tag{2.29}$$

$$E^{QP} = IE_v - EA_v, \tag{2.30}$$

where $E(N)$, $E(N+1)$, and $E(N-1)$ are the energies of the systems with N, $N+1$, and $N-1$ electrons in the geometry of the neutral system, respectively. Before calculating $E(N)$, $E(N+1)$, and $E(N-1)$ systems' energies, the different vacuum levels of N, $N+1$, and $N-1$ electron system must be appropriately aligned because moving an electron to and from the vacuum level appears without transferring kinetic energy. Furthermore, explicit calculations suffer from the limitations of the periodic boundary conditions. Therefore, monopole and dipole corrections[106, 107] must be applied to the anion and cation systems to compensate for the errors in the total energy and forces induced by spurious long-range (LR) electrostatic interactions between neighbouring supercells.

Optical gap or electron-hole pair excitation, which includes the attractive Coulomb interaction of the excited electron and hole screened by the remaining electrons, is defined as follows:

$$E^{\Delta SCF}_{Op} = E(N,e+h) - E(N), \tag{2.31}$$

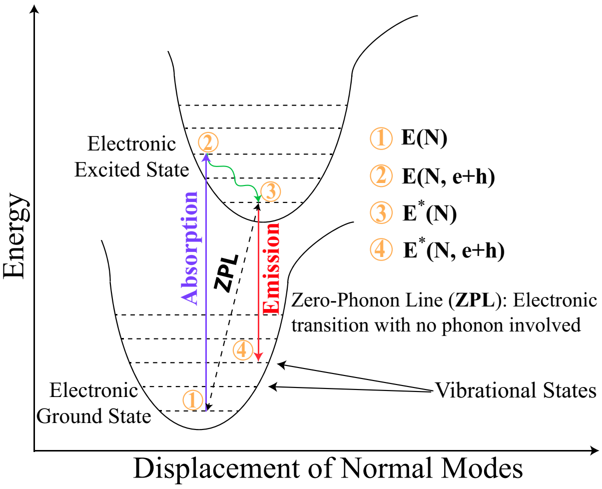

Figure 2.3: Schematic representation of the pair excitation energy calculation corresponding to the absorption and emission process.

where the $E(N,e+h)$ is the minimisation of the self-consistent total energy concerning the atomic coordinates in the presence of an electron-hole pair. This calculation is done by applying the occupation constraint that the HOMO of the ground-state system contains a hole, and the excited electron resides in the LUMO of the ground-state system. The lowest emission energy, measured in luminescence experiments, is defined as:

$$E^{\Delta SCF}_{Op^*} = E^*(N,e+h) - E^*(N), \tag{2.32}$$

where $E^*(N,e+h)$ is the total energy obtained after structurally and electronically optimising the system in the presence of the electron-hole pair. $E^*(N)$ is the self-consistent total energy of the system in its ground state electronic configuration evaluated at the optimised geometry of the pair-excited structure. The schematic mechanism is illustrated in Figure 2.3 for the pair excitation energy calculation corresponding to the absorption and emission process. The Stokes shift between the absorption and emission edges of the system can be calculated as:

$$\Delta_{ST} = E^{\Delta SCF}_{Op} - E^{\Delta SCF}_{Op^*}. \tag{2.33}$$

Finally, the exciton binding energy E^{ex}_b of the system is defined as the energy difference between between the quasiparticle HOMO-LUMO energy gap E^{QP} and optical gaps E^{Op}. Note that both systems are achieved in practice by imposing an occupation constraint on the electronic states throughout the entire self-consistency cycle.

2.7 Optical Response within Time-Dependent Density-Functional Theory

The description of the MB system in the excited state cannot be obtained in the framework of the conventional DFT. In order to access the excited state properties, the time-dependent MB problem can be solved using the Bethe-Salpeter[k] and TDDFT approaches. The TDDFT method is an extension of the ground state DFT presented by Runge and Gross, which accounts for external time-dependent perturbations in terms of time-dependent density.[108]

2.7.1 Runge-Gross Theorems

Following the conventional DFT strategy, in which the full MB problem is transformed into a non-interacting particle system, the time-dependent external perturbation is now applied to the static potential. As a result, the time-dependent density $\mathrm{n}(\mathrm{r},\mathrm{t})$ can be presented as a fundamental variable by a bijective function between density $\mathrm{n}(\mathrm{r},\mathrm{t})$ and external potential $\mathrm{V}_{\mathrm{ext}}(\mathrm{r},\mathrm{t})$.

Theorem III: *For any system of interacting particles in an external time-dependent potential* $\mathrm{V}_{\mathrm{ext}}(\mathrm{r},\mathrm{t})$ *that can be expanded in the Taylor series around* $\mathrm{t}=\mathrm{t}_0$ *and given an initial state* $\psi(\mathrm{r},\mathrm{t}_0)=\psi_0(\mathrm{r})$*, there is a bijection between* $\mathrm{V}_{\mathrm{ext}}(\mathrm{r},\mathrm{t})$ *and the time-dependent density* $\mathrm{n}(\mathrm{r},\mathrm{t})$*, excluding a trivial function of time.*[108]

By analogy with the HK Theorem I of conventional DFT, Theorem III states that it is possible to deduce the external potential $\mathrm{V}_{\mathrm{ext}}(\mathrm{r},\mathrm{t})$ from the knowledge of the density $\mathrm{n}(\mathrm{r},\mathrm{t})$ alone; hence, the MB wavefunction $\psi(\mathrm{r},\mathrm{t})$ determines each observable of the system in turn. Consequently, all observables can ultimately be regarded as functionals of the density. Unlike DFT, it is needed to provide an initial condition as evolution is followed through time.

Theorem IV. *For a given initial state* $\left|\psi_0(\mathrm{r})\right\rangle$ *at* t_0*, the extrema of the quantum mechanical action* $\mathcal{A}[\mathrm{n}]$*, defined as*:

$$\mathcal{A}[\mathrm{n}]=\int_{\mathrm{t}_0}^{\mathrm{t}_1}\left\langle\psi(\mathrm{t})\right|i\frac{\partial}{\partial\mathrm{t}}-\widehat{\mathrm{H}}(\mathrm{t})\left|\psi(\mathrm{t})\right\rangle\mathrm{dt}, \tag{2.34}$$

becomes stationary at the exact time-dependent density $\mathrm{n}_0(\mathrm{r},\mathrm{t})$ *corresponding to the external potential* $\mathrm{V}_0(\mathrm{r},\mathrm{t})$[108]:

$$\left.\frac{\delta\mathcal{A}[\mathrm{n}]}{\delta\mathrm{n}(\mathrm{r},\mathrm{t})}\right|_{\mathrm{n}_0}=0. \tag{2.35}$$

Theorem IV proves that the time-dependent problem can be solved by finding the stationary point of the action $\mathcal{A}$[l].

---

[k] The Bethe-Salpeter approach, within the MB perturbation theory, is based on the solution of the Bethe-Salpeter screened equation (BSE). The correlated electron hole is created and diagonalised in such a way as to give rise to the excitation energies and wavefunctions of the excited states. It is often used on top of the Single-Particle Green Function with Screened Coulomb Interaction (ω) (GW) method, solving the quasiparticle problem when a charge is added to or removed from the system. It is used for getting a good agreement of the theoretical absorption spectrum with the experimental one and requires a high computational effort, so it is beyond the scope of this study.

[l] The definition of the extrema of the quantum mechanical action $\mathcal{A}$, Eq. (2.34), presents the problems of causality violation.

2.7.2 Time-Dependent Kohn-Sham Equations

Referring to what has been done with the energy functional Eq. (2.19), the action functional $\mathcal{A}[n]$ can be decomposed into its subcomponents as:

$$\mathcal{A}[n] = \mathcal{T}_0[n] \underbrace{-\frac{1}{2}\int_{t_0}^{t_1} dt \int\int \frac{n(r,t)n(r',t)}{|r-r'|} drdr'}_{\mathcal{A}_H[n]} + \mathcal{A}_{xc}[n] + \int_{t_0}^{t_1} dt \int V_{ext}(r,t)n(r,t)dr, \tag{2.36}$$

where $\mathcal{T}_0[n]$ is adding and subtracting the kinetic term of the non-interacting KS system, $\mathcal{A}_H[n]$ is the Hartree contribution, and $\mathcal{A}_{xc}[n]$, analogously to conventional DFT, contains all the missing contributions to the functional $\mathcal{A}[n]$. However, there is no complete knowledge of the action functional $\mathcal{A}[n]$. Analogous to the conventional DFT, the time-dependent density can be estimated by considering an auxiliary system of non-interacting electrons moving in the time-dependent effective potential.[111] Hence, the time-dependent KS equation can be written in the following form:

$$\left[-\frac{1}{2}\nabla^2 + V_{eff}([n],\mathbf{r},t)\right]\phi_j(\mathbf{r},t) = i\frac{\partial}{\partial t}\phi_j(\mathbf{r},t), \tag{2.37}$$

where $V_{eff}([n],\mathbf{r},t)$ and $\phi_j(\mathbf{r},t)$ are the time-dependent effective potential[m] and wavefunction, respectively. The density n_0 solution of both the real and fictitious system is given by:

$$n(\mathbf{r},t) = \sum_{j=1}^{N} |\phi_j(\mathbf{r},t)|^2, \tag{2.38}$$

where N is the number of occupied states. Hence, utilising the decomposition of the action functional Eq. (2.36) and the variational principle mentioned in Theorem IV, we derive the following effective potential for the static case:

$$V_{eff}([n],\mathbf{r},t) = V_{ext}(\mathbf{r},t) + \int \frac{n(\mathbf{r}',t)}{|\mathbf{r}-\mathbf{r}'|} d^3r' + V_{xc}([n],\mathbf{r},t). \tag{2.39}$$

So far, the static TDDFT has been improved under the auspicious stewardship of numerous contributions; detailed information about improvements of this theory (for example, the relativistic TDDFT and the finite temperature in thermal equilibrium) can be found in the following Refs. [112–115].

2.7.3 Linear Response Theory

In this part, a summary of the general results of linear response theory will be presented, emphasising its application to optical absorption spectra. The objective of linear response theory is to examine the change of a particular physical observable resulting from the application of a weak external perturbation to a many-particle system. If the time-dependent external potential is weak, the external potential can be presented in the following form:

$$V_{ext}(\mathbf{r},t) = V_{ext}^{(0)}(\mathbf{r}) + V_{ext}^{(1)}(\mathbf{r},t), \tag{2.40}$$

where $V_{ext}^{(0)}(\mathbf{r})$ is the static external potential of the unperturbed system, and $V_{ext}^{(1)}(\mathbf{r},t)$ is the time-dependent perturbation part of the external potential. Hence, the density $n(\mathbf{r},t)$ can be extended in the

---

It is poorly defined and lack of necessary components to construct orbital functional and XC functionals with memory.[109] These problems could be solved in the framework of the time-contour formalism of Keldysh.[110]

[m] This is also known as the time-dependent KS potential, which has the form where the density of the non-interacting system equals the density of the realistic system of interacting electrons. This potential origin for any density $n(r,t)$ can be deduced from Theorem III and thoroughly shown by van Leeuwen in Ref. [110].

Taylor series with response to the perturbation $\mathrm{V}^{(1)}_{\mathrm{ext}}(\mathbf{r},\mathrm{t})$, and it can be practically split into the following *linear* and *non-linear*[n] categories:

$$\mathrm{n}(\mathbf{r},\mathrm{t}) = \mathrm{n}^{(0)}(\mathbf{r}) + \underbrace{n^{(1)}_{\mathrm{ind}}(\mathbf{r},t)}_{linear} + \underbrace{n^{(2)}_{\mathrm{ind}}(\mathbf{r},t) + ...,}_{non-linear} \tag{2.41}$$

where $\mathrm{n}^{(0)}(\mathbf{r})$ is the density of the unperturbed system, $\mathrm{n}^{(1)}(\mathbf{r},\mathrm{t})$ is the first order time-dependent induced density-response, $\mathrm{n}^{(2)}(\mathbf{r},\mathrm{t})$ is the second order time-dependent induced density-response and so on. Suppose that the linear-response theory is handled by considering only the first order induced density-response in Eq. (2.41). In that case, the first order time-dependent induced density can be written in the following form[116]:

$$\mathrm{n}^{(1)}_{\mathrm{ind}}(\mathbf{r},\mathrm{t}) = \int \chi^{(1)}(\mathbf{r},\mathbf{r}',\mathrm{t}-\mathrm{t}')\mathrm{V}_{\mathrm{ext}}(\mathbf{r}',\mathrm{t}')\mathrm{dr}'\mathrm{dt}', \tag{2.42}$$

where $\chi^{(1)}(\mathbf{r},\mathbf{r}',\mathrm{t}-\mathrm{t}')$ is the linear density response function[o], defined as:

$$\chi^{(1)}(\mathbf{r},\mathbf{r}',\mathrm{t}-\mathrm{t}') = \left.\frac{\delta \mathrm{n}(\mathbf{r},\mathrm{t})}{\delta \mathrm{V}_{\mathrm{ext}}(\mathbf{r}',\mathrm{t}')}\right|_{\mathrm{V}_{\mathrm{ext}}(\mathbf{r}',\mathrm{t}')=\mathrm{V}^{(0)}_{\mathrm{ext}}(\mathbf{r}')}. \tag{2.43}$$

The causality paradox requires the linear density response function to be equal to zero at $\mathrm{t} < \mathrm{t}'$ because the density cannot be influenced by later variations of the potential.[116] By analogy with DFT, the density of the real system is considered equal to that of non-interacting KS electrons for the linear density response function calculation. Hence, the induced density is related to the effective potential, which is defined as:

$$\mathrm{n}^{(1)}_{\mathrm{ind}}(\mathbf{r},\mathrm{t}) = \int \chi^{(1)}_0(\mathbf{r},\mathbf{r}',\mathrm{t}-\mathrm{t}')\mathrm{V}_{\mathrm{eff}}(\mathbf{r}',\mathrm{t}')\mathrm{dr}'\mathrm{dt}', \tag{2.44}$$

where $\mathrm{V}_{\mathrm{eff}}$ is given in Eq. (2.39) and $\chi^{(1)}_0(\mathbf{r},\mathbf{r}',\mathrm{t}-\mathrm{t}')$ is the independent-particle polarisation. By applying the "chain rule"[p] for functional derivatives and using the functional relation[q], the linear density response function can be written in the following form:

$$\chi^{(1)}(\mathbf{r},\mathbf{r}',\mathrm{t}-\mathrm{t}') = \int \underbrace{\frac{\delta \mathrm{n}(\mathbf{r},\mathrm{t})}{\delta \mathrm{V}_{\mathrm{eff}}(\mathrm{r}'',\mathrm{t}'')}}_{\chi^{(1)}_0(\mathbf{r},\mathbf{r}'',\mathrm{t}-\mathrm{t}'')} \cdot \frac{\delta \mathrm{V}_{\mathrm{eff}}(\mathrm{r}'',\mathrm{t}'')}{\delta \mathrm{V}_{\mathrm{ext}}(\mathbf{r}',\mathrm{t}')}\mathrm{dr}''\mathrm{dt}'' =$$

$$= \int \chi^{(1)}_0(\mathbf{r},\mathbf{r}'',\mathrm{t}-\mathrm{t}'') \left[\underbrace{\frac{\delta \mathrm{V}_{\mathrm{ext}}(\mathrm{r}'',\mathrm{t}'')}{\delta \mathrm{V}_{\mathrm{ext}}(\mathbf{r}',\mathrm{t}')}}_{1^{\mathrm{st}}\mathrm{term}} + \underbrace{\frac{\delta \mathrm{V}_{\mathrm{H}}(\mathrm{r}'',\mathrm{t}'')}{\delta \mathrm{V}_{\mathrm{ext}}(\mathbf{r}',\mathrm{t}')}}_{2^{\mathrm{nd}}\mathrm{term}} + \underbrace{\frac{\delta \mathrm{V}_{\mathrm{xc}}(\mathrm{r}'',\mathrm{t}'')}{\delta \mathrm{V}_{\mathrm{ext}}(\mathbf{r}',\mathrm{t}')}}_{3^{\mathrm{rd}}\mathrm{term}} \right] \mathrm{dr}''\mathrm{dt}''. \tag{2.45}$$

The first term yields by:

$$\frac{\delta \mathrm{V}_{\mathrm{ext}}(\mathrm{r}'',\mathrm{t}'')}{\delta \mathrm{V}_{\mathrm{ext}}(\mathbf{r}',\mathrm{t}')} = \delta(\mathrm{r}''-\mathrm{r}')\delta(\mathrm{t}''-\mathrm{t}'). \tag{2.46}$$

---

[n] In the case of non-linear optics, the time-dependent higher-order (non-linear) response must be included by computing the higher-order components in Eq. (2.41).[111]

[o] The linear density response function is also called first-order susceptibility, fully interacting density-density response function or reducible polarisability.

[p] $\frac{\delta \mathcal{V}}{\delta \Psi(\mathrm{x})} = \int \frac{\delta \mathcal{V}}{\delta \mathcal{G}(\mathrm{y})} \cdot \frac{\delta \mathcal{G}(\mathrm{y})}{\delta \Psi(\mathrm{x})}\mathrm{dy}$

[q] $\frac{\delta \mathcal{V}(\mathrm{x})}{\delta \mathcal{V}(\mathrm{y})} = \delta(\mathrm{x}-\mathrm{y})$

Since both the Hartree V_H and XC potentials V_{xc} are also functionals of the density, one can apply the chain rule once again and rewrite the second and third terms as:

$$\frac{\delta V_H(r'',t'')}{\delta V_{ext}(\mathbf{r}',t')} = \int \underbrace{\frac{\delta V_H(r'',t'')}{\delta n(r''',t''')}}_{\delta(t''-t''')/|r''-r'''|} \cdot \underbrace{\frac{\delta n(r''',t''')}{\delta V_{ext}(\mathbf{r}',t')}}_{\chi^{(1)}(r''',r',t'''-t')} dr'''dt''' = \int \frac{\delta(t''-t''')}{|r''-r'''|}\chi^{(1)}(r''',r',t'''-t')dr'''dt''' \quad (2.47)$$

and

$$\frac{\delta V_{xc}(r'',t'')}{\delta V_{ext}(\mathbf{r}',t')} = \int \underbrace{\frac{\delta V_{xc}(r'',t'')}{\delta n(r''',t''')}}_{f_{xc}(r'',r''',t''-t''')} \cdot \underbrace{\frac{\delta n(r''',t''')}{\delta V_{ext}(\mathbf{r}',t')}}_{\chi^{(1)}(r''',r',t'''-t')} dr'''dt''' = \int f_{xc}(r'',r''',t''-t''')\chi^{(1)}(r''',r',t'''-t')dr'''dt''', \quad (2.48)$$

where $f_{xc}(r'',r''',t''-t''')$ is the XC kernel in Eq. (2.48). If the results of three terms are combined together, one must get the following relation:

$$\begin{aligned} &\int \chi_0^{(1)}(\mathbf{r},r'',t-t'')\left[\delta(r''-r')\delta(t''-t') + \int \upsilon(r'',r''')\chi^{(1)}(r''',r',t'''-t')dr'''dt''' + \right.\\ &\left. + \int f_{xc}(r'',r''',t''-t''')\chi^{(1)}(r''',r',t'''-t')dr'''dt'''\right] dr''dt'' = \chi_0^{(1)}(r,r',t-t') + \\ &+ \int\int \chi_0^{(1)}(r,r'',t-t'')\left[\frac{\delta(t''-t''')}{|r''-r'''|} + f_{xc}(r'',r''',t''-t''')\right]\chi^{(1)}(r''',r',t'''-t')dr''dr'''dt''dt'''. \end{aligned} \quad (2.49)$$

After using the relation Eq. (2.49) in Eq. (2.45) and performing a Fourier transformation to the frequency domain[r], the linear density response function will be in the following form:

$$\chi^{(1)}(\mathbf{r},\mathbf{r}',\omega) = \chi_0^{(1)}(r,r',\omega) + \int\int \chi_0^{(1)}(r,r'',\omega)\left[\frac{1}{|r''-r'''|} + f_{xc}(r'',r''',\omega)\right]\chi^{(1)}(r''',r',\omega)dr''dr'''. \quad (2.50)$$

This Eq. (2.50) is also called the Dyson-like screening equation. Eq. (2.50), assuming a periodic crystal and space Fourier transform, can be rewritten in the reciprocal space[116]:

$$\chi^{(1)}_{G,G'}(\mathbf{q},\omega) = \chi^{(1)}_{0_{G,G'}}(\mathbf{q},\omega) + \sum_{G_1,G_2} \chi^{(1)}_{0_{G,G_1}}(\mathbf{q},\omega)[\upsilon_{G_1}(\mathbf{q})\delta_{G_1,G_2} + f_{xc_{G_1,G_2}}(\mathbf{q},\omega)]\chi^{(1)}_{G_2,G'}(\mathbf{q},\omega), \quad (2.51)$$

where the G and G′ are the reciprocal lattice vectors, and q is the wavevector in the Brillouin zone (BZ). By considering the Fourier coefficients $\chi^{(1)}_{0_{G,G'}}(\mathbf{q},\omega) = \chi(q+G,q+G',\omega)$[117, 118], $\chi^{(1)}_{0_{G,G'}}(\mathbf{q},\omega)$ is calculated by summing the transitions between KS states as:

$$\chi^{(1)}_{0_{G,G'}}(\mathbf{q},\omega) = \frac{1}{N_\mathbf{k}\Omega}\sum_\mathbf{k}\sum_{\upsilon,c}\frac{(f^\upsilon_\mathbf{k} - f^c_{\mathbf{k}+\mathbf{q}})}{\varepsilon^\upsilon_\mathbf{k} - \varepsilon^c_{\mathbf{k}+\mathbf{q}} + \omega + i\eta}\cdot\langle\varphi^\upsilon_\mathbf{k}|e^{-i(\mathbf{G}+\mathbf{q})\cdot\mathbf{r}'}|\varphi^c_{\mathbf{k}+\mathbf{q}}\rangle\langle\varphi^c_{\mathbf{k}+\mathbf{q}}|e^{i(\mathbf{G}'+\mathbf{q})\cdot\mathbf{r}}|\varphi^\upsilon_\mathbf{k}\rangle \quad , \quad (2.52)$$

where Ω is the volume of the unit cell in real space, k refers to the k-point grid of the 1st (irreducible) BZ, and N_k is the number of these points. υ and c are the states between which the transition is calculated. These quantities characterise the microscopic phenomena. The knowledge of $\chi^{(1)}_{G,G'}(\mathbf{q},\omega)$ gives access to the inverse dielectric function in the momentum space, which reads as:

$$\varepsilon^{-1}_{G,G'}(\mathbf{q},\omega) = \delta_{G,G'} + \upsilon_G(\mathbf{q})\chi^{(1)}_{G,G'}(\mathbf{q},\omega), \quad (2.53)$$

where $\upsilon_G(\mathbf{q}) = 1/|q+G|^2$ is the Fourier transform of the Coulomb potential. These properties characterise the microscopic phenomena. Once the microscopic dielectric function has been determined,

---

[r] The time Fourier transform gives a one-frequency dependence because of the time invariance.

it is necessary to obtain measurable quantities. The microscopic inverse dielectric function gives access to the absorption spectrum defined as the imaginary part of the macroscopic dielectric function: $\mathrm{Im}[\varepsilon_{\mathrm{M}}(\omega)]$. Within TDDFT, the macroscopic dielectric function $\varepsilon_{\mathrm{M}}(\omega)$ can be calculated by using the following formula[117, 118]:

$$\varepsilon_{\mathrm{M}}(\omega) = \lim_{\mathbf{q}\to 0} \frac{1}{\varepsilon^{-1}_{\mathrm{G,G'}}(\mathbf{q},\omega)}\bigg|_{\mathrm{G,G'}=0}. \tag{2.54}$$

In order to calculate optical properties, some approximations are needed in the Dyson-like Eq. (2.51). For simplicity, let us rewrite this equation without indexes in the short following notation:

$$\chi^{(1)} = \chi_0^{(1)} + \chi_0^{(1)}[\upsilon + \mathrm{f_{xc}}]\chi^{(1)}. \tag{2.55}$$

Eq. (2.55) can be solved by inversion and is exact in the framework of the linear response theory. The Coulomb potential υ is responsible for the so-called Local Field Effect (LFE)[s], and the XC kernel $\mathrm{f_{xc}}$[t] includes all the difficulties of XC in the dynamical linear regime.

The simplest approximation in optical calculations consists of setting υ and $\mathrm{f_{xc}}$ terms to zero, also known as the Independent-Particle Approximation (IPA).[116] The differences between the empty and filled KS energy levels used to construct the independent particle polarisation $\chi_0^{(1)}$ determine the excitation energies in the IPA. This approximation results in absorption peaks that are generally red-shifted relative to experimental spectra[119] because of the band gap problem[u] of DFT. By neglecting only the XC kernel ($\mathrm{f_{xc}} = 0$) in Eqs. (2.50-2.55), one uses the Random-Phase Approximation (RPA). In this situation, just the classical Coulomb term is considered as part of the total kernel in Eqs. (2.50-2.55). This term characterises the well-known Lindhard theory of screening with the addition of LFE.[123] Despite its simplicity, the RPA produces reasonable results for numerous systems. In addition to IPA and RPA, there are more advanced approximations, for instance, based on the functional derivative of $\mathrm{V_{xc}^{LDA}}$ with respect to the electronic density. This approximation is named the Adiabatic Local Density Approximation (ALDA).[124, 125]

2.8 Numerical Technical Aspects

The KS formalism needs many techniques and numerical algorithms to solve the set of N coupled, three-dimensional, partial differential equations self-consistently. In this thesis, the Plane-Wave (PW) basis sets with *Pseudopotential* (PP) methods are used in Vienna *ab initio* simulation package (VASP)[126] and Quantum ESPRESSO (QE)[127, 128], and the Atomic Orbital (AO) basis sets are used in ORCA quantum chemistry program (ORCA)[129]. Just once, the objective is not to survey every detail of the code's numerical machinery but rather to illustrate, in a broad sense, the most critical aspects of the methodology.

2.8.1 Basis Sets

In practice, to solve the KS Eqs. (2.17-2.19), the KS wavefunctions $\psi_{\mathrm{n}}(\overrightarrow{r}) = \sum_\alpha \mathrm{C}_{\mathrm{n}\alpha}\phi_\alpha(\overrightarrow{r})$ must be spanned in Hilbert space with a complete basis sets $\phi_\alpha(r)$: localised and delocalised, suitable for the system under study. Using a basis set permits the transformation of the solution of an ongoing issue into the process of finding the coefficients of the expansion $\mathrm{C}_{\mathrm{n}\alpha}$. A significant part of the numerical procedures used to solve KS equations is determined by choice of the basis set. Consequently, this

---

[s] It describes the fluctuations of induced electronic density at the microscopic scale, which correlates to the atomic structure of matter.

[t] The XC kernel is unknown in practice and suitable approaches need to be found to identify it.

[u] The gap between filled and empty states is substantially underestimated.[120–122]

decision remains fundamental for developing a particular DFT code. The two primary types of basis sets are AO and PW:

- AO basis sets[v]:
  - Localised basis:
    - Slater-type Orbitals [130]
    - Gaussian-type Orbitals [131]
    - Linear Combinations of AO [132, 133]
    - Linearised Muffin-Tin Orbitals [134, 135]
    - Smart Local Orbitals [136]
- PW basis sets:
  - Delocalised basis PW [137]
  - Mixed of Localised and Delocalised basis:
    - Linearised Augmented PW [138]
    - Projected Augmented Wave Method (PAW) [139]

In this thesis, both AO and PW basis sets are utilised depending on the investigated systems. The choice of basis sets offers some advantages and disadvantages in itself.

- Advantages of AO basis sets:
  - The convergence with regard to the size of the basis set is rapid, requiring just a few functions per atom.
  - The difficulty of describing orbitals near the core is much less than describing PWs.
  - Finite systems such as molecules and clusters can be dealt with simply because they do not populate the vacuum as PWs do.

In principle, the selection of AO basis functions firmly depends on the purposes and systems. Detailed information about the AO basis sets is given in Ref. [140] and references therein. A comprehensive discussion of AO basis sets is beyond the scope of this thesis; suffice it to note that Gaussian basis sets of triple zeta valence (def2-TZVP)[141] can be used for general-purposes in DFT and TDDFT computations.

- Advantages of PW basis sets:
  - Contrary to AO basis sets, the PW basis sets are an excellent choice for the description of solids in particular, as PWs possess the periodicity of solids thanks to the Bloch theorem.[142] An electron moving in the effective potential $\mathrm{V_{eff}(r)}$ with the periodicity of the crystal $\mathrm{V_{eff}(r+R) = V_{eff}(r)}$, where R is the radius vector of the unit cell, can be defined by the following wavefunction:

$$\psi_{\mathrm{n,k}}(\vec{r}) = \frac{1}{\sqrt{\mathrm{N_k}\cdot\Omega}} \mathrm{e}^{\mathrm{i}\mathrm{k}\cdot\vec{r}} \sum_{\mathrm{G}}^{\infty} \mathrm{C_{n,k+G}}\cdot\mathrm{e}^{\mathrm{iG}\cdot\vec{r}}. \tag{2.56}$$

    Here, n is the energy band index, k is wave-vectors lying inside the 1st BZ, and Ω, $\mathrm{N_k}$ and G are the volume of the Wigner-Seitz cell, the number of k-points considered, and the vector of the reciprocal lattice, respectively.

---

[v] Atomic orbitals can be represented generally as follows: $\phi_\alpha(\vec{\mathrm{r}}) = \mathrm{R}(|\vec{\mathrm{r}}_\mathrm{I}|)\mathrm{Y}_{l,m}(\hat{\mathrm{r}}_\mathrm{I})$, where $\mathrm{R}(|\vec{\mathrm{r}}_\mathrm{I}|)$ is the radial part of the function and $\mathrm{Y}_{l,m}(\hat{\mathrm{r}}_\mathrm{I})$ is a spherical harmonic of the order l with angular momentum m. Depending on the function employed for the radial part of the function, atomic orbitals can be classified as Slater-type orbitals ($\mathrm{e}^{-\xi\mathrm{r}}$), Gaussians orbitals ($\mathrm{e}^{-\alpha\mathrm{r}^2}$) or numerical orbitals.

- PW basis sets are mutually orthogonal, simplifying the evaluation of derivatives and integrals and and facilitating the calculation of Hamiltonian matrix elements. Contrary to AO basis sets, they do not suffer from basis set superposition error because of orthogonal.
- They permit the use of Fast Fourier Transform formalism to easily transition from the direct to the reciprocal space and vice versa.
- Since there is no Pulay term[w], it is simple to compute atomic forces.
- The convergence quality can be easily evaluated for total energy calculations without ambiguity by increasing the kinetic-energy cutoff:

$$\frac{1}{2}|\mathrm{k}+\mathrm{G}|^2 \leq \mathrm{E}_{\mathrm{cut}}, \tag{2.57}$$

which is correlated to the number of PW on the basis by the relation $\mathrm{N}_{\mathrm{PW}} \simeq \Omega \cdot \mathrm{E}_{\mathrm{cut}}^{\frac{3}{2}}$.

2.8.2 K-point Grid

Calculating the ground state charge density from Bloch's states $\psi_{\mathrm{i,k}}(\vec{r})$, the ground-state DFT calculation requires evaluating integrals over a grid of k-points in the 1st BZ:

$$\mathrm{n}(\vec{r}) = \frac{\Omega}{8\pi^3} \int_{\mathrm{BZ}} \sum_{\mathrm{i}} |\psi_{\mathrm{i,k}}(\vec{r})|^2 \mathrm{dk}. \tag{2.58}$$

In order to execute a numerical computation, the integral must be transformed back into a sum over a set of weighted k-points. Firstly, Baldereschi introduced the idea of special k-points.[144] Later, Chadi-Cohen[145] and Monkhorst-Pack (MP)[146] expounded on this idea, and their strategies are now extensively utilised. Compared to an arbitrary grid of points that do not represent the symmetries of the BZ, the special k-points dramatically reduce the number of points required to calculate integrals with a certain degree of precision. In addition, the resultant inaccuracy can be minimised systematically by increasing the density of the particular point grid.

2.8.3 Pseudopotential Approximation

In the PW basis set, the KS equations can be solved very efficiently. However, it is worth noting that the electronic wavefunctions become rapidly oscillating functions when approaching the nuclei. Hence, a huge number of PWs is required to describe such oscillations - a computationally demanding task. Moreover, the energy of the core states is on the order of KeV, whereas the relevant bonding energies are in the range of eV: a high relative precision for total energy is required, even when only differences are of interest. Nevertheless, this problem can be overcome by using the PP approximation,[147–149] see Figure 2.4. Furthermore, the fact that the valence electrons of each atom dominate chemical binding in molecules and solids has also stimulated the development of PPs. The core electrons feel a stronger binding Coulomb potential because their proximity to the nucleus makes these electrons only weakly chemically active.[x][147–149]

This resulted in the concept of replacing the whole cluster consisting of the core and the tightly bound electrons with an effective ionic potential that operates on the valence electrons while still accounting for Pauli exclusion. In an auxiliary atomic calculation for the element of interest, these PPs can be constructed and then used in subsequent molecular or solid computations. In this way, it is assumed that the core electrons are effectively frozen because their orbitals cannot shift while the effective ionic potential remains constant.[y] This type of PP is categorised as *norm-conserving pseudopotential* (NC-PP)

---

[w] Pulay forces occur while evaluating derivatives of localised basis set functions with regard to atomic positions.[143] When the PW basis set is utilised, the Pulay forces do not exist.

[x] Due to the negligible effect of the external potential on the core-electron dynamics, the inner lying atomic orbitals found solely in isolated atoms are only minimally altered and yet provide a decent approximation of core electron wavefunctions.

[y] It is generally called frozen-core approximation. Similar to what had been done for nuclei within the BO approximation.

if the pseudo-wavefunction they generate agrees well with the real one at distances farther than a defined cutoff radius r_c from the potential origin, that is, the core.[149] The NC-PPs are transferrable; that is, they present the scattering properties of the real potential over a broad energy range and are reasonably smooth.[150] However, NC-PPs require large PW basis sets, resulting in high computational and memory requirements. Hence, *ultra-soft pseudopotential* (US-PP) was developed to circumvent this issue, and US-PPs require a significantly lower energy cutoff than NC-PPs.[151]

Although both NC-PPs and US-PPs are relatively simple to process computationally and in good agreement with all-electron calculations for most cases, eliminating all near-core physics and replacing it with a black box that does nothing but provide the illusion that everything is the same at a sufficient distance from it may nonetheless appear to be a somewhat coarse-grained activity. It is particularly critical when researching physical properties in the core region. This scenario is considerably better treated by the PAW method, which was first developed by Blöchl[139] and later modified by Kresse and Joubert[152] for PW computations. Besides, there are various *ab initio* PPs satisfying additional conditions such as scalar relativistic and fully relativistic.[153–157]

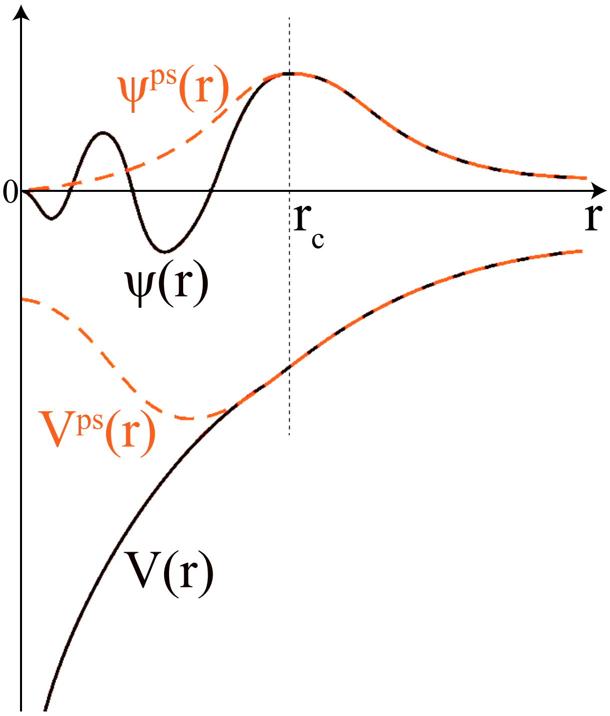

Figure 2.4: Schematic representation of the replacement of all-electron potential $V(r)$ and wavefunction $\psi(r)$ (solid lines) by a fictitious PP $V^{ps}(r)$ and pseudo-wavefunction $\psi^{ps}(r)$ (dashed lines), respectively. The PP and wavefunction become virtually indistinguishable outside a sphere with radius r_c around the origin. This is the fundamental idea of the PP approximation. Schematic representation is adapted with respect to the original description in Ref. [148].

2.8.4 The Dispersion Correction

Conventional DFT describes the effective electron interaction at short inter-atomic distances rather well because of their deep relation to the corresponding electron density changes. In inhomogeneous materials and weakly bonded systems, the LR electron correlation effect cannot be effectively characterised by local or semi-local XC functionals. Especially the significance of weak intermolecular interactions can even surpass that of chemical bonds in crystalline assemblies.[158] They are either kept together by electrostatic and polarisation interactions or by London dispersion forces[z] in their (near) absence.[160] Therefore, it would be advantageous to have a technique adequate for describing vdW interactions.

---

[z] London dispersion forces are one of the three classes of van der Waals (vdW) interactions occurring between atoms and molecules.[159] Attractive or repulsive, vdW forces can be subdivided into three distinct phenomena[160]:

- the interaction between two permanent dipoles - the Keesom interaction;
- the interaction between a permanent dipole and a polarisable atom producing an induced dipole - the Debye interaction;
- the interaction of two instantaneous dipoles is formed arising from fluctuations in the distribution of electronic charge - the London dispersion interaction;

In the most atoms and molecules, dispersion forces are the strongest of these three contributions. The interaction occurs when the outer electrons of nearby molecules reject each other and attempt to flee. This results in an immediately induced dipole, which is an oscillating redistribution of electron density within a molecule. The impact is more pronounced for larger atoms with larger shells, and it is also proportional to the amount of surface contact. The force is referred to as dispersive, strongly dependent on the fluctuating frequency of electrons.

Although significant progress has been made in discovering a fully *ab-initio* treatment of dispersion forces utilising quantum Monte-Carlo methods[161] and the combination of exact XC energy within the adiabatic-connection fluctuation-dissipation theorem[162], it is computationally so expensive to be used regularly on larger systems.[163–167] However the most reasonable possibility to emerge from this domain is the so-called DFT+vdW-scheme, combining conventional DFT-functionals plus the longest ranged or most non-local energy terms.[168–171] Despite the quantum-mechanical origin of the electron correlation, according to this method, it is conceivable to interpret vdW interactions as an interaction between instantly fluctuating dipoles. It considers the type of atoms present as well as their interatomic distances. For a periodic N-atom system, the expression of dispersive interaction energy can be defined in the following general form:

$$\mathrm{E_{disp}} = -\sum_{\alpha,\beta}^{\mathrm{N}}\sum_{\mathrm{T}} \mathrm{s_n}\frac{\mathrm{C}_{\mathrm{n}}^{\alpha\beta}}{|\mathrm{r}_{\alpha,0}-\mathrm{r}_{\beta,\mathrm{T}}|^{\mathrm{n}}}\mathrm{f}_{\mathrm{dmp}}^{(\mathrm{n})}(|\mathrm{r}_{\alpha,0}-\mathrm{r}_{\beta,\mathrm{T}}|). \qquad (2.59)$$

Here, the $\mathrm{s_n}$ represents that the scaling coefficient is set to unity to ensure the correct LR behaviour, $\mathrm{C}_{\mathrm{n}}^{\alpha\beta}$ denotes dipole-dipole (n=6) and dipole-quadrupole (n=8) dispersion coefficient for α and β atoms pair, $\mathrm{r}_{\alpha,0}$ is the position vector of the atom α in the unit cell at 0 and $\mathrm{r}_{\beta,\mathrm{T}}$ that of atom β in the unit cell reached by considering all translation invariant vectors T inside a cut-off sphere. In order to prevent near-singularities for small inter-atomic distances, a damping function $\mathrm{f}_{\mathrm{dmp}}^{(\mathrm{n})}(|\mathrm{r}_{\alpha,0}-\mathrm{r}_{\beta,\mathrm{T}}|)$ must be employed in semi-empirical DFT descriptions of dispersive interactions. In order to handle systems with vdW-controlled characteristics in DFT, various approaches have been progressively developed and studied so far.[170–182]

> *"It does not make any difference how beautiful your guess is, it does not make any difference how smart you are, who made the guess, or what his name is. If it disagrees with experiment, it is wrong."*
>
> — Richard Feynman,
> *Messenger Lectures on The Character of Physical Law,*
> *Cornell, 9 November 1964.*

3

Exchange and Correlation beyond Density-Functional Theory

The simplest approximations (LDA and GGA) on the few rungs of Jacob's ladder mentioned in the previous chapter have an excellent accuracy to computational cost ratio. However, the DFT with this class of XC functionals exhibits remarkable failures because of the SIE. In this context, Hubbard-corrected DFT and hybrid functionals will be discussed in this section because both of them can effectively counteract electronic self-interaction.

3.1 The Self-Interaction Error

Despite the various yet justified approximations included in Section 2.4's formulation of DFT, none has a more significant impact on the qualitative dependability of computations than the approximation to the XC functional. Furthermore, all approximated XC functionals are known to be susceptible to the SIE[a], as each electron resides in the field of all electrons, including itself, and can thus be residually interacted with itself. The SIE[185–189] has a quantitative energetic consequence as a deviation from linearity concerning exact piecewise linear behaviour,[190] and by this derivative discontinuity[191–193] with fractional addition or subtraction of an electron.

Despite the remarkable success of local and semi-local XC functionals such as LDA and GGA, they display a convex deviation[b][194–196] from piecewise-linearity, see Figure 3.1. The SIE in DFT leads to several certain problems in predicting band-gaps,[196, 197] dissociation energies,[198, 199] and EA[200]. Hence, it can

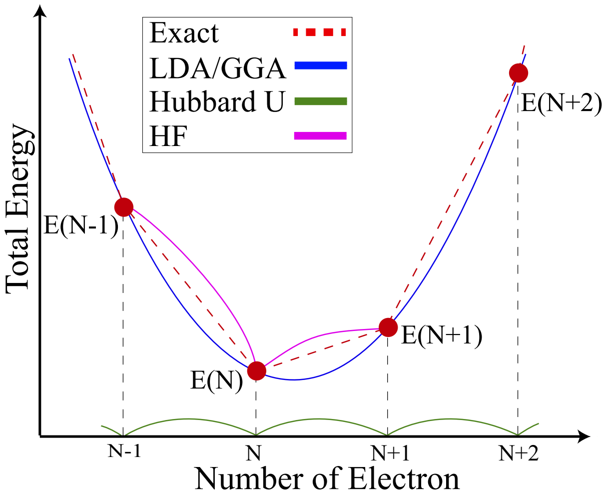

Figure 3.1: Schematic representation of the total energy profile as a function of the number of electrons in a generic atomic system in contact with a reservoir. The blue line represents the DFT energy in practical exchange-correlation functionals such as LDA and GGA; the red dashed line represents the exact limit as the correct piecewise linear behaviour, and the green line is Hubbard U correction in the atomic limit, the pink line is HF energy, adapted from Refs. [183, 184].

---

[a] It is also referred to as delocalization error.

[b] A physical interpretation of the discontinuity in the derivative provides the insight that a fractional electron number from the (wrong) convex behaviour of the XC functional would minimise the energy of the system, resulting in an incorrect delocalisation of the electrons.

be apparent that one obvious way to account for self-interaction error correction (SIC) in DFT calculations is to use better XC functionals. In this respect, the Hubbard U correction and hybrid functionals are generally expected to lead to improved results at a reasonable computational cost.

3.2 Hubbard U correction

The Hubbard U correction was suggested to accurately describe strongly correlated behaviour in materials known as Mott insulators.[c][201] It is one of the simplest models[202] formulated to rationalise the physics of correlated materials, and its real-space second quantisation formalism perfectly describes systems with electrons localised on atomic orbitals.[d]

When the SIE can be adequately assigned to highly localised orbitals, a well-established and computationally efficient methodology for correcting it is the DFT+U method.[203] It is one of the favoured approaches for correcting the SIE.[204–211] By explicitly including an atomic-like Coulomb contact on-site, the DFT+U approach enables the occupation of a collection of localised orbitals to be tailored to a more physical description than DFT alone. The general form of DFT+U energy functional is in the following form:

$$\mathrm{E_{DFT+U}}[\mathrm{n}(\mathbf{r})] = \mathrm{E_{DFT}}[\mathrm{n}(\mathbf{r})] + \mathrm{E_{Hub}}[\{\mathrm{n}^{\mathrm{m}}_{\mathrm{I},\sigma}\}] - \mathrm{E_{dc}}[\{\mathrm{n}_{\mathrm{I},\sigma}\}], \tag{3.1}$$

where $\mathrm{E_{Hub}}[\{\mathrm{n}^{\mathrm{m}}_{\mathrm{I},\sigma}\}]$ denotes a Hubbard term which is added to account for localisation phenomena and correct the SIE, and $\mathrm{E_{dc}}[\{\mathrm{n}_{\mathrm{I},\sigma}\}]$ denotes a double counting term which is eliminated to remove interaction already accounted for in DFT. The Hubbard and double counting terms contribution for each Hubbard atom and sub-shell must be identified. Generally, the double counting term is derived from the fully localised limit[208], and it is specified concerning the on-site Coulomb U and exchange J parameters:

$$\mathrm{E_{dc}}[\{\mathrm{n}_{\mathrm{I},\sigma}\}] = \frac{\mathrm{U}}{2}\mathrm{n_I}(\mathrm{n_I}-1) - \frac{\mathrm{J}}{2}\left[\mathrm{n}_{\mathrm{I},\uparrow}(\mathrm{n}_{\mathrm{I},\uparrow}-1) + \mathrm{n}_{\mathrm{I},\downarrow}(\mathrm{n}_{\mathrm{I},\downarrow}-1)\right], \tag{3.2}$$

where $\mathrm{n_I} = \sum_{\mathrm{m},\sigma} \mathrm{n}^{\mathrm{m},\mathrm{m}'}_{\mathrm{I},\sigma}$ denotes the total number of electrons, $\mathrm{n}_{\mathrm{I},\uparrow}$ and $\mathrm{n}_{\mathrm{I},\downarrow}$ are spin-up and spin-down electrons, respectively. While comparing the DFT total energy with the piecewise linear behaviour of the exact energy, the parabolic deviation with almost constant height U/2 is observed; see Figure 3.1. It is easy to understand that if the DFT energy profile is represented by a parabola, the correction required to recover the physical piecewise linear behaviour (green curve) has the expression of the first part of Eq. (3.2), provided that U represents the (spurious) curvature of the approximate total energy profile one aims to eliminate. Second part of Eq. (3.2) is (empirical) extension for spin-polarised systems.

---

[c] In transition metal oxides materials, the insulating nature of the ground state is due to the high Coulomb repulsion between electrons, prevailing over their kinetic energy (minimised by delocalisation) and compelling the electrons to locate on atomic-like orbitals (Mott localisation). In fact, the LDA and GGA fail to predict the insulating nature of these materials and provide a poor representation of their equilibrium crystal structure, vibrational spectrum and magnetic moments.

[d] The Hubbard Hamiltonian is defined as follows for the electronic structure of solids, considering both fully itinerant and fully localised states:

$$\hat{\mathrm{H}}_{\mathrm{Hub}} = -\mathrm{t}\sum_{\langle \mathrm{i,j}\rangle}\sum_{\sigma}(\hat{\mathrm{c}}^{+}_{\mathrm{i},\sigma}\hat{\mathrm{c}}_{\mathrm{j},\sigma} + \mathrm{h.c.}) + \mathrm{U}\sum_{\mathrm{I}}\hat{\mathrm{n}}_{\mathrm{I},\uparrow}\hat{\mathrm{n}}_{\mathrm{I},\downarrow},$$

where the $\langle \mathrm{i,j}\rangle$ denotes nearest-neighbour lattice sites, $\hat{\mathrm{c}}^{+}_{\mathrm{i},\sigma}$, $\hat{\mathrm{c}}_{\mathrm{j},\sigma}$ and $\hat{\mathrm{n}}_{\mathrm{i},\sigma}$ are, respectively, the creation, annihilation and the spin-density operators for putting an electron of spin σ into an electronic orbital at the I^{th} lattice site (each orbital can hold two electrons). The amplitude of the hopping term t is proportional to the dispersion (the bandwidth) of the valence electronic states, giving the chance of making a hop from one site to the nearest-neighbour site, and U mimics the screened Coulomb repulsion between electrons. The balance between the hopping strength term t and the on-site Coulomb repulsion U governs the behaviour and characteristics of the systems' electronic ground states. In the limit where $\mathrm{t} << \mathrm{U}$, the system becomes an insulator (even under half-filled circumstances, when DFT predicts the system as a metal) because electrons cannot hop around because they lack the energy to surmount the repulsion from neighbouring electrons.

Commonly, a simplifying assumption is to treat parallel spin and anti-parallel spin electrons equivalent with $\mathrm{U_{eff} = U - J}$,[210] and one obtains it as follows:

$$\mathrm{E_{DFT+U} = E_{DFT}} + \frac{1}{2}\sum_{\mathrm{I},\sigma}\sum_{n,l}\mathrm{U}_{\mathrm{I}}^{n,l}\left[\mathrm{Tr}\left(\mathrm{n}_{\mathrm{I},\sigma}^{n,l}\left(1-\mathrm{n}_{\mathrm{I},\sigma}^{n,l}\right)\right)\right], \tag{3.3}$$

where n is the principal quantum number and l is the orbital angular momentum quantum number. The elements of the $\mathrm{n}_{\mathrm{I},\sigma}^{n,l}$ occupation matrix are in general defined via a local projection operator $\hat{\mathrm{P}}_{\mathrm{I},\sigma}^{\mathrm{m,m'}} = |\phi_{\mathrm{I}}^{\mathrm{m'}}\rangle\langle\phi_{\mathrm{I}}^{\mathrm{m}}|$ on the Hubbard manifold.[212] Calculating the projection of all KS states yields the following formula for obtaining the matching $\mathrm{n_{I,\sigma}}$ matrix elements:

$$\mathrm{n}_{\mathrm{I},\sigma}^{\mathrm{m,m'}} = \frac{1}{\mathrm{N_k}}\sum_{\mathrm{k}}^{\mathrm{N_k}}\sum_{\upsilon}\mathrm{f}_{\mathrm{k},\upsilon}^{\sigma}\langle\Psi_{\mathrm{k},\upsilon}^{\sigma}|\phi_{\mathrm{I}}^{\mathrm{m'}}\rangle\langle\phi_{\mathrm{I}}^{\mathrm{m}}|\Psi_{\mathrm{k},\upsilon}^{\sigma}\rangle, \tag{3.4}$$

where υ and σ represent, respectively, the band and spin labels of the KS wavefunctions, k indicates the points in the 1^{st} BZ, and $\mathrm{N_k}$ is the number of K-points, $\mathrm{f}_{\mathrm{k},\upsilon}^{\sigma}$ are the occupations of the KS states, $\phi_{\mathrm{I}}^{\mathrm{m'}}(\mathrm{r})$ is the Bloch sum computed using $\phi_{\mathrm{I}}^{\mathrm{m'}}(\mathrm{r}-\mathrm{R_I})$ which are the localised orbitals cantered on the $\mathrm{I^{th}}$ atom at the position $\mathrm{R_I}$.

As is evident from the formulation of the Hubbard functionals, the "strength" of the correction to DFT total energy functionals is determined by the Hubbard U, the value of which is unknown in advance. It has become a regular practice to adjust the Hubbard U in a semi-empirical way by finding agreement with existing experiments of specific features and utilising them to establish value to predict other properties of the system's behaviour. Furthermore, consistent and reliable techniques for calculating the Hubbard U have also been established to produce quantitatively predicted findings. The linear response approach to compute self-consistently Hubbard U has been recently reported.[183] This method is implemented in the PW PP total-energy code of the QE package[127, 128] and helps to recover the piecewise linearity in transition metal-based materials. Within this approach, the Hubbard parameters are the components of an effective interaction matrix, computed as the difference between bare and screened inverse susceptibilities, as follows:

$$\mathrm{U_I} = (\chi_0^{-1} - \chi^{-1})_{\mathrm{II}}, \tag{3.5}$$

where χ_0 and χ are the susceptibilities measuring the response of atomic occupations to shifts in the potential acting on individual Hubbard manifolds. In particular, χ is defined as:

$$\chi_{\mathrm{IJ}} = \sum_{\sigma,\mathrm{m}}\frac{\mathrm{dn}_{\mathrm{I},\sigma}^{\mathrm{m,m'}}}{\mathrm{d}\alpha_{\mathrm{J}}}, \tag{3.6}$$

where α_{J} is the strength of the perturbation on the $\mathrm{J^{th}}$ site. While χ is evaluated at self-consistency of the linear-response KS calculation, χ_0 is computed before the self-consistent re-adjustment of the Hartree and XC potentials.[183] This process makes it possible to calculate the values of these interactions in dependence on the crystal structure,[213] magnetic phase[214] and chemical transformations[215]. In recent years, this theory has been expanded to correct inter-site electronic hybridisations by DFT+U+V[216] and to account for the over-delocalisation of the electrons in the localised Hubbard manifold within Density Functional Perturbation Theory (DFPT)[217].

3.3 Hybrid DFT

Conventional HF theory neglects the correlation between electrons, resulting in inaccurate estimations of systems' total energies. HF is less precise than even the simplest XC functional approximation (such as

LDA) in KS-DFT for most materials' properties of concern to material scientists. However, inaccuracies are usually in the opposite direction to those produced by LDA/GGA functionals. For example, while LDA/GGA consistently underestimates atomisation energies, HF consistently overestimates them due to conversely over-localising electrons and exhibits concave deviations from piecewise linearity,[184] see Figure 3.1. Consequently, one can think that combining two methods (HF and KS-DFT) must generate superior outcomes thanks to error cancellation, which can be described as follows[e]:

$$E_{xc}^{GH} = E_{xc}^{DFT} + \alpha\left(E_{x}^{HF} - E_{x}^{DFT}\right) = \alpha E_{x}^{HF} + (1-\alpha)E_{x}^{DFT} + E_{c}^{DFT}, \tag{3.7}$$

with α being the "exact exchange" (EXX) mixing ratio, determining the weight of each individual functional are typically stated. The exchange mixing ratio can be defined semi-empirically by fitting the functional's predictions to experimental findings or theoretically verified by using the adiabatic connection formalism.[218, 219] The HF EXX functional is defined as follows:

$$E_{x}^{HF} = -\frac{1}{2}\sum_{i,j}^{occ}\iint \psi_i^{*}(\mathbf{r})\psi_j^{*}(\mathbf{r}')\frac{1}{|r'-r|}\psi_j(\mathbf{r})\psi_i(\mathbf{r}')\,d\mathbf{r}\,d\mathbf{r}' \tag{3.8}$$

The Eq. (3.7) type functional is referred to as a (global) hybrid functional. Currently, the most advanced and commonly used (global) hybrid functionals are the Becke 3-parameter Lee–Yang–Parr (B3LYP)[93, 220, 221] and zero parameter hybrid functional based on PBE (PBE0)[222, 223] functionals.

The B3LYP functional is defined as:

$$E_{xc}^{B3LYP} = a_0E_{x}^{HF} + (1-a_0)E_{x}^{LDA} + a_x(E_{x}^{GGA} - E_{x}^{LDA}) + E_{c}^{LDA} + a_c\left(E_{c}^{GGA} - E_{c}^{LDA}\right), \tag{3.9}$$

where $a_0 = 0.20$, corresponding to 20% HF exchange, and the GGA[f] enhancement factors over LDA[g] are $a_x = 0.72$ and $a_c = 0.81$ for exchange and correlation, respectively. While B3LYP is regularly used to successfully describe organic systems, its direct application to organometallic compounds yields mixed results due to the fact that the LYP-GGA correlation functional does not reproduce the correct limit for the homogeneous system.

The PBE0 hybrid functional is defined in the following form:

$$E_{xc}^{PBE0} = a_0E_{x}^{HF} + (1-a_0)E_{x}^{PBE} + E_{c}^{PBE}, \tag{3.10}$$

where $a_0 = 0.25$, corresponding to 25% HF exchange, 75% PBE type GGA exchange functional along with the full PBE type GGA correlation functional.

Furthermore, it could be potentially improved by using the Meta-GGA exchange functional instead of the GGA exchange functional in the (global) hybrid functional, named the hybrid Meta-GGA. For example, hybrid functional based on Tao–Perdew–Staroverov–Scuseria functional (TPSSh) was slightly better than B3LYP in some cases.[224]

---

[e] For simplicity, the $[n(r)]$ dependence will not be explicitly written in the hybrid functional formulae.

[f] In E_x^{GGA}, the B88[94] type GGA exchange energy are used, as follows:

$$E_x^{GGA}[n(r)] = E_x^{LDA}[n(r)] - \beta\sum_{\sigma}\int n_{\sigma}^{\frac{4}{3}}(r)\frac{x_{\sigma}^{2}}{(1+6\beta x_{\sigma}\sinh^{-1}x_{\sigma})}dr,$$

where this exchange energy is referenced with respect to the LDA energy and is a rescaled integral of the spin density (spin index σ) with a semi-empirical parameter β = 0.0042 a.u.; the variable x_σ is the rescaled gradient of the density as $x_\sigma = \frac{|\nabla n_\sigma(r)|}{n_\sigma^{\frac{4}{3}}(r)}$. In E_c^{GGA}, the LYP[93] type GGA correlation functional is used.

[g] In E_c^{LDA}, the Vosko-Wilk-Nusair (VWN)[87] type LSDA correlation functional is used.

3.4 Range Separated Functionals

Generally, the results of (global) hybrid functional are that the XC mixing parameter is expected to balance the partial elimination of the SIE by using the EXX and incorporating a non-dynamical correlation. However, it causes the wrong asymptotic potential decay $\frac{\alpha}{\mathrm{r}}$, that is, proportional to the fraction of the EXX. As a result, this drawback leads systematically to an underestimation of the energy properties of systems, including reaction barriers and charge-transfer excitations calculations.

The effective method for improving (global) hybrid functional is to maintain GGA exchange at a short range while activating HF exchange asymptotically to achieve the correct asymptotic behaviour, utilising a RS of the electronic interaction.[225–227] This approach consists of a robust approach by splitting the distance-dependent Coulomb repulsion operator into short-range (SR) and LR terms as follows:

$$\frac{1}{|\mathrm{r}-\mathrm{r}'|} = \underbrace{\frac{1-[\alpha+\beta\cdot(1-\xi^{\omega}(|r-r'|))]}{|r-r'|}}_{\mathrm{SR}} + \underbrace{\frac{\alpha+\beta\cdot(1-\xi^{\omega}(|r-r'|))}{|r-r'|}}_{\mathrm{LR}}. \tag{3.11}$$

Commonly, the kernel is chosen as:

$$\xi^{\omega}(|\mathrm{r}-\mathrm{r}'|) = 1-\mathrm{erf}(\omega|\mathrm{r}-\mathrm{r}'|), \tag{3.12}$$

where $\mathrm{erf}(\omega|\mathrm{r}-\mathrm{r}'|)$ is the standard error function,[h] and ω is a range-separation (screening) parameter, which is usually determined empirically, helps to control the ratio between SR and LR contribution. This screening parameter can be seen as the inverse of a smooth cut-off radius, see Figure 3.2. If the electron-electron interaction distance is less than $1/\omega$, the SR contribution is dominant, while the LR contribution is dominant for distances higher than $1/\omega$. When the range separation transformation is applied to the exchange potential, it holds the correct asymptotic behaviour $\frac{1}{\mathrm{r}}$.

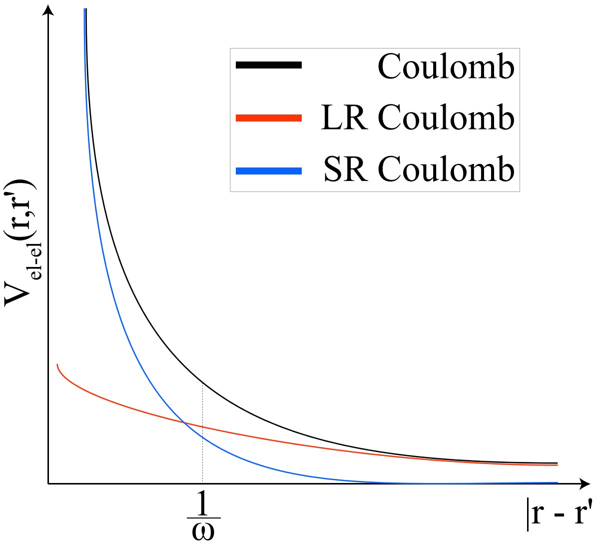

Figure 3.2: Schematic representation of the Coulomb operator into its SR and LR contributions for a given range separation (screening) parameter ω in function of the electron-electron distance $|\mathrm{r}-\mathrm{r}'|$.

Admixing HF EXX into SR and LR separately yields a general expression for a hybrid functional with range-separation[228]:

$$\mathrm{E}_{\mathrm{xc}}^{\mathrm{RS}} = \alpha\mathrm{E}_{\mathrm{x}}^{\mathrm{SR-HF}}(\omega)+(1-\alpha)\mathrm{E}_{\mathrm{x}}^{\mathrm{SR-DFT}}(\omega)+\beta\mathrm{E}_{\mathrm{x}}^{\mathrm{LR-HF}}(\omega)+\beta\mathrm{E}_{\mathrm{x}}^{\mathrm{LR-DFT}}(\omega)+\mathrm{E}_{\mathrm{c}}^{\mathrm{DFT}}, \tag{3.13}$$

where the α and β parameters are adjustable between 0 and 1 for various purposes.

When the parameter β is chosen equal to 0 (excluding the LR contribution of HF EXX), this kind of RS hybrid functional is called as the screening hybrid functional[i], too. Currently, the most effective commonly applied the screening hybrid functional is Heyd–Scuseria–Ernzerhof (HSE)[229, 230], defined as follows:

$$\mathrm{E}_{\mathrm{xc}}^{\mathrm{HSE}} = \alpha\mathrm{E}_{\mathrm{x}}^{\mathrm{HF,SR}}(\omega)+(1-\alpha)\mathrm{E}_{\mathrm{x}}^{\mathrm{PBE,SR}}(\omega)+\mathrm{E}_{\mathrm{x}}^{\mathrm{PBE,LR}}(\omega)+\mathrm{E}_{\mathrm{c}}^{\mathrm{PBE}}, \tag{3.14}$$

where $\alpha = 0.25$, corresponding to 25% HF exchange, 75% PBE type GGA exchange functional along with the full PBE type GGA correlation functional, the screening parameters are chosen 0.15 and 0.11

---

[h] The error function is defined as $\mathrm{erf}(\omega\mathrm{r}) = 1-\frac{2}{\sqrt{\pi}}\int_{\omega\mathrm{r}}^{\infty}\mathrm{e}^{-\mathrm{t}^2}\mathrm{dt}$. In the latter case, the kernel is also chosen as a $\mathrm{e}^{-\omega\mathrm{r}}$ exponential function, so it called as Yukawa screening.

[i] It is also called as SR hybrid functional in literature.

bohr^{-1} for HSE03[229] and HSE06[230] functionals. With comparing (global) hybrid functional, the screening hybrid functionals reduce significantly the computational cost of extended and solid systems[j], particularly those with a small band gap.[231, 232]

When α and β satisfy the following conditions: $0 < \alpha \leq 1$ and $0 < \beta \leq 1$, this kind of RS hybrid functional is called as the LR corrected hybrid functional. Currently, the most effective commonly applied LR-corrected hybrid functional is Coulomb attenuating method (CAM)-B3LYP functional[233, 234] with the following form:

$$\mathrm{E}_{\mathrm{xc}}^{\mathrm{CAM-B3LYP}} = \alpha \mathrm{E}_{\mathrm{x}}^{\mathrm{HF}} + \beta [\mathrm{E}_{\mathrm{x}}^{\mathrm{LR-HF}}(\omega) - \mathrm{E}_{\mathrm{x}}^{\mathrm{LR-GGA}}(\omega)] + (1-\alpha)\mathrm{E}_{\mathrm{x}}^{\mathrm{GGA}} + \delta \mathrm{E}_{\mathrm{c}}^{\mathrm{GGA}} + (1-\delta)\mathrm{E}_{\mathrm{c}}^{\mathrm{LDA}}, \quad (3.15)$$

where $\alpha = 0.19$, corresponding to 19% HF exchange, and $\beta = 0.46$, corresponding to 46% LR HF exchange, and the B88[94] functional is chosen for GGA exchange functional, $\delta = 0.81$, corresponding to 81% LYP type GGA[93] and to 19% VWN[87] type LDA correlation functionals, $\omega = 0.33$ are used. The fundamental band gap and optical excitation energy calculated using CAM-B3LYP functional are much closer, respectively, to that observed than the available GW and GW-BSE results (for example 2D BN material) and require much fewer computational resources.[233] Furthermore, the investigation of CAM-B3LYP functional on charge transfer energies of molecules suggests that chemical precision is achievable around 0.1 eV.[234] In the literature, there are other examples of LR-corrected hybrid functional, such as hybrid functional based on Becke-1997 functional (ωB97) and ωB97X.[k]

Generally, TDDFT calculations with LR-corrected hybrid functionals can provide the following advantages[234–238]:

- the accurate Rydberg excitation energies;
- the same order of calculated oscillator strengths for all molecules;
- the accurate charge-transfer excitation energies;

Although RS hybrid functional works very well in the asymptotic range, problems persist over short distances. Therefore, it has been improved to present the outstanding performance by using LR-corrected double hybrid functionals[l][239, 240], which are also categorised onto the five rungs of Perdew's metaphorical "Jacob's ladder". The application of LR-corrected double hybrid functional is beyond the scope of this thesis since good and reliable results are considered with a more affordable computational cost.

---

[j] SR HF exchange are only considered in screening hybrid functional, and the effects in the solid are more sensitive to descriptions of dynamic correlation.

[k] There are including 100% HF for LR exchange and applying B97 type GGA for SR XC in ωB97 and ωB97X hybrid functionals,[235] and they are defined as follows, respectively:

$$\mathrm{E}_{\mathrm{xc}}^{\omega\mathrm{B97}} = \mathrm{E}_{\mathrm{x}}^{\mathrm{LR-HF}}(\omega) + \mathrm{E}_{\mathrm{x}}^{\mathrm{SR-B97}}(\omega) + \mathrm{E}_{\mathrm{c}}^{\mathrm{B97}} \quad (3.16)$$

and

$$\mathrm{E}_{\mathrm{xc}}^{\omega\mathrm{B97X}} = \gamma \mathrm{E}_{\mathrm{x}}^{\mathrm{SR-HF}}(\omega) + \mathrm{E}_{\mathrm{x}}^{\mathrm{LR-HF}}(\omega) + \mathrm{E}_{\mathrm{x}}^{\mathrm{SR-B97}}(\omega) + \mathrm{E}_{\mathrm{c}}^{\mathrm{B97}}. \quad (3.17)$$

In here, the parameter γ is chosen equal to 0.16, and the range separation ω parameter is chosen equal to 0.4 and 0.3 bohr^{-1} for ωB97 and ωB97X functional, respectively. These functionals are also good in performance for dissociation and charge-transfer problems that are sensitive to the SIE.

[l] They even rival common wave function-based approaches (for example, Coupled Cluster single-double, second-order Møller–Plesset perturbation theory or better).

"The non-physicist finds it hard to believe that really the ordinary laws of physics, which he regards as the prototype of inviolable precision, should be based on the statistical tendency of matter to go over into disorder."

— Erwin Schrödinger,
Book: What Is Life? The Physical Aspect of the Living Cell,
Dublin, September 1967.

4

Application and Results

In this chapter, the applications of the theories and methodologies described in Chapters 2 and 3 are presented to investigate some systems. In section 4.1, the applications of Hubbard U correction and the hybrid functional approaches are presented to describe the structural, electronic, and optical properties of the three major phases of TiO_2 crystals and amorphous titania thin film. In section 4.2, the results about the structural, electronic and the excitation energies of the bare titania clusters and the titania/graphene composites are analysed by using DFT, the hybrid functional approaches, and CDFT. Finally, in section 4.3, DFT and TDDFT calculations are presented on the electronic and optical absorption properties of the series of new organic D-π-A dyes incorporating a diquat (DQ) moiety using LR-corrected hybrid functional and confirm they exhibit intramolecular charge transfer (ICT) behaviour.

4.1 Titania[a]

Titania, TiO_2, has promising energy and environmental applications including the utilisation of solar energy for photocatalysis[241–249] and photovoltaics[249–251] as well as in electronic devices[252–254]. It appears in multiple polymorphs, the most common ones being Rutile (R), Anatase (A), and Brookite (B) (see Figure 4.1), occurring naturally in minerals.[255–258]

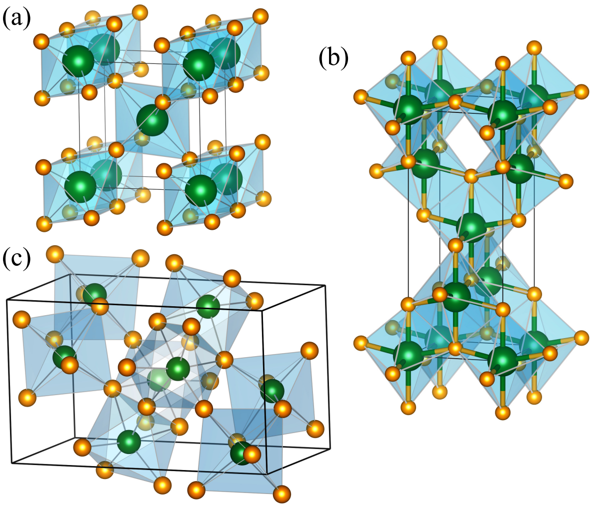

Figure 4.1: Atomic structures of the (a) rutile, (b) anatase, and (c) brookite polymorph of titania. Green and orange spheres represent Ti and O atoms, respectively. Polyhedra indicate the direct neighbourhood of each Ti atom defined by the nearest O atoms.

4.1.1 Overview

Photoemission spectroscopy measurement reveals that the electronic band gap of R- and A-TiO_2 equals 3.30[259] and 3.47[260] eV, respectively. The conduction band of R-TiO_2 is approximately 0.2 eV higher than that of A-TiO_2, as shown by work function measurements.[261] We are unaware of any photoemission measurements on B-TiO_2. Nonetheless, measurements of the optical gaps for all three polymorphs are available; they

---

[a] The results presented in this section have been submitted to a peer-reviewed scientific journal.

are stated to be ~3.0 eV,[262–265] 3.4 eV,[264–266] and 3.3 eV[267, 268] for R-, A-, and B-TiO_2, respectively. These gap sizes necessitate additional efforts to sensitise TiO_2 based materials for solar radiation below the Ultraviolet (UV) region of the electromagnetic spectrum to activate their useful functionalities by photoinduced charge carriers.[269–272]

Computational investigations significantly help and guide corresponding experimental works.[271–276] Particularly, *first-principles* simulations offer a great insight into the processes at function in TiO_2-based systems.[260, 269–274] However, the predictive capacity of DFT, the most commonly utilised methodology in this context, is severely constrained concerning the proper representation of the electronic structure, including the band gap.[100, 119–121] Quantum chemistry techniques,[269] many-body perturbation theory,[100] and dynamic mean-field theory[277, 278] are among the methodologies with higher predictive capability; nonetheless, they are computationally too expensive for practical scenarios to complex titania-based systems. Accordingly, there is a need for a versatile, computationally efficient and accurate methodology to handle the titania electronic properties.

As mentioned in section 3.2, the DFT+U methodology is commonly considered a practical approach for balancing accuracy and computational cost by correcting the on-site Coulomb and exchange energies of specific orbitals. In the last two decades, multiple DFT+U studies have been conducted in which the Hubbard U value was determined to reproduce a particular TiO_2 property known from experiments or high-level theory.[279–291] However, this technique is relatively unsatisfactory. On the one hand, it does not ensure a stable and accurate representation of the characteristics of the material when exposed to varied external circumstances or during chemical reactions. Furthermore, the accurate description of one property does not always ensure the accuracy of the descriptions of other properties. For instance, the optimisation of U_d with respect to the reduction energy of TiO_2 to Ti_2O_3 fails to provide the correct band gap.[279] Similar outcomes were also reported in Ref. [289]. Combining individual Hubbard U correction for the Ti^{3d} and O^{2p} states can improve the description of the atomic structure and the electronic band gap. However, it introduces extra complication and inconsistency, especially concerning the optical response calculation.[283, 284] The accurate electronic band gaps for R- and A-TiO_2 were also presented in 2020 based on Hubbard U and Hund's J correction using the minimum-tracking linear response theory.[290] The extensive benchmarking of DFT+U was recently conducted for several compounds, including R-TiO_2, and it was observed that the predicted band gaps are particularly sensitive to the type of projector functions.[291]

As stated in section 3.3, Hybrid DFT incorporating a fraction of exact-exchange from HF theory is another numerically more involved scheme than Hubbard U correction for addressing the shortcomings of the DFT in describing titania, particularly in predicting single-particle excitation energies.[257, 285, 292–300] The effect of the exact-exchange fraction was examined on the electronic structure of R- and A-TiO_2.[298] Hybrid DFT has also been used to determine optical transitions and Franck-Condon shifts in titania.[300]

4.1.2 Results and Discussion

Parameterisation

To begin with, hybrid functionals using PBE0[222, 223] and HSE[229, 230], containing a fraction α of exact exchange from HF theory, are used to account for XC effects beyond conventional DFT. The adjustable screening parameter ω, controlling the short-ranginess of the interaction in HSE, is chosen equal to 0.106 bohr^{-1}. The exact exchange fraction α has a strong influence on the band gap. As shown in Figure 4.2, it increases nearly linearly with α. The strongest and weakest slope is observed for A- and B-TiO_2, respectively. Fractions α of 11.4% and 16.3% in PBE0 and HSE, respectively, lead to the best simultaneous reproduction of the experimental band gaps of all titania polymorphs studied here.

In particular, the valence band (VB) and conduction band (CB) edges of titania are dominated by O^{2p} and Ti^{3d} states, respectively.[271] Alternatively, a Hubbard U correction can be applied to these

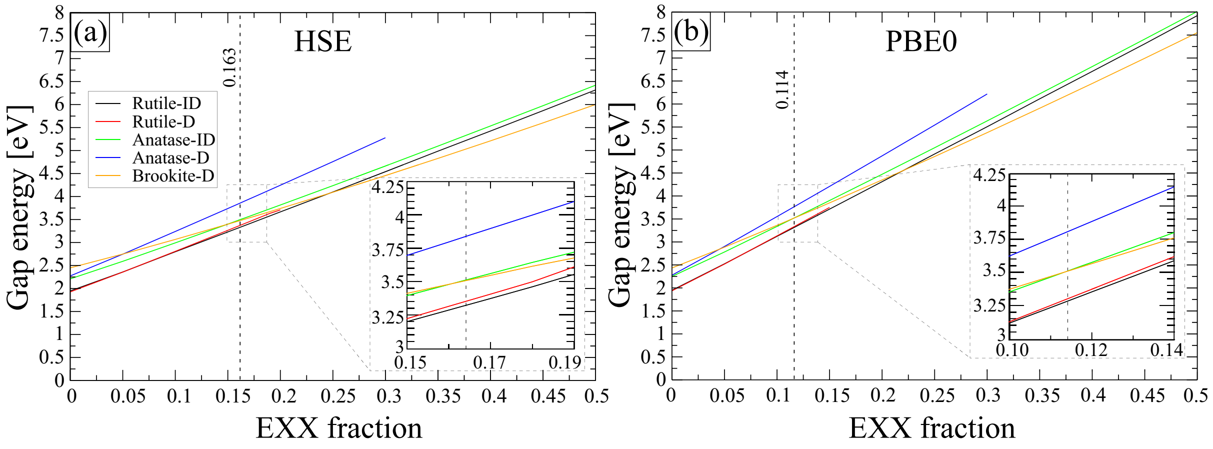

Figure 4.2: Calculated fundamental lowest Direct (D) and Indirect (ID) band gaps for R-, A-, B-TiO_2 as a function of the EXX fraction used in the respective hybrid DFT.

states. In the DFT+U (DFT+U_p+U_d) scheme, U_d parameters represents the screened on-site Coulomb interaction of Ti^{3d} electrons and U_p accounts for the O^{2p} states. Dudarev rotationally invariant Hubbard U/J correction scheme[210], that is, $U_{eff} = U - J$ the effective Hubbard parameter is used in this study. Computational details for this study can be found in Appendix A.1.

In a first step, the U_d values for R-, A-, and B-TiO_2 crystals were found self-consistently using the linear response method.[183] This yields U_d values of 5.91, 5.97 and 5.95 eV for the corresponding Ti^{3d} states. However, while the linear-response theory are applied to determine U_p values for O^{2p} states in TiO_2 crystals, it results in rather large (>18 eV) values that are not suitable for obtaining realistic band structures. Similar results were also obtained in literature[291, 301] and were attributed to the fact that linear-response theory is not suited for application to light elements. Nevertheless, U_d values are not enough alone to reproduce the band gap of titania structures correctly. If U_d is increased for improving band gap of titania structures, the band gap is surprisingly decreasing again after $U_d = 7.5$ eV. The reason of this behaviour is $Ti^{3d} \leftrightarrow O^{2s}$ and $Ti^{3d} \leftrightarrow O^{2p}$ partial hybridisation, see also Partial Density of States (PDOS) in Figure 4.3(c). In addition, U_d alone elongated bond length and lattice parameters, see Table 4.1, Figure 4.3(a), and Figure A.1 in Appendix A.2. Most important, optical spectra is gradually damaged if increasing the U_d value, see Figure A.2 in Appendix A.2.

While considering these facts, two strategies can be used to improve the description fundamental band gap and optical gap.

Method I (Gap correction):

- At first, the U_d values are determined self-consistently using the linear response approach for R-, A- and B-TiO_2 crystals. This results in U_d values of 5.91, 5.97, and 5.95 eV for the respective Ti^{3d} states;

- Next, these U_d values are employed to empirically determine U_p such that the accurate direct band gap is obtained for titania structures. This results in corrections of 4.20 eV for the O^{2p} electrons in R-, A- and B-TiO_2, respectively;

Method II (Optical spectra correction):

- To consider only U_p value by considering lattice parameters obtained in PBE_{sol} because the resulting U_p correction procedure leads to a rigid shift to higher energies. Thereby, U_p value is chosen equal to 8.0 eV to reproduce accurate dielectric optical spectra with comparing experimental and PBE0 optical spectra;

Method I is useful to adjust the band gap to experimental one. It is also sound to produce reasonable lattice parameters because U_d and U_p value work against each other to reproduce reasonable lattice parameters, but it damages optical dielectric spectra. In contrast, Method II is invaluably good for researching the optical dielectric properties of *disordered* structures.

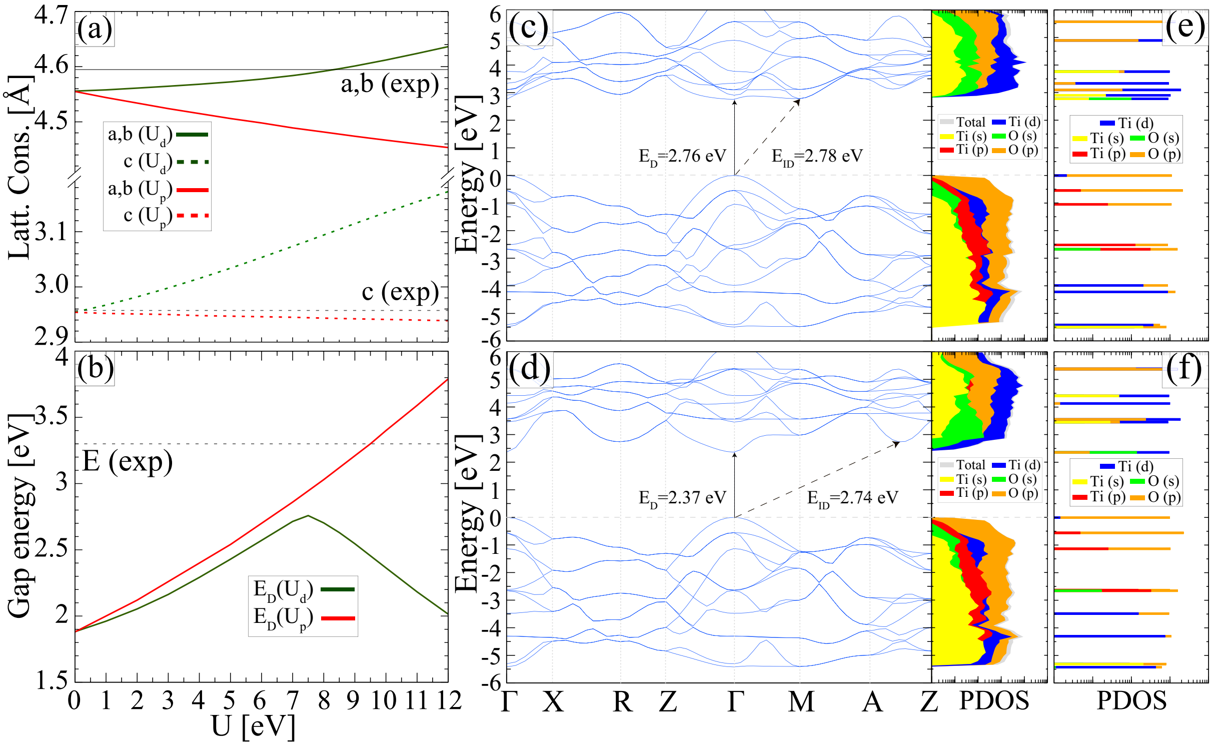

Figure 4.3: Lattice parameters (a) and fundamental band gap (b) of R-TiO_2 crystal calculated as a function U values. Band structure and PDOS with considering U_d=7.5 eV (c) and U_d=10.0 eV (d). For both cases, also the PDOS at the Γ point is given for U_d=7.5 eV (e) and U_d=10.0 eV (f).

TiO_2 bulk crystals

R- and A-TiO_2 belong to the tetragonal space groups $P4_2/mmm$ (136) and $I4_1/amd$ (141), respectively. B-TiO_2 is orthorhombic with space group Pbca (61). TiO_2 octahedra chains are formed in these titania polymorphs consisting of Ti^{4+} cations coordinated to six O^{2-} anions, see Figure 4.1. The R- and A-TiO_2 unit cell contain 6, 12, and 24 atoms, respectively. At ambient conditions, R is the most stable phase while A and B are metastable and transform to R-TiO_2 when heated. However, A- and B-TiO_2 are thermodynamically stable in titania nanoparticles with diameters below 11 nm and in range from 35 to 11 nm, respectively[302].

The lattice parameters of R-, A- and B-TiO_2 are determined within PBE_{sol}, $PBE_{sol}+U_d$, $PBE_{sol}+U_{p,d}$, HSE, and PBE0 are given in Table 4.1. It can be seen that PBE0 provides structural data in excellent agreement with experiment for all three titania polymorphs, while the HSE data are of similar quality as the PBE_{sol} calculations. The $PBE_{sol}+U_d$ calculations lead to a systematic overestimation of the lattice parameters of the order of 1-4 %, which is improved by taking Hubbard corrections for the O^{2p} states into account. Based on the above evaluation, the atomic geometries of PBE0 are considered for band structure and optical response calculations in hybrid functional calculations.

Table 4.2 compares the calculated band gaps for R-, A- and B-TiO_2 with experimental data. As expected, the DFT values underestimate the measured data considerably. A band gap widening by about 0.5-0.8 eV occurs upon inclusion of Hubbard corrections for the Ti^{3d} states. This widening results mainly

Table 4.1: Calculated unit cell parameters **a**, **b**, **c** (in Å) and volume **V** (in Å^3) of R-, A-, and B-TiO$_2$ in comparison to experiment. U$_d$ values are equal to 5.91, 5.97, and 5.95 eV for the respective Ti^{3d} states of R-, A-, and B-TiO$_2$, whereby U$_p$ for the respective O^{2p} states is chosen equal to 4.2 eV. Relative deviations are given with respect to the mean of experimental data.

Method	Rutile			Anatase			Brookite			
	a = b	c	V	a = b	c	V	a	b	c	V
PBE$_{sol}$	4.556	2.954	61.32	3.761	9.579	135.50	9.154	5.424	5.107	253.57
	-0.8%	-0.1%	-1.8%	-0.6%	+0.7%	-0.6%	-0.3%	-0.5%	-0.8%	-1.7%
PBE$_{sol}$+U$_d$	4.578	3.052	63.96	3.834	9.657	141.95	9.240	5.488	5.239	265.67
	-0.4%	+3.2%	+2.5%	+1.3%	+1.5%	+4.1%	+0.6%	+0.7%	+1.7%	+3.0%
PBE$_{sol}$+U$_{d,p}$	4.542	3.038	62.67	3.803	9.653	139.61	9.184	5.448	5.215	260.93
	-1.1%	+2.7%	+0.4%	+0.5%	+1.4%	+2.4%	+0.0%	-0.1%	+1.3%	+1.2%
HSE	4.563	2.953	61.48	3.707	9.949	136.72	9.202	5.418	5.109	254.72
	-0.7%	-0.1%	-1.5%	-2.1%	+4.6%	+0.3%	+0.2%	-0.6%	-0.8%	-1.2%
PBE0	4.573	2.960	61.90	3.738	9.783	136.69	9.175	5.441	5.133	256.25
	-0.5%	+0.1%	-0.8%	-1.2%	+2.8%	+0.3%	-0.1%	-0.2%	-0.3%	-0.6%
Experiments	4.604	2.959	62.72[303]	3.787	9.518	136.50[303]	9.184	5.454	5.146	257.76[303]
	4.587	2.954	62.15[304]	3.784	9.515	136.24[305]	9.180	5.457	5.158	258.39[306]
	4.593	2.959	62.42[307]	3.785	9.514	136.30[307]	9.184	5.447	5.145	257.38[308]

from an upward shift of the conduction band. However, it is not able to reproduce the experimental data. Moreover, an ID band gap rather than a D band gap is calculated for R-TiO$_2$, in contrast to experiment [262, 263]. The correct character of the R-TiO$_2$ band gap is recovered, and excellent band gap values for all three polymorphs are obtained if both the Ti^{3d} and the O^{2p} states are Hubbard U corrected. The band gaps calculated within hybrid DFT agree with the PBE$_{sol}$+U$_{p,d}$ values as well as with experiment within 0.05 eV. Nevertheless, PBE0 predicts an ID band gap semiconductor rather than a D band gap semiconductor for R-TiO$_2$, in contrast to the PBE$_{sol}$+U$_{p,d}$ calculations and the experimental findings, see also Figure 4.4.

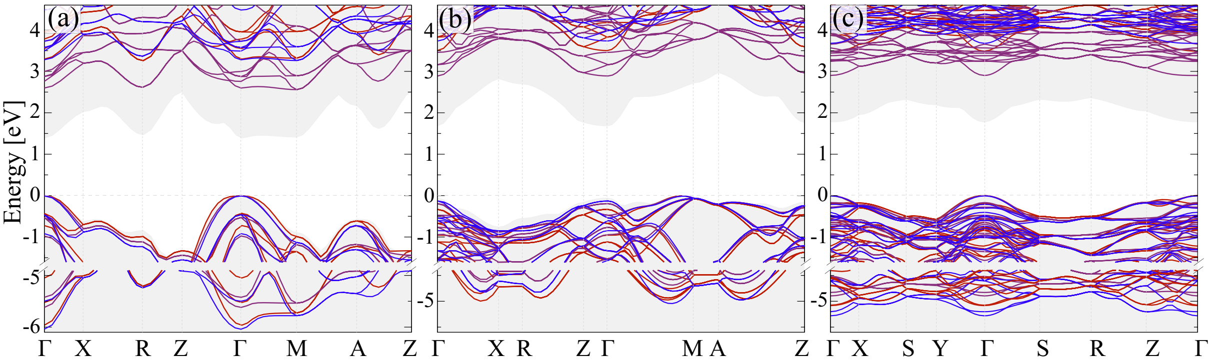

Figure 4.4: Band structures of R-, A-, B- and amorphous thin film TiO$_2$ calculated on the PBE$_{sol}$+U$_d$ (purple), PBE$_{sol}$+U$_{p,d}$ (blue) and PBE0 (red) level of theory. U$_d$ values are equal to 5.91, 5.97, and 5.95 eV for the respective Ti^{3d} states of R-, A-, and B-TiO$_2$ in PBE$_{sol}$+U$_d$ and PBE$_{sol}$+U$_{p,d}$, whereby U$_p$ for the respective O^{2p} states is chosen equal to 4.2 eV.

Also, the electronic states below the VB edge (see band structures in Figure 4.4) are well described using PBE$_{sol}$+U$_{p,d}$ and hybrid DFT. For R titania an upper valence bandwidth in the range of 5-6 eV was measured [309–312]. This is well reproduced by the present PBE$_{sol}$+U$_{p,d}$ calculations, which determine a value of 5.90 eV and the band width of 5.93 eV determined with PBE0. Similarly, PBE$_{sol}$+U$_{p,d}$ predicts a bandwidth of 4.81 eV for the upper valence band in A-TiO$_2$, close to the measured 4.75 eV [313] and the PBE0 prediction of 4.93 eV. Previous HSE and quasiparticle calculations in GW approximation led to bandwidths in excess of 6.5 and 5.5 eV, respectively [257, 271, 289, 314, 315]. For B-TiO$_2$ a bandwidth of 5.05 and 5.09 eV is predicted within PBE$_{sol}$+U$_{p,d}$ and PBE0, respectively. The corresponding experimental data are unknown. PBE$_{\text{sol}}$+U$_{\text{d}}$ calculations result in somewhat smaller band widths than PBE$_{\text{sol}}$+U$_{\text{p,d}}$ or hybrid DFT, with values of 5.42, 4.47, 4.74 eV for R-, A- and B-TiO$_2$, respectively.

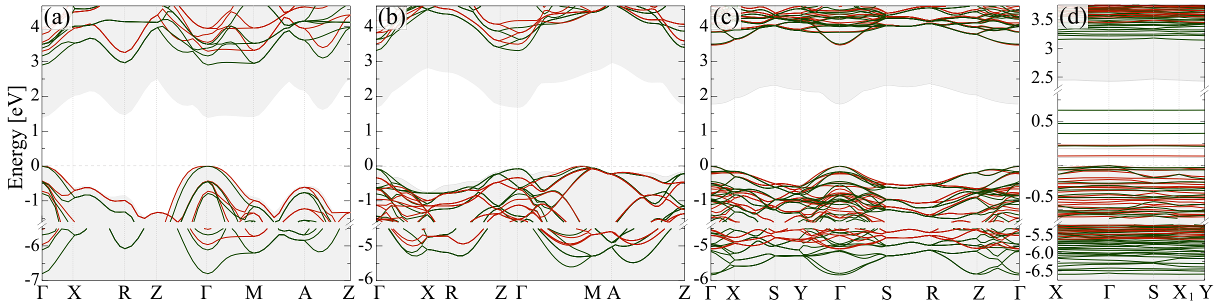

Figure 4.5: Band structures of R-, A-, B- and thin film TiO$_2$ calculated on the PBE$_{\text{sol}}$+U$_{\text{p}}$ (green) and PBE0 (red) level of theory. The PBE$_{\text{sol}}$ band edges are shown as grey shaded areas. U$_{\text{p}}$ is taken equal to 8 eV in order optimize the optical absorption of R- and A-TiO$_2$.

Table 4.2: Calculated D and ID fundamental band gap (in eV) of titania in comparison to experimental data. U$_{\text{d}}$ values are equal to 5.91, 5.97, and 5.95 eV for the respective Ti^{3d} states of R-, A-, and B-TiO$_2$ in PBE$_{\text{sol}}$+U$_{\text{d}}$ and PBE$_{\text{sol}}$+U$_{\text{p,d}}$, whereby U$_{\text{p}}$ for the respective O^{2p} states is chosen equal to 4.2 eV. In PBE$_{\text{sol}}$+U$_{\text{p}}$, U$_{\text{p}}$ value is equal to 8.0 eV so that the calculated optical absorption spectra reproduce the experimental ones.

Method	Rutile	Anatase	Brookite	Amorphous thin-film
PBE$_{\text{sol}}$	1.88 (D) 1.93 (ID)	2.27 (D) 2.16 (ID)	2.40 (D)	2.43 (D)
PBE$_{\text{sol}}$+U$_{\text{d}}$	2.60 (D) 2.55 (ID)	3.08 (D) 2.91 (ID)	2.90 (D)	2.98 (D)
PBE$_{\text{sol}}$+U$_{\text{d,p}}$	3.29 (D) 3.29 (ID)	3.87 (D) 3.76 (ID)	3.69 (D)	3.37 (D)
PBE$_{\text{sol}}$+U$_{\text{p}}$	2.91 (D) 2.95 (ID)	3.39 (D) 3.32 (ID)	3.50 (D)	3.15 (D)
HSE	3.34 (D) 3.31 (ID)	3.84 (D) 3.52 (ID)	3.50 (D)	3.43 (D)
PBE0	3.31 (D) 3.29 (ID)	3.83 (D) 3.51 (ID)	3.49 (D)	3.43 (D)
Experiment	3.30 (D) — [259]	3.97 (D) 3.47 (ID)[260]	—	—

While following Method II, that is, considering U$_{\text{p}}$ alone to fit optical dielectric spectroscopy in DFT+U calculations, it also improve significantly (of course, not as much as the PBE$_{\text{sol}}$+U$_{\text{p,d}}$ and PBE0) the band gap of titania structures with comparing PBE$_{\text{sol}}$ and PBE$_{\text{sol}}$+U$_{\text{d}}$, see Table 4.2. Surprisingly, the bandgap of B-TiO$_2$ are found almost same (3.50 eV) with the corresponding value obtained by PBE0. The most significant difference is found in the remaining range of -7.0 to -4.5 eV, where the PBE$_{\text{sol}}$+U$_{\text{p}}$ bands are over downshifted with respect to the PBE0 results, see Figure 4.5.

In Figure 4.6 the calculated imaginary parts of the dielectric functions of R-, A- and B-TiO$_2$ in ordinary and extraordinary polarisation are compared with experiment. The calculations based on the PBE$_{\text{sol}}$+U$_{\text{p}}$ and PBE0 electronic structure account well for the onset energy of the optical absorption caused by O^{2p}→Ti^{3d} t$_{2g}$ inter-band transitions. Among the electronic structure methods probed here, PBE0 provides the best description of the line shape of the dielectric function, at least for low photon energies. PBE$_{\text{sol}}$+U$_{\text{p}}$ resembles shitted PBE$_{\text{sol}}$ results. Interestingly, even some small peaks for E$\perp$c and E$\|$c are found in agreement with the PBE0 hybrid as well as with experiment. Furthermore, the calculated line shape for photon energies between 9-12 eV fits nicely to measured optical spectra in A-TiO$_2$.

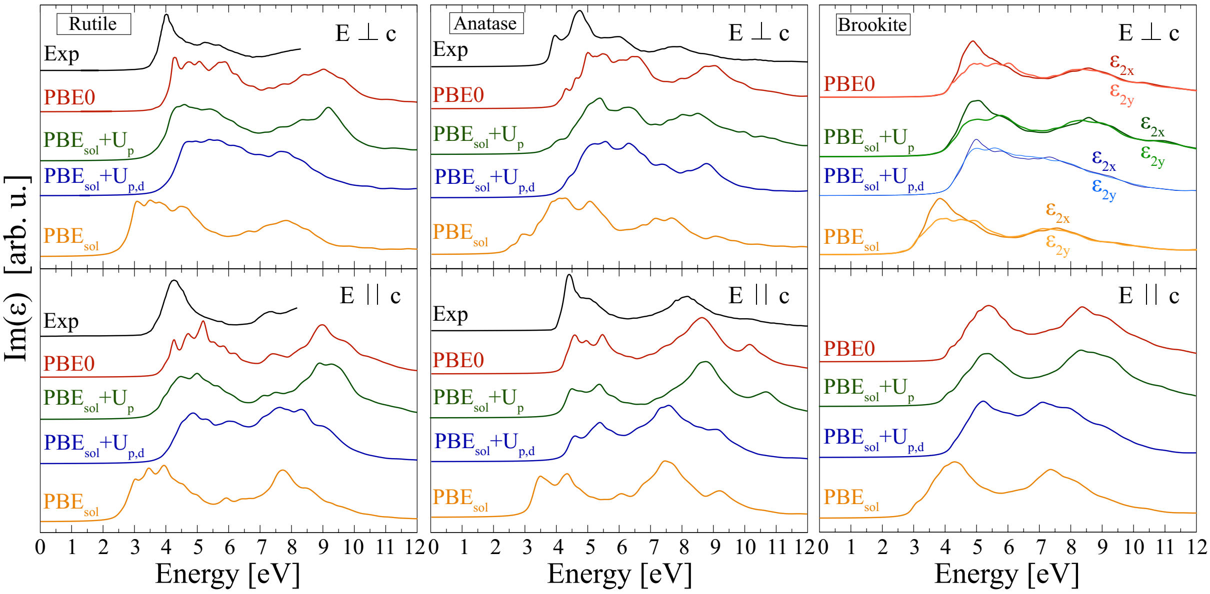

Figure 4.6: Imaginary part of the titania complex dielectric function calculated within IPA based on the PBE_{sol}, PBE_{sol}+U_p (U_p=8 eV), PBE_{sol}+$U_{d,p}$ (U_d=5.94 eV, U_p=4.2 eV) with PBE_{sol} electronic structure in comparison to experimental data from Ref. [316] for R-TiO_2 and Ref. [317] for A-TiO_2.

Amorphous TiO_2 thin film

R-, A- and B-TiO_2 are well-defined by their octahedral building blocks, but the disorder-induced creation of under and over-coordinated Ti atoms characterise the amorphous phase, which is defined by the truncation of Ti-O octahedral coordination, see Figure 4.7(a). The exceptional optical and catalytic capabilities of the crystalline phases have also sparked interest in amorphous TiO_2 as a low-cost material for technological applications.[318, 319] Furthermore, in the hydrothermal treatment[b] of different single-crystalline phases, amorphous titania serves as a generic forerunner material.[320–323] Thereby, amorphous titania thin film can be easily prepared by using various experimental techniques.[323–330]

The general geometric characteristics of the proposed amorphous titania thin film model, the Ti-O bond length is changed around 1.83-2.13 Å. TiO_6-polyhedron building blocks occur with an even higher fraction of 60%, while fourfold, fivefold and sevenfold coordinated units occur with a ratio of 4%, 29% and 7%, respectively. The thickness of thin film is around 1.1 nm. Our model is a reasonable match to the experimental synthesised “glassy” ultra-thin film (∼2 nm) amorphous TiO_2 concerning TiO_6-polyhedron building blocks ratio.[330]

The band gap of amorphous TiO_2 is found to close in the B-TiO_2 phases. The almost flat middle gap states are caused by a few under-coordinated surface oxygens. Despite the mid-gap states, energy dispersive bands have been observed along the high-symmetry lines in the BZ, see Figure 4.5(d). It means that the loss of momentum conservation does not induce a HOMO-LUMO-type energy gap in the *disordered* amorphous titania thin film. The optical anisotropy has been observed in the amorphous titania ultra-thin film, its complex dielectric function acts as almost similar behaviour the biaxial B phase, see Figures 4.6(c) and 4.7(b). Based of the electronic band gaps and optical spectra, it can be concluded that there is a close relation between B and the amorphous titania, and this observation confirms the significant results about the considerable resemblance of the atomic arrangement in amorphous samples with crystalline B-TiO_2.[264, 331]. Furthermore, the valley characteristic between main two peak disappear in PBE_{sol}+$U_{p,d}$ and it keeps similarity only up to 7 eV with comparing PBE0 result. However, PBE_{sol}+U_p and PBE0 results coincide completly. Even the small peak for E⊥c and E||c at around 8.0 eV is found

---

[b] It provides an effective reaction environment for the synthesis of nanocrystalline TiO_2 with high purity

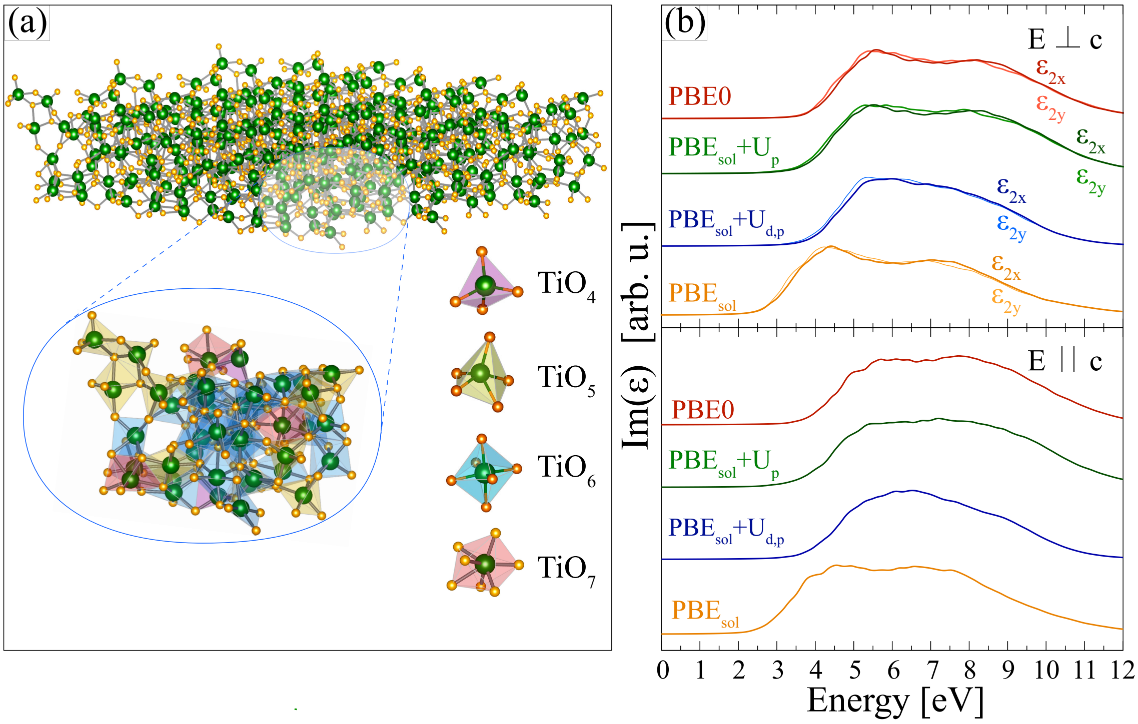

Figure 4.7: (a) Polyhedra representation (2.5 Å Ti-O bond-length cutoff) of the TiO_x building blocks for the 126-atoms of amorphous TiO_2 thin film, TiO_x building block fraction is TiO_4 (4%), TiO_5 (29%), TiO_6 (60%) and TiO_7 (7%). The thickness of thin film is around 1.1 nm. (b) imaginary part of the titania complex dielectric function calculated within IPA based on the PBE_{sol}, $PBE_{sol}+U_p$ (U_p=8 eV), $PBE_{sol}+U_{d,p}$ (U_d=5.94 eV, U_p=4.2 eV) based on PBE_{sol} relaxed crystal structure in comparison to PBE0 hybrid calculation. Notably, the surface states visible in the band structure (see Figure 4.5(d)) do not show up in the calculated optical absorption spectra.

in agreement with the PBE0 hybrid. In addition, the optical properties of the amorphous titania thin film is not affected by surface defects states, that is, the mid gap states are not observed in optical spectra. Considering all the aforementioned findings, PBE0 is the gold standard for investigating geometrical structures, electronic properties and optical spectra. However, Method II also describes optical spectra very well for large *disordered* systems at a more efficient computational cost.

4.2 Titania-Graphene Composite Systems[c]

In general, TiO_2-based photocatalytic systems were extensively employed in the wastewater treatment of dyes,[332, 333] microbial disinfection,[334, 335] pharmaceuticals,[335, 336] and hormones[337]. However, two undesired features of the TiO_2, that is, its lack of response to visible light and fast recombination rate of electron-hole pairs, hinder its wide range of applications.[249, 338] Coupling TiO_2 with Graphene (GR)[d] is very promising to surmount these limitations for energy and environmental applications.

4.2.1 Overview

Several techniques, including surface dye sensitisation,[343] precious metal deposition,[344, 345] particle doping,[346, 347] surface modification,[348–350] and particle size modification,[350, 351] have been investigated to improve the properties of TiO_2 material for high-efficiency solar energy in photocatalytic applications. Even though all of these techniques can extend the wavelength of photoactivation of TiO_2 into the visible region of the electromagnetic spectrum, the surface and particle size modification is more promising for mitigating several undesirable side effects in practical applications.[352–354] In recent years, an accessible pathway for enhancing the photocatalytic activities of TiO_2 materials is to combine it with several allotropes of carbon materials since they are more likely to behave as an effective electron donor[355–360] or acceptor[361] to promote the photoinduced charge carriers and mitigate the recombination of the photogenerated electron-holes.

Thanks to the high organic pollutant adsorption capability, GR has been used as an electrocatalyst and promoter in photocatalysis.[362, 363] In addition, GR-metal(oxide) composites have great potential for various applications, including photocatalysis, photovoltaic devices, batteries, supercapacitors, bioimaging, and sensors, owing to the excellent electrical and electronic properties and the synergistic effect between GR and metal(oxide) nanoparticles.[364–368] Indeed, GR appears as a suitable candidate to be combined with TiO_2 to mitigate electron-hole recombination by taking advantage of the higher mobility of charge transferred into the GR sheet.[362, 363] The presence of GR can also function as a sensitiser by extending photoabsorption into the visible region. In addition, new reaction sites can boost overall reactivity. The π-d electron coupling can be instrumental for the fast transport of the photoinduced electron between GR and TiO_2, effectively inhibiting the recombination of photogenerated electron-hole pairs in TiO_2.[369]

Nanosized TiO_2 has a higher surface-to-volume ratio than bulk titania; that is, TiO_2 clusters contain a high density of active surface sites for adsorption and catalysis. Furthermore, TiO_2 clusters allow the photogenerated charges to reach the catalyst surface, reducing the undesired recombination rate of electron-hole pairs. Several theoretical and experimental studies have been conducted on neutral TiO_2 clusters[370–378] and their combination with GR-based materials[379–385]. Some of the interesting results can be mentioned as the following examples:

- the charge separation of the VB maximum and CB minimum by location at the cluster and GR sheet reduces the probability of electron-hole recombination, and the excitation energy decreases in the visible light region for the VB maximum contributed from C^{2p} is considerably less than for Ti^{2p}[380];

- C vacancies in GR or epoxide groups are proposed as the optimal anchor points for TiO_2 on a potential energy surface that is otherwise fairly shallow[381];

---

[c] The results presented in this section were published in Journal of Computational Chemistry, see Ref. [105].

[d] As a two-dimensional allotrope of carbon, GR possesses a certain set of unique properties, including superior electron mobility, high thermal conductivity, flexible structure, large specific surface area, high transparency, outstanding optical properties and quantum hall effects at room temperature.[339–342]

- the carbon support to TiO_2 clusters has a considerable effect on the CO_2 binding energy[382];
- the Graphene Quantum Dot (GQD)/TiO_2 combination has five times the photocatalytic performance of the highly effective $CaInO_4$ photocatalyst[383];
- GR flake and TiO_2 nanoparticle composites degrade as much as 70% more atmospheric NO_x than the titania photocatalyst[384];
- GR oxide quantum dot increases the photocatalytic activity of TiO_2 by facilitating the separation of photogenerated electron-hole pairs[385];

4.2.2 Results and Discussion

Here, it is focused on rationalising the photocatalytic properties of TiO_2/GR composite materials. To this end, vdW-corrected DFT is used to determine the ground-state atomic structures of bare as well as GR and GQD adsorbed $(TiO_2)_n$ clusters (n=1-5). The electronic excitation properties of the respective systems are studied using KS-DFT, screening hybrid, and CDFT.

Titania Clusters

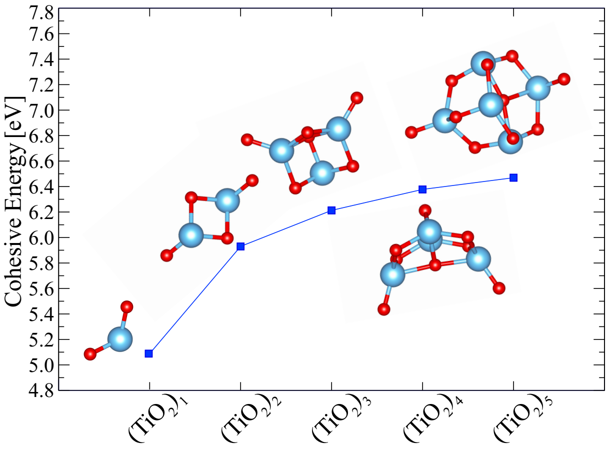

Figure 4.8: Calculated cohesive energy per atom in dependence on the titania cluster size. The insets show the geometric structure of the energetically most favourable neutral TiO_2 clusters. Blue and red spheres represent Ti and O atoms, respectively. The solid line is to guide the eye.

The calculation started with a systematic search for the neutral titanium dioxide clusters with one, two, three, four, and five units of TiO_2. Computational details with related this study can be found in Appendix B.1. The $(TiO_2)_n$ structures with n=1-5 (see Figure 4.8) are optimised by calculating their total energy without imposing any symmetry constraint, and they are in good agreement with those obtained previously by experiment and theory.[377, 378] The minimum energy structures of $(TiO_2)_1$, $(TiO_2)_2$, $(TiO_2)_3$, $(TiO_2)_4$, and $(TiO_2)_5$ clusters contain C_{2v}, C_{2h}, C_s, C_{2v}, and C_s point group symmetry, respectively. The cohesive energy per atom increases by increasing the unit size of TiO_2; see Table 4.3 and Figure 4.8. Accordingly, bigger TiO_2 clusters are more energetically stable than smaller clusters. The Bader charge analysis indicates that the Ti atom donates 0.7-1.0 e^- to each bonding O atom; that is, the TiO_2 clusters possess ionic bonds. All ground state structures of TiO_2 clusters are found to be non-magnetic.

As seen in Table 4.3, the adiabatic EA and IE are in fair agreement with the experimentally reported data.[371–374] In this case, it has to be mentioned that isomers with the highest EA rather than those with the lowest energy may be selectively observed in photoemission experiments.[376] The calculated HOMO-LUMO energy gaps for the different clusters depend strongly on the level of theory: GGA, HSE06, and ΔSCF predict values between 1.6-2.88, 3.06-4.27, and 6.7-8.07 eV, respectively. As expected (see sections 2.5.2 and 3.1), DFT-GGA gives the lowest values because it neglects the electron self-energy. The gap gets bigger when the exact-exchange is only partially used in the screening hybrid functional HSE06. Even larger values, consistent with the order of magnitude expected from the measured IEs and EAs, are obtained from the ΔSCF calculations. The latter method accounts for electronic MB effects and may thus yield the most accurate results, see Section 2.6. As one might expect from the quantum confinement effect, neither of the computational methods used here shows that the HOMO-LUMO energy gap decreases steadily as the size of the cluster increases.[386] This might be because the clusters studied here are small, so surface and symmetry effects can significantly the excitation energies.

At pH = 0, the oxidation potential of O_2/H_2O and the reduction potential of H^+/H_2 are equal to -4.44 eV and -5.67 eV (0 V and 1.229 V on the electrochemical scale), respectively.[387] As illustrated in Figure 4.9, the respective values are well within the HOMO-LUMO energy gap obtained within ΔSCF; that is, the energies of photogenerated holes (electrons) of TiO_2 clusters are lower (higher) than the electrochemical potential of the O_2/H_2O (H^+/H_2) redox couple. Hence, TiO_2 clusters in principle contain a suitable electronic structure for the overall solar water splitting. Furthermore, the charge density separation of HOMO and LUMO energy levels by location at the corner and centre of titania clusters mitigates the probability of electron-hole recombination, see Figure A.3 in Appendix B.2. The optical gaps of TiO_2 clusters differ from 2.09 to 2.86 eV, which is smaller than the optical gaps of R-TiO_2 (~3.0 eV)[262–265] and R-TiO_2 (~3.4 eV)[264–266] bulk phases. Accordingly, they are more responsive to visible light. As shown in Table 4.3, the optical gaps of the TiO_2 clusters are pretty close to the DFT-GGA's HOMO-LUMO energy gaps, indicating the almost cancellation of the quasiparticle gap opening and the Coulomb attraction of electrons and holes. The large exciton binding energies of titania clusters exhibit that the small clusters have a strong electrostatic electron-hole pair interaction, so there is a significant quantum confinement effect in TiO_2 clusters. Furthermore, the large Stokes shift exhibits that there is strong exciton-phonon coupling and excellent photostability, increasing with cluster size.

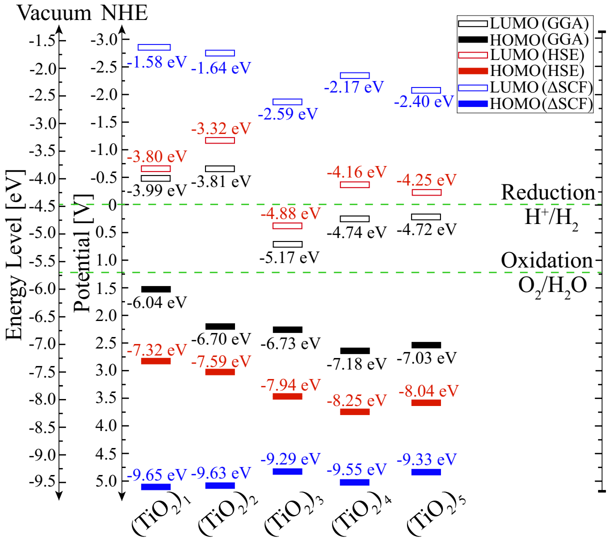

Figure 4.9: Calculated the HOMO and LUMO energies level of titania clusters in relation to the redox reactions of water splitting.

Table 4.3: The calculated parameters for neutral TiO_2 clusters. The cohesive energy per atom, E_{Coh}; the charge donation from Ti to O, $\Delta\rho_{Ti\text{-}O}$; the vertical and adiabatic EA, EA_v and EA_{ad}; the vertical and adiabatic IE, IE_v and IE_{ad}; experimental EA and IE, EA^{exp}_{ad} and IE^{exp}_{ad}; E^{GGA}_{HL}, E^{HSE}_{HL} and $E^{\Delta SCF}_{HL}$ are HOMO-LUMO energy gaps based on GGA, HSE06 and ΔSCF, respectively; $E^{\Delta SCF}_{Op}$ is optical gap based on ΔSCF; the Stokes shift, Δ_{ST}; the exciton binding energy, E^{ex}_{b}. Numbers in parentheses represent estimated experimental uncertainties in the last digits.

	E_{Coh}(eV)	$\Delta\rho_{Ti\text{-}O}$(e^-)	EA_v(eV)	EA_{ad}(eV)	EA^{exp}_{ad}(eV)	IE_v(eV)	IE_{ad}(eV)	IE^{exp}_{ad}(eV)	E^{GGA}_{HL}(eV)	E^{HSE}_{HL}(eV)	$E^{\Delta SCF}_{HL}$(eV)	$E^{\Delta SCF}_{Op}$(eV)	Δ_{ST}(eV)	E^{ex}_{b}(eV)
$(TiO_2)_1$	5.09	0.8	1.58	1.61	1.59(3)[b,c]	9.65	9.50	9.5(1)[d]	2.05	3.52	8.07	2.09	0.51	5.98
$(TiO_2)_2$	5.92	0.8-0.9	1.64	1.83	2.10(8)[b], 2.06(5)[c]	9.63	9.42	10.0(5)[e]	2.89	4.27	7.99	2.86	1.24	5.13
$(TiO_2)_3$	6.21	0.7-0.8	2.59	2.89	2.9(1)[b], 2.78(10)[c]	9.29	9.17	—	1.55	3.06	6.70	2.45	1.27	4.25
$(TiO_2)_4$	6.37	0.7-1.0	2.17	2.85	3.3(2)[b], 3.00(15)[c]	9.55	9.40	—	2.44	4.09	7.38	2.85	1.66	4.53
$(TiO_2)_5$	6.46	0.8-1.0	2.40	2.85	3.15(20)[c]	9.33	9.08	—	2.31	3.79	6.93	2.86	1.68	4.07

[b] See Tab. 3 of Ref. [371]. [c] See the value of Adiabatic Detachment Energies of anions TiO_2^- clusters in Tab. 1 of Ref. [372], which represents Adiabatic EA of neutral TiO_2 clusters. [d] See Ref. [373]. [e] See Ref. [374].

TiO_2 clusters on Graphene

In this part, the interaction between TiO_2 clusters and pristine GR is examined. Up to one hundred start configurations were utilised to identify the optimal bonding geometry, depending on cluster size and symmetry. In any case, it is observed that the TiO_2 clusters bind preferentially with Ti to the GR surface.

The adsorbate TiO_2 clusters have a negligible effect on the structure of the GR. Figure 4.10 illustrates the most favourable adsorption configurations. They are mostly compatible with reported results,[380–382] and the remaining differences can be related to the neglect of vdW forces or limitations concerning the number of starting configurations in previous works.

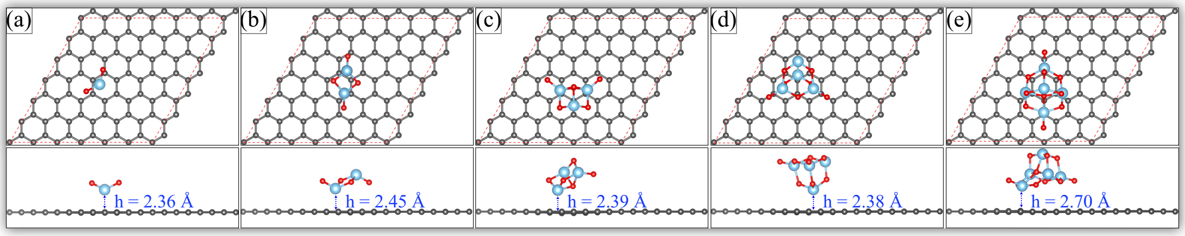

Figure 4.10: Top and side views of the energetically most favourable $(TiO_2)_n$/GR configurations within the (6 × 6) supercell for (a) n=1, (b) n=2, (c) n=3, (d) n=4, and (e) n=5. Blue, red and dark grey spheres represent Ti, O, and C atoms, respectively. The dashed line represents the hexagonal unit cell.

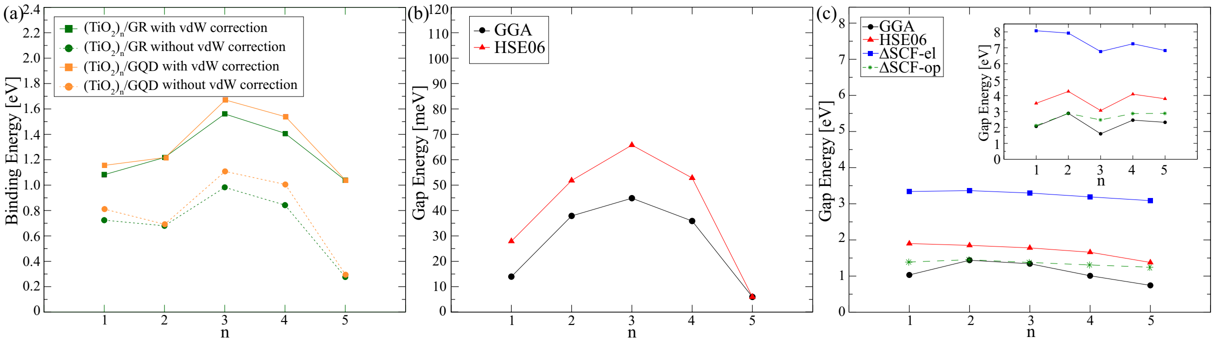

Figure 4.11: (a) Calculated bonding energy of GR and GQD adsorbed $(TiO_2)_n$ clusters. (b) Band gap of GR adsorbed $(TiO_2)_n$ clusters. (c) HOMO-LUMO energy gap and the optical gap of GQD adsorbed $(TiO_2)_n$ clusters. The inset shows the HOMO-LUMO energy gap and optical gap of the isolated titania clusters for comparison. The solid lines are to guide the eye.

Table 4.4: The calculated parameters for TiO_2 clusters on GR. The GR-TiO_2 cluster distance, h; the binding energy with and without vdW correction, $E_b^{\text{w-vdW}}$ and $E_b^{\text{wo-vdW}}$; the charge transfer from GR to TiO_2 clusters, $\Delta\rho_{GR-TiO_2}$; E_g^{GGA} and E_g^{HSE} are band gaps based on GGA and HSE06, respectively.

	h(Å)	$E_b^{\text{w-vdW}}$(eV)	$E_b^{\text{wo-vdW}}$(eV)	$\Delta\rho_{GR-TiO_2}$(e^-)	E_g^{GGA}(eV)	E_g^{HSE}(eV)
$(TiO_2)_1$/GR	2.36	1.08	0.72	0.1	14	28
$(TiO_2)_2$/GR	2.45	1.22	0.68	0.1	38	52
$(TiO_2)_3$/GR	2.39	1.56	0.98	0.2	45	66
$(TiO_2)_4$/GR	2.38	1.41	0.83	0.2	36	53
$(TiO_2)_5$/GR	2.70	1.04	0.27	0.1	6	6

The vertical distance of the closest atoms between TiO_2 clusters and GR ranges from 2.37 to 2.68 Å; see Figure 4.10 and Table 4.4. During adsorption, an electron transfer of the order of 0.1-0.2 e^- occurs from GR to the TiO_2 clusters. Accordingly, the construction of internal electric fields at the interface can improve the photoactivity of TiO_2 clusters by boosting the electron transfer rate and providing more reaction-active sites for the degradation of environmental contaminants.[388–391] Still, there is only little charge overlap between the GR π electrons and the adsorbate, see Figure A.4 in Appendix B.2. This reveals a substantial contribution of vdW forces to the bonding of pristine GR and TiO_2 clusters, see Figure 4.11(a).

At the Fermi level, the perturbation caused by the adsorption of TiO_2 clusters splits the GR linear bonding and anti-bonding π bands (Dirac cone)[e]; see Figure A.5 in Appendix B.2. Breaking the inversion symmetry in the carbon lattice opens a small band gap, see Figure 4.11(b) and Table 4.4. However, a word of caution is warranted regarding the calculated values: the computations were conducted using periodic boundary conditions specifying a (6×6) GR unit cell. The band gap's opening will not only depend on cluster size but will also increase when the unit cell size decreases in response to increased cluster coverage.

The PDOS of $(TiO_2)_n$/GR, depicted in Figure 4.12, indicates that both VB and CB states mainly originate from the GR carbon atoms and that the characteristic V shape of the GR PDOS at the Dirac point is almost conserved except for the small band gap opening. However, a significant contribution of $(TiO_2)_n$ clusters displays that the total DOS increases with cluster size for the CB and decreases with cluster size for the VB. There is a partial hybridisation between GR and $(TiO_2)_n$ VB and CB states, as seen in the band decomposed charge density, see Figure A.5 in Appendix B.2.

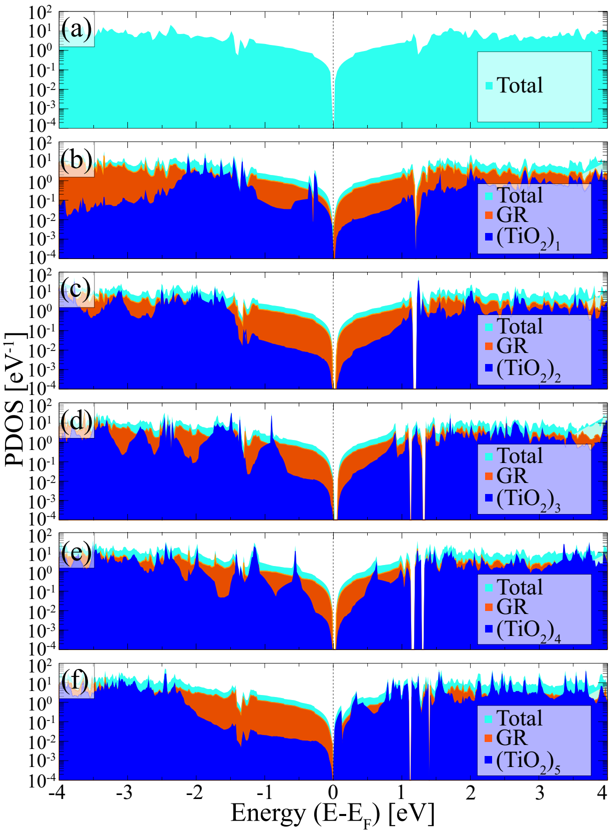

Figure 4.12: The total Density of States (DOS) and PDOS for compatible with the total energy results, the absorbed $(TiO_2)_n$ cluster (a) n=0, (b) n=1, (c) n=2, (d) n=3, (e) n=4, and (f) n=5 with the GR. Note the (decimal) logarithmic scale.

Combination of TiO_2 clusters and Graphene Quantum Dot

In this part, the interaction of TiO_2 clusters with GQDs[f] is explored. The electronic property of GR is varied from semimetal to semiconductor and depends on the flake size and form due to the quantum confinement.[393] The stable structure of GQD depends on their shape, size, and temperature. The armchair-edged hexagonal GQDs are thermodynamically more stable than other GQD shapes.[394] By chemically exfoliating graphite nanoparticles, hexagonal GQDs with a diameter range of 1.65-21 nm (2.1-317.3 nm^2 surface area) have been produced.[395] Based on mentioned information, the armchair-edged hexagonal GQD is chosen as a model system. The quantum dot edges in our model have been passivated with hydrogen to saturate the dangling bonds since GQDs produced from bottom-up synthesis[396] are typically hydrogen passivated.

Initially, bare and $(TiO_2)_1$-decorated GQD of varying sizes (~ 1-13 nm^2) were investigated concerning equilibrium geometry, total energy, and band gap; see Figure A.6 in Appendix B.2. The experimentally reported HOMO-LUMO band edges (~ -3.3 – -5.7 eV vs Vacuum) and band gap (~ 2.4 eV) for the coil GQD (~ 60 carbon rings)[397] are, respectively, in good agreement with the current obtained ΔSCF values (-2.63 – -5.29 eV vs Vacuum) and (2.66 eV) for $C_{222}H_{42}$ GQD (91 carbon rings). Additionally,

---

[e] The VB and CB take the form of the upper and lower halves of a conical surface.

[f] GQD refers to the fragmentation of a GR monolayer into small pieces (disks) having dimensions of a few nanometers (2-20 nm).[392]

for the exactly same $C_{114}H_{30}$ GQD, the theoretically predicted electronic band gap (3.51 eV) and exciton binding energy (1.37 eV) based on the GW+BSE method[398] are in reasonable agreement with the currently obtained ΔSCF values (3.83 eV) and (1.99 eV), respectively. It can be asserted with certainty that both the HOMO-LUMO energy gap and the optical gap of the GQDs are highly proportional to their size, and they decrease steadily as GQD's size grows. The optical gaps of bare and $(TiO_2)_1$-decorated GQD bigger than about 3 nm^2 are energetically below the visible light's spectral range; see Table 4.5 and Figure A.6 in Appendix B.2.

Table 4.5: The calculated parameters for GQDs and $(TiO_2)_1$ cluster on the surface of GQDs. ^{a} The cohesive energy per atom, E_{Coh}; the binding energy of $(TiO_2)_1$ cluster to GQDs, E_b; E_{HL}^{GGA}, E_{HL}^{HSE} and $E_{HL}^{\Delta SCF}$ are HOMO-LUMO energy gaps based on GGA, HSE06 and ΔSCF, respectively; the vertical electronic affinity and ionisation energy, EA_v and IE_v ;the adiabatic EA and IE, EA_{ad} and IE_{ad} ; $E_{Op}^{\Delta SCF}$ is optical gap based on ΔSCF; the Stokes shift, Δ_{ST}; the exciton binding energy, E_b^{ex}.

	E_{Coh}(eV)	E_b(eV)	E_{HL}^{GGA}(eV)	E_{HL}^{HSE}(eV)	$E_{HL}^{\Delta SCF}$(eV)	EA_v(eV)	EA_{ad}(eV)	IE_v(eV)	IE_{ad}(eV)	$E_{Op}^{\Delta SCF}$(eV)	Δ_{ST}(eV)	E_b^{ex}(eV)
$C_{42}H_{18}$	6.27	-	2.46	3.12	5.28	1.23	1.26	6.51	6.50	2.44	0.26	2.84
$C_{114}H_{30}$	6.77	-	1.53	1.95	3.51	2.15	2.20	5.66	5.63	1.52	0.11	1.99
$C_{222}H_{42}$	7.03	-	1.10	1.40	2.66	2.63	2.69	5.29	5.22	1.10	0.06	1.56
$C_{480}H_{60}$	7.39	-	0.76	0.95	1.92	3.04	3.11	4.96	4.88	0.76	0.02	1.16
$(TiO_2)_1/C_{42}H_{18}$	-	1.18	1.31	2.53	4.88	1.75	1.86	6.63	6.54	1.87	0.65	3.01
$(TiO_2)_1/C_{114}H_{30}$	-	1.15	1.03	1.90	3.43	2.38	2.43	5.81	5.75	1.41	0.16	2.02
$(TiO_2)_1/C_{222}H_{42}$	-	1.13	0.90	1.38	2.62	2.75	2.81	5.37	5.31	1.06	0.05	1.46
$(TiO_2)_1/C_{480}H_{60}$	-	1.12	0.72	0.94	1.82	3.14	3.18	4.96	4.90	0.75	0.02	1.07

Therefore, the following is focused on a GQD with a surface area of 3.18 nm^2 containing 114 carbon and 30 hydrogen atoms. This type of GQD is employed to investigate the adsorption of $(TiO_2)_n$ clusters. Various feasible initial configurations have been used to arrive at the models depicted in Figure 4.13, representing the optimal geometry for each cluster size. TiO_2 clusters bound to the GQD similarly to pristine GR. This also keeps the structural characteristics, such as the vertical distance between titania clusters and pristine GR, see Figure 4.13 and Table 4.6.

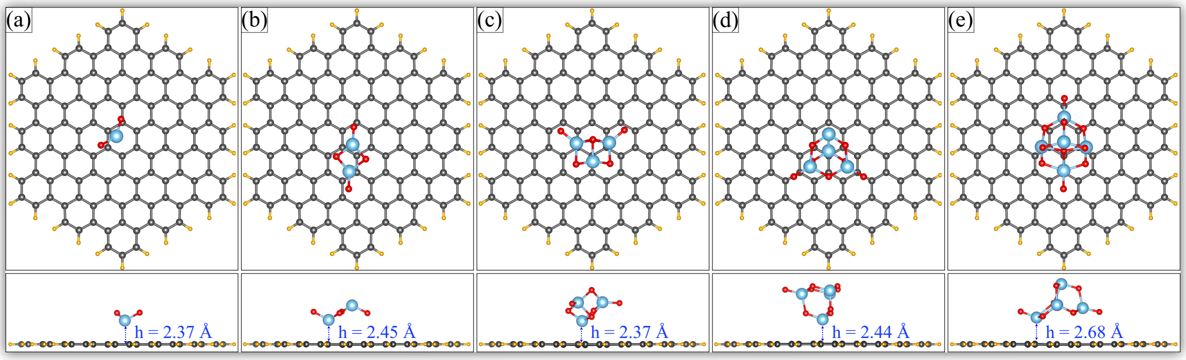

Figure 4.13: Top and side views of the energetically most favourable $(TiO_2)_n$/GQD configurations for (a) n=1, (b) n=2, (c) n=3, (d) n=4, and (e) n=5. Blue, red, dark grey, and orange spheres represent Ti, O, C, and H atoms, respectively.

The TiO_2 clusters are slightly stronger bind to the GQD than to GR. The vdW forces account for a significant fraction of the cluster GQD interaction again, as seen in Figure 4.11(a). The Bader charge analysis reveals the charge transfer from the GQD to the titania clusters of approximately 0.1-0.2 e$^-$, which is similar to the absorption of titanium clusters on pristine GR, see Table 4.6. Similarly, there is a small charge density overlap at the interface; see Figure A.7 in Appendix B.2.

The GQD⇝TiO_2 charge transfer upon bonding can be comprehended from their distinct IEs, see Figure A.8 in Appendix B.2. When titania clusters and GQDs are combined, their respective Fermi levels are aligned, the charge is transferred across the interface, and an electric field builds up. The relative

Table 4.6: The calculated parameters for TiO_2 clusters on GQD. The GQD-TiO_2 cluster distance, h; the binding energy with and without vdW correction, $E_b^{\text{w-vdW}}$ and $E_b^{\text{wo-vdW}}$; the charge transfer from GQD to clusters; $\Delta\rho_{GQD-TiO_2}$; E_{HL}^{GGA}, E_{HL}^{HSE} and $E_{HL}^{\Delta SCF}$ are HOMO-LUMO energy gaps based on GGA, HSE06 and ΔSCF, respectively; the adiabatic EA and IE, EA_{ad} and IE_{ad}; $E_{Op}^{\Delta SCF}$ is optical gap based on ΔSCF; the Stokes shift, Δ_{ST}; the exciton binding energy, E_b^{ex}.

	h(Å)	$E_b^{\text{w-vdW}}$(eV)	$E_b^{\text{wo-vdW}}$(eV)	$\Delta\rho_{GQD-TiO_2}$(e⁻)	E_{HL}^{GGA}(eV)	E_{HL}^{HSE}(eV)	$E_{HL}^{\Delta SCF}$(eV)	EA_v(eV)	EA_{ad}(eV)	IE_v(eV)	IE_{ad}(eV)	$E_{Op}^{\Delta SCF}$(eV)	Δ_{ST}(eV)	E_b^{ex}(eV)
$(TiO_2)_1$/GQD	2.37	1.15	0.81	0.2	1.03	1.90	3.43	2.38	2.43	5.81	5.75	1.41	0.16	2.02
$(TiO_2)_2$/GQD	2.45	1.22	0.69	0.1	1.44	1.85	3.47	2.25	2.33	5.72	5.68	1.46	0.09	2.01
$(TiO_2)_3$/GQD	2.37	1.67	1.11	0.2	1.37	1.78	3.38	2.54	2.60	5.92	5.86	1.40	0.05	1.98
$(TiO_2)_4$/GQD	2.44	1.53	1.00	0.2	1.05	1.66	3.28	2.68	2.74	5.96	5.91	1.38	0.30	1.90
$(TiO_2)_5$/GQD	2.68	1.03	0.29	0.1	0.74	1.41	3.13	2.58	2.63	5.71	5.66	1.35	0.33	1.78

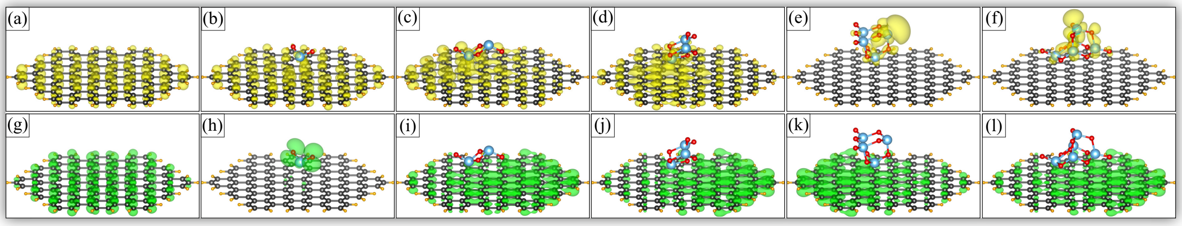

Figure 4.14: The decomposed charge density of (a, b, c, d, e, f) LUMO and (g, h, i, j, k, l) HOMO energy levels of $(TiO_2)_n$ clusters (n=0-5) on the surface of GQD. The isosurface level of charge density is taken to be that at 67.5×10^{-5} e⁻/Å^3 (1×10^{-4} e⁻/Bohr^3).

positions of the titania clusters and GQD's HOMO and LUMO states are affected in such a way that for some configurations, for instance, $(TiO_2)_1$, $(TiO_2)_4$, and $(TiO_2)_5$, photoelectrons can be expected to transfer across the interface. This will be favourable for ultrafast interfacial electron injection and reduce the electron recombination rate, thus increasing photocatalytic activity. It is especially valid if there is only weak hybridisation between the titania cluster and GQD's HOMO and LUMO states, as observed for $(TiO_2)_4$ and $(TiO_2)_5$, see Figure 4.14. Both the HOMO-LUMO quasiparticle gaps and the optical gaps of GQD bound clusters are significantly decreased compared to the bare $(TiO_2)_n$ clusters, as shown in Figure 4.11(c) and Table 4.6. A substantial reduction appears in the corresponding Stokes shifts as well. Interestingly, neither the spatial localisation nor the relative energy of the photoactive states exhibit a clear trend concerning the titania cluster size. Given that there are more titania cluster configurations than the minimum energy structures studied here[376] and an infinite number of alternative GQD structures and binding geometries, a wide variety of excitation and charge transfer scenarios can be expected.

4.3 Molecular Catalyst[g]

TiO_2, titania has emerged as one of the most promising photoanode and photocatalytic materials among the several photocatalytic semiconductor materials owing to its low cost, non-toxicity, excellent charge transfer, and long-standing physical and chemical stability.[399] As is well-known, the lack of visible light absorption inherent to titania prevents the full exploitation of the solar spectrum, resulting in a low energy conversion efficiency.[249, 338] Among the various known strategies for harvesting visible light, synthesising and designing organic dyes[h] are a typical and effective method to surmount this drawback by prolonging the light harvest.[400, 401] Furthermore, organic dyes can be readily functionalised to modify their spectroscopical and redox characteristics, in addition to their easy availability, low cost, and biocompatibility.

4.3.1 Overview

In particular, the D-π-A organic dyes[i] with an efficient ICT mechanism can boost the photoinduced charge separation, leading to remarkable photon-to-electron conversion.[404] Each of these three building components (donor, π-bridge and acceptor) can be easily interchanged, allowing for a wide variety of dye permutations.[405] Slight adjustments can also have a significant effect on their electronic and optical properties.[405] In order to enhance the light-harvesting efficiency of photocatalysis, the appropriate choice of donor and acceptor groups is essential. Generally, the ethylene-bridged dicationic derivate of bipyridine, DQ, is an intriguing moiety for application in D-π-A dyes. The ring system can undergo reversible and electron reductions to create radical cations and neutral species.[406, 407] Its redox-cycling capacity stimulates the formation of superoxide radicals and other reactive species. Incorporation of DQ moieties into a covalent organic framework can increase its photocatalytic hydrogen evolution activity through improved electron transport.[407]

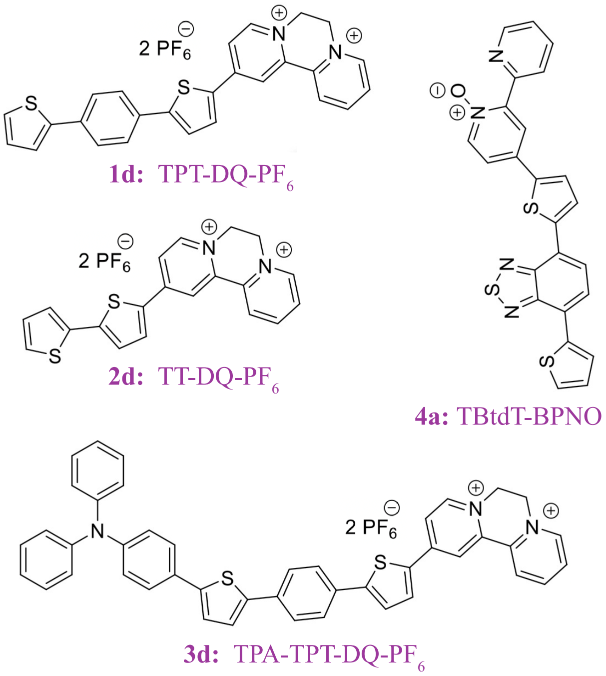
1d: TPT-DQ-PF_6

2d: TT-DQ-PF_6

4a: TBtdT-BPNO

3d: TPA-TPT-DQ-PF_6

Figure 4.15: Schematic representation of new dyes' molecular structures.

So far, several D-π-A organic dyes containing carbazole,[408–411] phenothiazine,[412–415] triphenylamine (TPA),[416–418] indole[419, 420], coumarin[421, 422] and perylene[423] units have been reported for photocatalyst. Furthermore, LR-corrected hybrid functionals have provided valuable guidance to current experiments for the investigation of D-π-A dyes and have given insight into more speculative systems not yet amenable to experimental study.[424–431] In this context, three new D-π-A dyes[j] with a DQ moiety as their acceptor group and one dye-based on thienyl-benzothiadiazo-thienyl (TBtdT) and bipyridine-oxide (BPNO) moiety (see Figure 4.15) are used in this study.

---

[g] Results and Discussion part of this section are the theoretical part of the paper, submitted to a peer-reviewed scientific journal.

[h] A natural or synthetic coloured molecule chemically binds to the substrate to which it is applied.

[i] This type of organic dye, extensively studied in dye-sensitised solar cells,[402, 403] consists of a conjugated π-system connecting an electron-rich donor moiety to an electron-poor acceptor moiety.

[j] 1d: thienylphenylthienyl (TPT)-DQ-PF_6, 2d: bithiophene (TT)-DQ-PF_6, 3d: TPA-TPT-DQ-PF_6

4.3.2 Results and Discussion

A series of new organic D-π-A dyes incorporating a DQ moiety as a novel electron-acceptor-unit have been synthesised successfully in the Institute of Organic Chemistry at the Clausthal University of Technology.[k] They display a high photocatalytic activity under visible light, giving isolated yields of up to 95 %. D-π-A dyes synthesis and experimental characterisation procedures are beyond the scope of this thesis. This part of the thesis focuses on the theoretical characterisation and investigates the electronic and optical properties of these new dyes. The corresponding computational details of this part study can be found in Appendix C.1.

Ground-State Geometries

In organic dyes, the degree of coplanarity affects the absorption spectra and charge-transfer characteristics. Figure 4.16 depicts the optimised geometries of 1d: TPT-DQ, 2d: TT-DQ, 3d: TPA-TPT-DQ and 4a: TBtdT-BPNO dyes. The dihedral angles between the rings in TT, TPT and TBtdT dyes are around (~3-8°), and these parts keep all of the dyes to have planar structures in all dyes. Small dihedral angles can provide better conjugation between the donor and acceptor part so that the acceptor can be more favourable for electron passage. The length of each C-C bond is around 1.37-1.51 Å in all new dyes, which is the distance between the double-bonded C=C (1.33 Å) and the single-bonded C-C (1.53 Å). This information indicates that there is extensive delocalisation throughout the molecules.

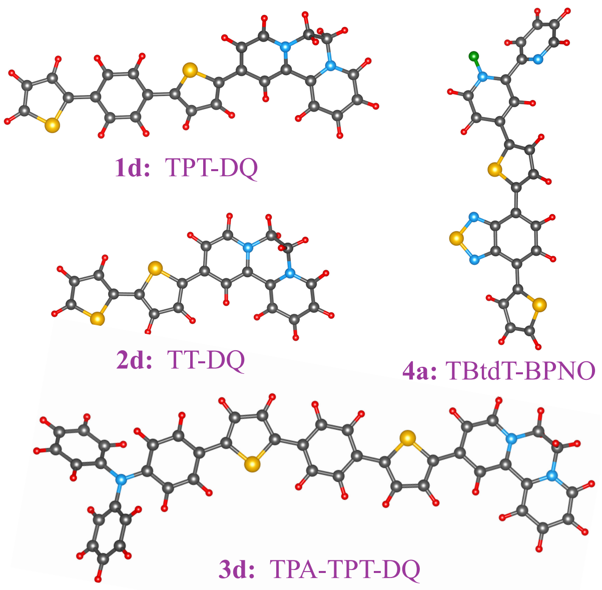

Figure 4.16: Optimised ground state geometry of new dyes' molecular structures. Blue, red, dark grey, orange and green spheres represent N, H, C, S and O atoms, respectively.

Electronic and Absorption Properties

The obtained HOMO and LUMO energy levels are shown in Figure 4.17 (a). It is well-known that the HOMO energy level is closely related to the donor part of the dye.[432] However, the acceptor part of the dye mainly influences the LUMO energy level.[432] As shown, the HOMO energy level of 3d dye (-6.43 eV) is higher than that of 1d (-7.23 eV), 2d (-7.49 eV) and 4a (-6.80 eV), indicating that the TPA unit has the more robust electron-donating characteristic than other donating groups of 1d, 2d and 4a dyes. The LUMO energy level of 4a dye (-2.85 eV) is below that of 1d, 2d and 3d dyes (-2.62 eV), which is based on BPNO moiety instead of DQ, manifests a different LUMO energy level. The results indicate that the LUMO energy level is negligibly sensitive to be affected by different π-conjugated bridges in 1d, 2d and 3d dyes. Higher LUMO energy levels can make the excited electron of these dyes effectively inject into TiO_2s' CB (usually, ~-4.0 eV)[432, 433]; the lower HOMO energy level of these dyes compared with the iodide/triiodide electrolyte (usually -4.80 eV) can also make the electron transfer from the redox shuttle to the oxidised dyes efficiently for the regeneration process.[432, 434] Accordingly, the calculated HOMO-LUMO energy gaps of these dyes increase in the following order 3d<1d<2d<4a with the corresponding values of 4.61 eV for 1d, 4.87 eV for 2d, 3.80 eV for 3d and 5.01 eV for 4a.

The IEs and EAs of the dyes calculated by the ΔSCF method are depicted in Figure 4.17 (a). The IEs and EAs can be compared with the oxidation and redox potential of dyes obtained from cyclic

---

[k] The experiments were done in the group of Prof. Dr. Wilhelm.

voltammogram measurements, see Figure A.10 (b) in Appendix C.2. The calculated -IEs or oxidation potentials of dyes are in good agreement with the experimental results. However, the computed -EAs or redox potential also fits the experiment, but it is more in line with the second experimental reduction potential than the first one. The IE value of 3d (5.27 eV) is lower than that of 1d (6.08 eV) and 2d (6.22 eV), so the absence of the TPA unit in 1d and 2d dyes can cause these dyes to lose electrons more easily, resulting in their slightly better photoelectric properties. While comparing the EAs of the dyes, 1d, 2d and 3d dyes must possess a better electron-accepting ability than the 4a dye.

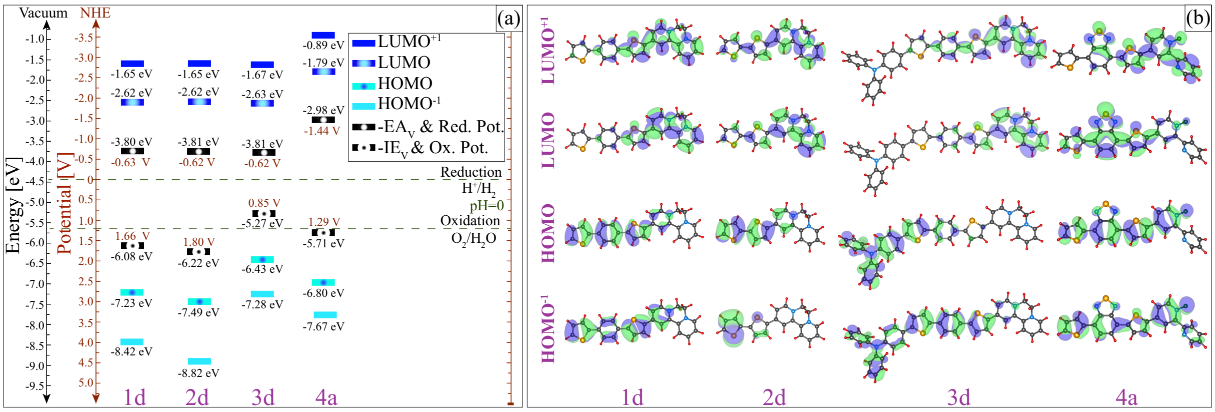

Figure 4.17: (a) Calculated energies of the frontier molecular orbitals (HOMO^{-1}, HOMO, LUMO, LUMO^{+1}), and redox and oxidation potential of 1d, 2d, 3d, and 4a dyes in relation to the redox reactions of water splitting. (b) Isosurface plots of corresponding orbitals orbitals of 1d, 2d, 3d, and 4a dyes.

Absorption spectra of the 1d, 2d, 3d and 4a dyes computed using TDDFT with CAM-B3LYP LR-corrected hybrid functional is shown in Figure 4.18 (a). Remarkably, the positions of the first maximal peak of the 1d (457 nm), 2d (450 nm), 3d (536 nm) and 4a (452 nm) dyes, corresponding to mainly the HOMO→LUMO transition are in good agreement with the experimental value of the 1d (473 nm), 2d (467 nm), 3d (507 nm) and 4a (465 nm) dyes, see Figure A.10 (a) in Appendix C.2. As expected from the previously reported results,[427–431] TDDFT with CAM-B3LYP LR-hybrid functional performs particularly well for simulating charge transfer energies of D-π-A dyes.

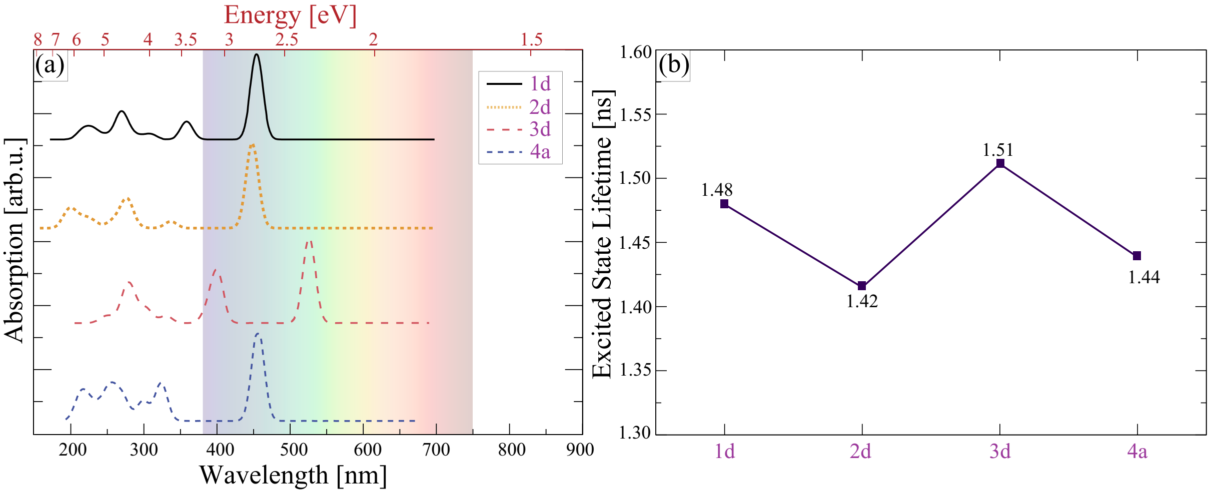

Figure 4.18: (a) Absorption spectra and (b) first excited state lifetimes of 1d, 2d, 3d and 4a dyes calculated with TDDFT. The spectra were simulated using 20 nm Gaussian broadening.

The electron density distribution over the frontier molecular orbitals (HOMO^{-1}, HOMO, LUMO, LUMO^{+1}) is illustrated in Figure 4.17 (b). For the three dyes with the DQ electron-acceptor moiety, 1d, 2d, and 3d, the electron density distribution over the frontier orbitals is in favour of an ICT nature of the excitation. The electron density of the LUMO of these three dyes clearly shows predominant localisation on the DQ electron-acceptor moiety. Their HOMO electron density is localised on the electron-donating parts showing the overlap with the LUMO onto the π-linker. These results confirm that the HOMO→LUMO transition in 1d, 2d and 3d is accompanied by the ICT from the electron donor group to the electron acceptor moiety through the π-linker. At the same time, the 4a dye based on BPNO moiety instead of DQ displays different electron density distributions along the frontier orbitals. The electron density of LUMO is predominantly localised in the electron-donating part of the molecule. Accordingly, the HOMO→LUMO transition of 4a dye cannot be regarded as an ICT transition, and it can be instead interpreted as a $\pi \rightarrow \pi^*$ excitation. To some extent, the ICT character can be attributed to the HOMO→LUMO^{+1} transition providing a rise to the absorption peak at 341 nm. The calculated first excited state lifetimes[l] of the dyes are depicted in Figure 4.18 (b). The results display that the excitation lifetimes of the 1d, 2d, 3d and 4a dyes in the first excited states are 1.48, 1.42, 1.51 and 1.44 ns, respectively. Generally, longer excited-state lifetimes correlate well with the observed trends in photocatalytic activity. Hence, 1d and 3d dyes would have a relatively higher electron injection performance than 2d and 4a dyes, which is expected to inhibit electron recombination more effectively in 1d and 3d dyes.

---

[l] The lifetime of the dye in the excited state is one of the most critical factors for assessing the efficiency of charge transfer via electron injection into a semiconductor substrate (for example, TiO_2) in the excited state. It estimates the time required for the dye to inject electrons into the semiconductor substrate. Until regeneration by a redox mediator, the dye is in a cationic state following electron injection. The longer lifetime (τ) in the excited state means that the dye spends more time in its cationic form and has higher optical stability, which is advantageous for charge transfer.

"As a man who has devoted his whole life to the most clearheaded science, to the study of matter, I can tell you as a result of my research about the atoms this much: There is no matter as such! All matter originates and exists only by virtue of a force which brings the particles of an atom to vibration and holds this most minute solar system of the atom together.... We must assume behind this force the existence of a conscious and intelligent Spirit. This Spirit is the matrix of all matter."

— Max Planck,
Speech on The Nature of Matter
Florence, 1944.

5

Conclusion and Perspectives

At the end of this study, the easiest way to summarise the conclusions is to go back and read the objective presented in the introduction and then follow how these results have been processed in this thesis. Briefly, DFT-based methods with SIC were employed to study some photocatalyst material systems, **(i)** titania bulk phases and amorphous thin-film, **(ii)** titania clusters and their combination with GR and GQD, and **(iii)** new organic D-π-A type catalyst dyes.

(i) TiO_2 crystals were systematically studied by performing Hubbard U correction and hybrid functional methods in DFT. Combining self-consistently determined U_d correction for Ti^{3d} states with semi-empirically determined U_p correction for O^{2p} states provides an approach to improve the accuracy of electron band structures calculated by DFT at modest numerical costs. The numerically more expensive hybrid DFT, particularly the PBE0 functional, provides similarly accurate electronic structure data and highly accurate atomic structures. However, the DFT+U_p and hybrid DFT provided more accurate optical excitation energies than DFT+$U_{p,d}$ by comparing with experimentally observed findings. In addition to describing the main results of the applications, several analyses have been carried out to rationalise the corrections provided by the DFT+U approach, which could benefit future research in this field. For example, the DFT+U_p (U_p correction for O^{2p} states) and hybrid DFT methods with the proposed methodology have been used to study TiO_2 amorphous thin-films. The results confirm that the proposed methodology can be generalised to study TiO_2-based *disordered* structures.

(ii) The structural, electronic, and optical properties of neutral TiO_2 clusters and TiO_2 clusters adsorbed on pristine GR and GQDs were studied by DFT, hybrid functional and CDFT methods. Compared to bulk titania, the optical gap of TiO_2 clusters is much reduced and resides in the spectral range of visible light. A further reduction occurs upon adsorption on GR and GQD where vdW interaction dominates. In addition to the red-shifted absorption, spatial separation of photoexcited charge carriers can also occur for many bonding scenarios, significantly boosting the photocatalytic activity of the hybrid material compared to its constituent components. The electronic properties of the hybrid material depend sensitively on the size of the respective constituents and are highly system specific. This allows for tuning and optimising the material concerning its desired properties for specific excitation wavelengths.

(iii) DFT and TDDFT methodology performed to investigate the electronic and absorption properties of new class three D-π-A dyes as photocatalyst with a DQ moiety as their acceptor group and one dye based on TBtdT and BPNO moiety by using LR-corrected hybrid functional (CAM-B3LYP). All new D-π-A dyes' absorption spectra exhibit the most intense peak in the visible light range dominated by the single-electron HOMO→LUMO transition. Calculations confirmed that the HOMO→LUMO transition in 1d, 2d and 3d is accompanied by the ICT, but the HOMO→LUMO transition of 4a dye could not be considered as an ICT transition, and it could be rather an interpreter as $\pi \rightarrow \pi^*$ excitation. The excited state with highly efficient charge separation properties can be propitious to the ultrafast interfacial electron injection and reduce the electrons recombination rate. The LR-corrected hybrid functional can be the optimum way to study D-π-A dyes and their derivatives.

Overall, this thesis's results demonstrate the applicability of the DFT+U, hybrid functionals and CDFT methodologies to investigate the electronic and optical properties of photocatalyst systems. There are several directions in which the work presented in this thesis can also be pursued and suggest some future research tasks and challenges, such as:

- detailed investigation of the correlation between TiO_2 amorphous thin-films and photocatalytic activity at the atomic level;
- modelling the different types of quantum dots and clusters for understanding the photocatalyst process of proposed systems;
- investigation of the different types of D-π-A organic dyes on the surface of the GR and TiO_2 structures or amorphous thin-film to understand the processes further and improve the photoactivity;

in both fundamental understanding and implementation.

Appendix

A Computational and Supporting Details on Titania

This part is to provide the computational and supporting details on titania, as discussed in Section 4.1.

A.1 Computational Details

DFT[36–38] within the GGA using the PBE and $\mathrm{PBE_{sol}}$ functional[a][98, 99] in conjunction with Grimme's D2 correction[176, 182] to account for dispersion interactions was the starting point of the present calculations. The QE package implementation [127, 128] with NC-PPs was used. The electron orbitals were expanded on the PW basis with an energy cutoff of 150 Ry. Energy and force convergence criteria of 10^{-10} Ry and 10^{-6} Ry/bohr were applied to determine the structurally relaxed ground state. The BZ sampling was performed using $8 \times 8 \times 12$, $10 \times 10 \times 4$, and $3 \times 5 \times 5$ MP k-point mesh for R-, A-, and B-$\mathrm{TiO_2}$ unit cells, respectively. PBE0[219, 222] and HSE[229, 230] were used for global- and screening hybrid functionals. In the HSE, the screening parameter ω was chosen to equal 0.106 bohr^{-1}.

The electronic structures calculated with $\mathrm{PBE_{sol}}$, $\mathrm{PBE_{sol}}$+$\mathrm{U_d}$, $\mathrm{PBE_{sol}}$+$\mathrm{U_p}$, $\mathrm{PBE_{sol}}$+$\mathrm{U_{d,p}}$, and PBE0 were used to calculate the dielectric function within the IPA[116]; that is, do not account for LFE and electron-hole attraction[435]. Specifically, the tensor elements in the long-wavelength limit are calculated as follows:

$$\varepsilon_{\beta\beta}(\omega) = 1 + \frac{16\pi}{\Omega} \sum_{\upsilon,c} \sum_{\mathbf{k}} \frac{1}{\varepsilon_{c\mathbf{k}} - \varepsilon_{\upsilon\mathbf{k}}} \frac{|\langle \upsilon\mathbf{k}| p_\beta + i[V^{nl}, r_\beta] |c\mathbf{k}\rangle|^2}{(\varepsilon_{c\mathbf{k}} - \varepsilon_{\upsilon\mathbf{k}})^2 - (\omega + i\gamma)^2}, \tag{A.1}$$

where β denotes the spatial direction. Following the usual convention of identifying the three-fold axis of symmetry with the z-direction, the x-direction is perpendicular to the z-direction and lies in the plane spanned by the three-fold axis of symmetry, one of the three equivalent basis vectors of the primitive orthorhombic unit cell. The sum runs over all VB and CB states and the wave vectors in the BZ. The transition dipole moments include the commutator with the nonlocal part of the PPs, Ω is the cell volume, and γ the broadening. The Yambo package[436, 437] was used for the numerical evaluation.

---

[a] Since $\mathrm{PBE_{sol}}$ functional gives more accurate crystal structures parameters than PBE, see Table 4.2 and Table A.1, the $\mathrm{PBE_{sol}}$ is considered further calculations.

A.2 Supporting Details

Table A.1: Calculated unit cell parameters **a**, **b**, **c** (in Å) and volume **V** (in $\mathrm{\AA}^3$) of R-, A-, and B-TiO_2 in comparison to experiment. U_d values are equal to 5.92, 5.96, and 5.95 eV for the respective Ti^{3d} states of R-, A-, and B-TiO_2 in PBE+U_d and PBE+$U_{p,d}$, whereby U_p for the respective O^{2p} states is chosen equal to 4.2 eV. Relative deviations are given with respect to the mean of experimental data.

Method	Rutile			Anatase			Brookite			
	a = b	c	V	a = b	c	V	a	b	c	V
PBE	4.600	2.977	62.99	3.784	9.728	139.29	9.230	5.477	5.156	260.65
	+0.1%	+0.7%	+0.9%	-0.0%	+2.2%	+2.2%	+0.5%	+0.6%	+0.1%	+1.1%
PBE+U_d	4.623	3.077	65.76	3.867	9.771	146.11	9.324	5.537	5.293	273.26
	+0.6%	+4.1%	+5.3%	+2.2%	+2.7%	+7.2%	+1.5%	+1.5%	+2.8%	+6.0%
PBE+$U_{d,p}$	4.584	3.062	64.34	3.832	9.754	143.23	9.263	5.495	5.265	267.99
	-0.2%	+3.6%	+3.1%	+1.2%	+2.5%	+5.1%	+0.9%	+0.8%	+2.2%	+3.8%
HSE	4.563	2.953	61.48	3.707	9.949	136.72	9.202	5.418	5.109	254.72
	-0.7%	-0.1%	-1.5%	-2.1%	+4.6%	+0.3%	+0.2%	-0.6%	-0.8%	-1.2%
PBE0	4.573	2.960	61.90	3.738	9.783	136.69	9.175	5.441	5.133	256.25
	-0.5%	+0.1%	-0.8%	-1.2%	+2.8%	+0.3%	-0.1%	-0.2%	-0.3%	-0.6%
Experiments	4.604	2.959	62.72[303]	3.787	9.518	136.50[303]	9.184	5.454	5.146	257.76[303]
	4.587	2.954	62.15[304]	3.784	9.515	136.24[305]	9.180	5.457	5.158	258.39[306]
	4.593	2.959	62.42[307]	3.785	9.514	136.30[307]	9.184	5.447	5.145	257.38[308]

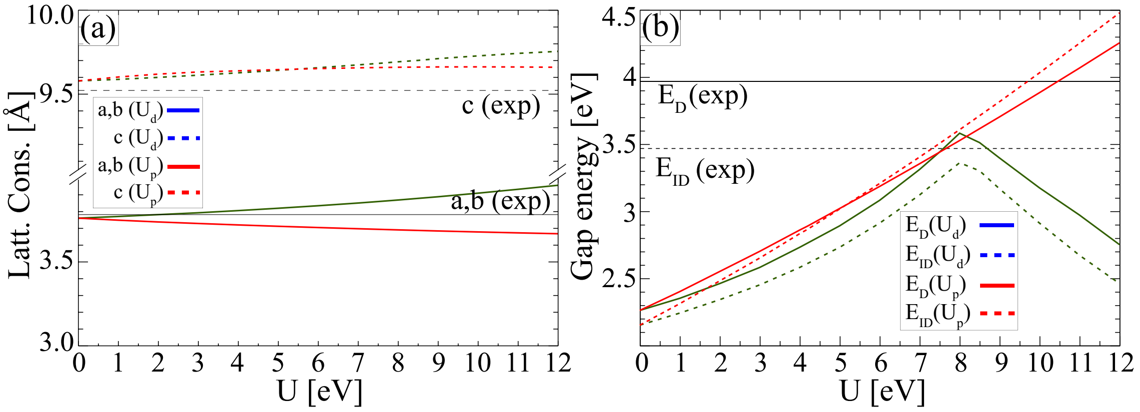

Figure A.1: Lattice parameters (a) and fundamental bandgap (b) of A-TiO_2 crystal calculated as a function of U values.

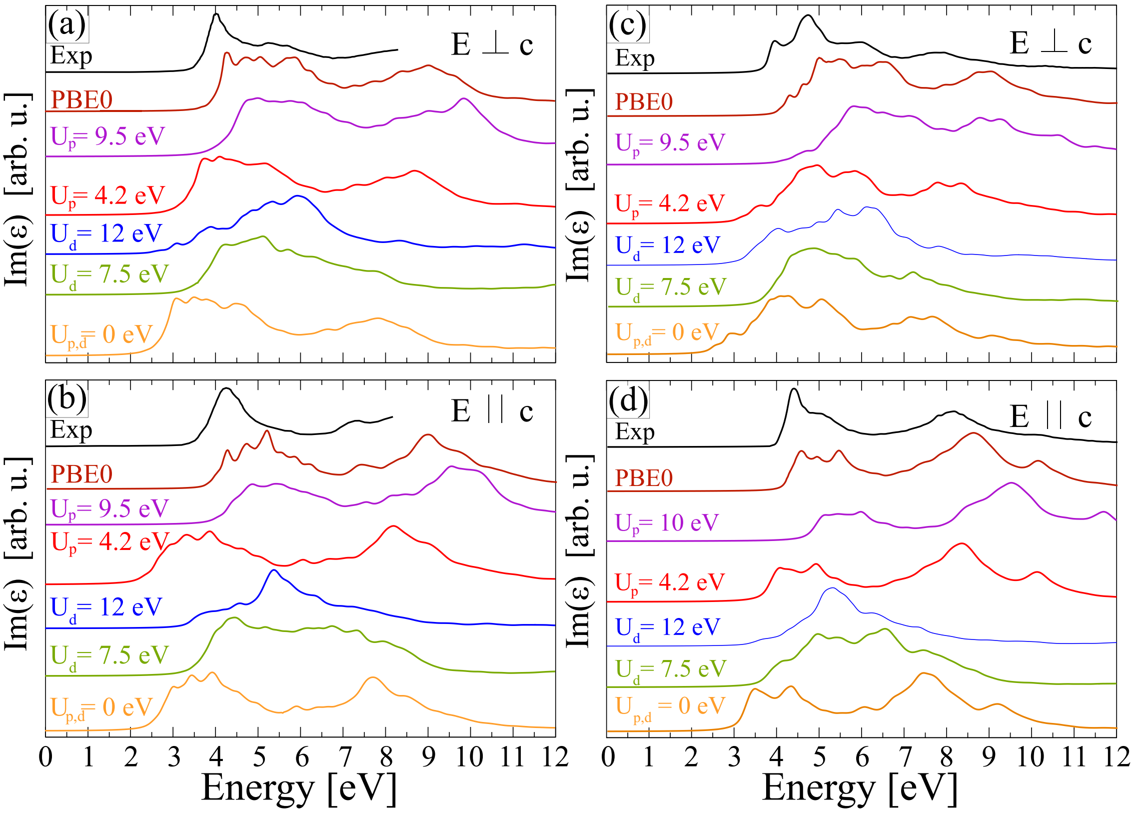

Figure A.2: Imaginary part of the R- and A-TiO_2s' complex dielectric function calculated within IPA based on the PBE_{sol}+U in comparison to experimental data from Ref. [317].

B Computational and Supporting Details on Titania-Graphene Composite System

This part is to provide the computational and supporting details on Titania-Graphene Composite, as discussed in Section 4.2.

B.1 Computational Details

The DFT[36–38] calculations were performed using the VASP.[126] The electron XC energies were described within the GGA using the PBE functional.[98] As stated in Section 2.8.4, the accurate modelling of weakly bonded adsorbates is a significant challenge for DFT since semi-local XC functionals do not adequately describe the LR vdW interactions.[172–175] In order to account approximately for dispersion interaction, a semi-empirical dispersion correction scheme based on the London dispersion formula,[159] the called DFT-D scheme, was used.[171, 180–182] Specifically, the DFT-D2 method was used.[176] Test calculations using DFT-D3[182] and DFT-D3BJ[167, 182] revealed only negligible deviations. The Bader technique[438] was used to determine the charge transfer between TiO_2 clusters and GR/GQD, and to analyse the chemical bonding.

The kinetic energy cutoff for PW expansion was 500 eV, and the energy and force convergence criteria were 10^{-5} eV and 10^{-4} eV/Å, respectively. $4 \times 4 \times 1$ Γ-centred k-point sampling was used for TiO_2 clusters in the $6 \times 6 \times 1$ supercell of GR for geometry optimisations and electronic band structure calculation. Gaussian smearing[439] width was set at 0.05 eV for all geometry and band structure calculations. The PDOS was calculated with the above computational parameters, except that the tetrahedral smearing with Blöchl corrections[440] and the denser $9 \times 9 \times 1$ k-point grid were used. All $(TiO_2)_n$ clusters (n=1-5) and their interaction with GR were calculated in a hexagonal supercell with a lattice parameter of 14.81 Å. A cubic supercell with a lattice parameter of 32 Å was used to model TiO_2 clusters interacting with hexagonal armchair GQD. In order to minimise the interaction between adjacent clusters or material slabs, a minimum vacuum space of 10 Å was used for separation.

The cohesive energy per atom E_{Coh} was calculated as follows:

$$E_{Coh} = \frac{1}{n_{Tot}} \left[\sum_{i=1} n_i E_i - E_{st} \right], \tag{A.2}$$

where the E_i represents the energies of a single isolated atom, and the i index denotes the type of atom. E_{st} represents the total ground state energy of the related structures. n_{Tot} and n_i are the numbers of total and isolated i-type atoms in the unit cell, respectively. The binding energy of adsorbed clusters was calculated as follows:

$$E_b = -E_{ads} = E_{GR/GQD} + E_{cl} - E_{GR/GQD+cl}, \tag{A.3}$$

where the $E_{GR/GQD}$ denotes the energy of the GR or GQD, E_{cl} is the energy of an isolated adcluster, and $E_{GR/GQD+cl}$ denotes the total energy when the adcluster is adsorbed on GR or GQD.

The DFT-GGA electronic structure is known to suffer from an underestimation of electronic excitation energies, as it does not account accurately for electronic self-energy effects.[100, 119] Moreover, optical excitation energies cannot be directly concluded from ground-state DFT calculations, as they neglect electron-hole attraction. In order to account for this shortcoming, the HSE06 hybrid functional was also used for electronic structure calculations.[230] DFT-GGA and HSE06 eigenvalues of the HOMO and LUMO states were aligned with respect to vacuum level; that is, the vacuum level of clusters, being obtained from a total local electrostatic potential calculation, was subtracted from molecular orbital energy levels. The EA, IE, quasiparticle energy gap and optical gap were calculated within the ΔSCF method.[102–105]

B.2 Supporting Details

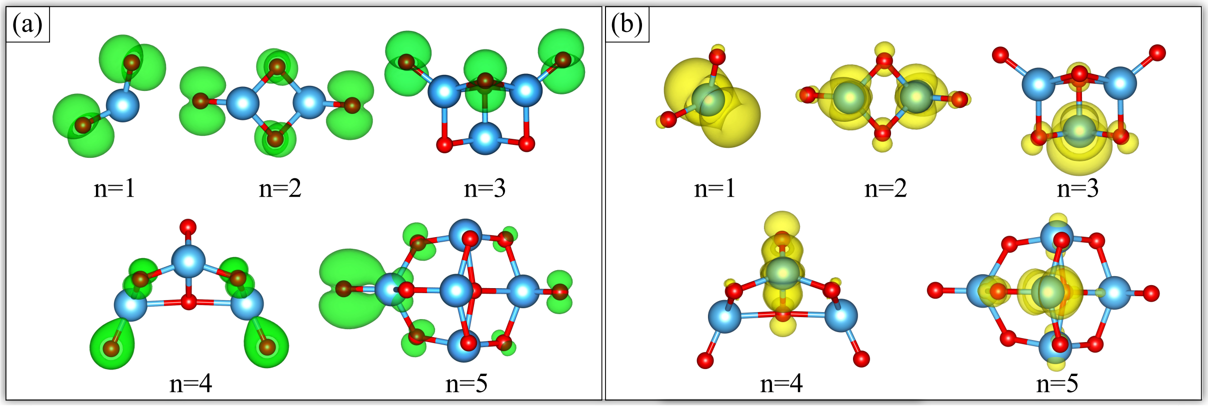

Figure A.3: The decomposed charge density plots of (a) HOMO and (b) LUMO of $(TiO_2)_n$ clusters (n=1-5). The isosurface level of charge density is taken to be that at 67.5×10^{-5} e⁻/$\mathring{A}^3$ (1×10^{-4} e⁻/Bohr^3).

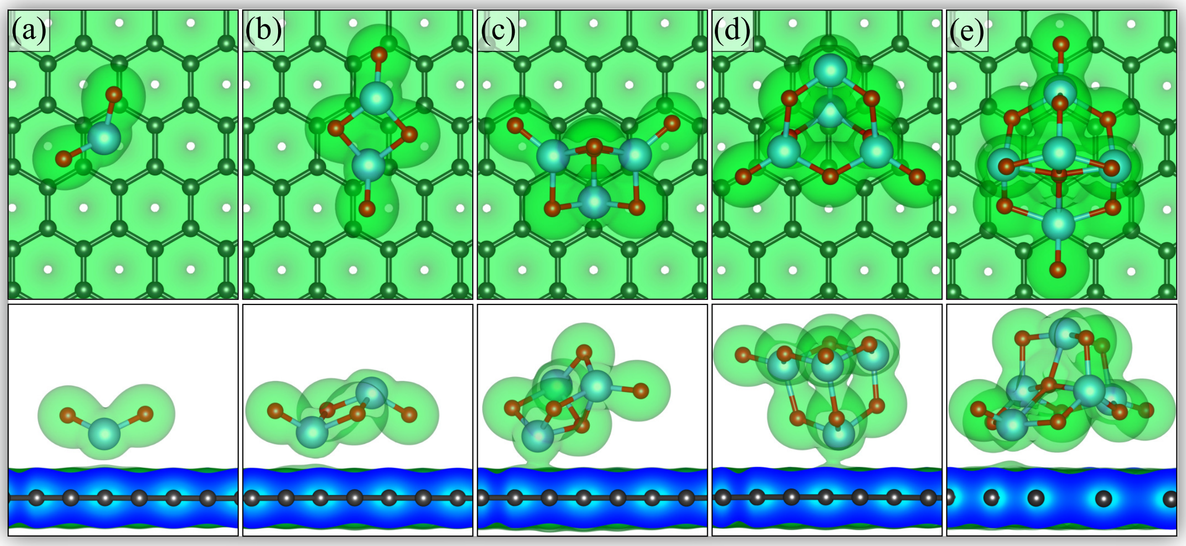

Figure A.4: The top and side views of the total charge density of $(TiO_2)_n$ clusters on the surface of GR at (a) n=1, (b) n=2, (c) n=3, (d) n=4, and (e) n=5. The isosurface level of charge density is taken to be that at 0.169 e⁻/$\mathring{A}^3$ (0.025 e⁻/Bohr^3).

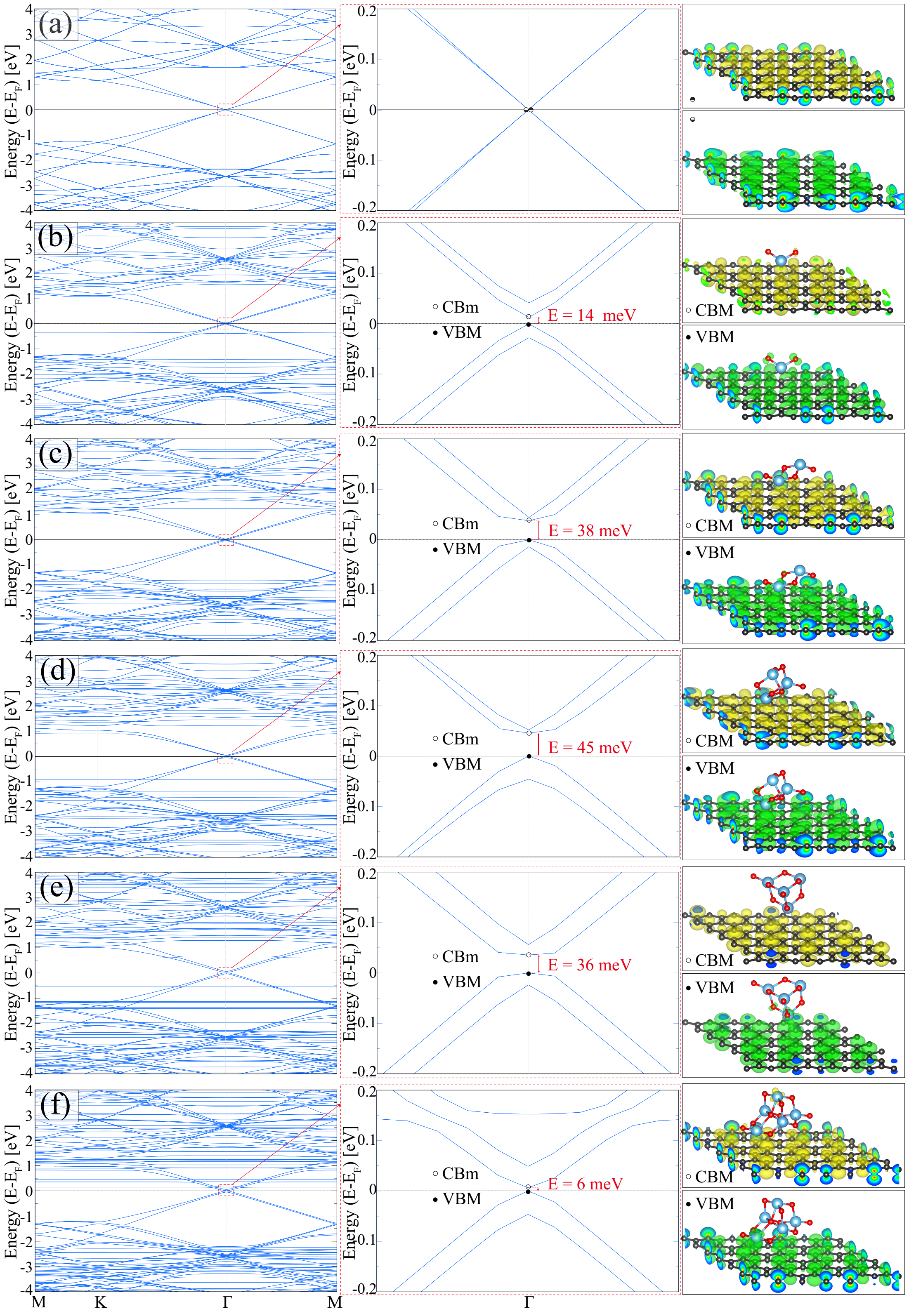

Figure A.5: The band structure and the decomposed charge density of VB maximum and CB minimum of the $(TiO_2)_n$ clusters on the surface GR at (a) n=0, (b) n=1, (c) n=2, (d) n=3, (e) n=4, and (f) n=5. In the case of $(TiO_2)_n$/GR, the Dirac cone at the Γ and the folded bands due to the (6×6) GR supercell structure of the system are present in the plot. The second column views show the corresponding VB maximum and CB minimum on an enlarged scale. The isosurface level of charge density is taken to be that at 67.5×10^{-5} e$^-$/Å^3 (1×10^{-4} e$^-$/Bohr^3).

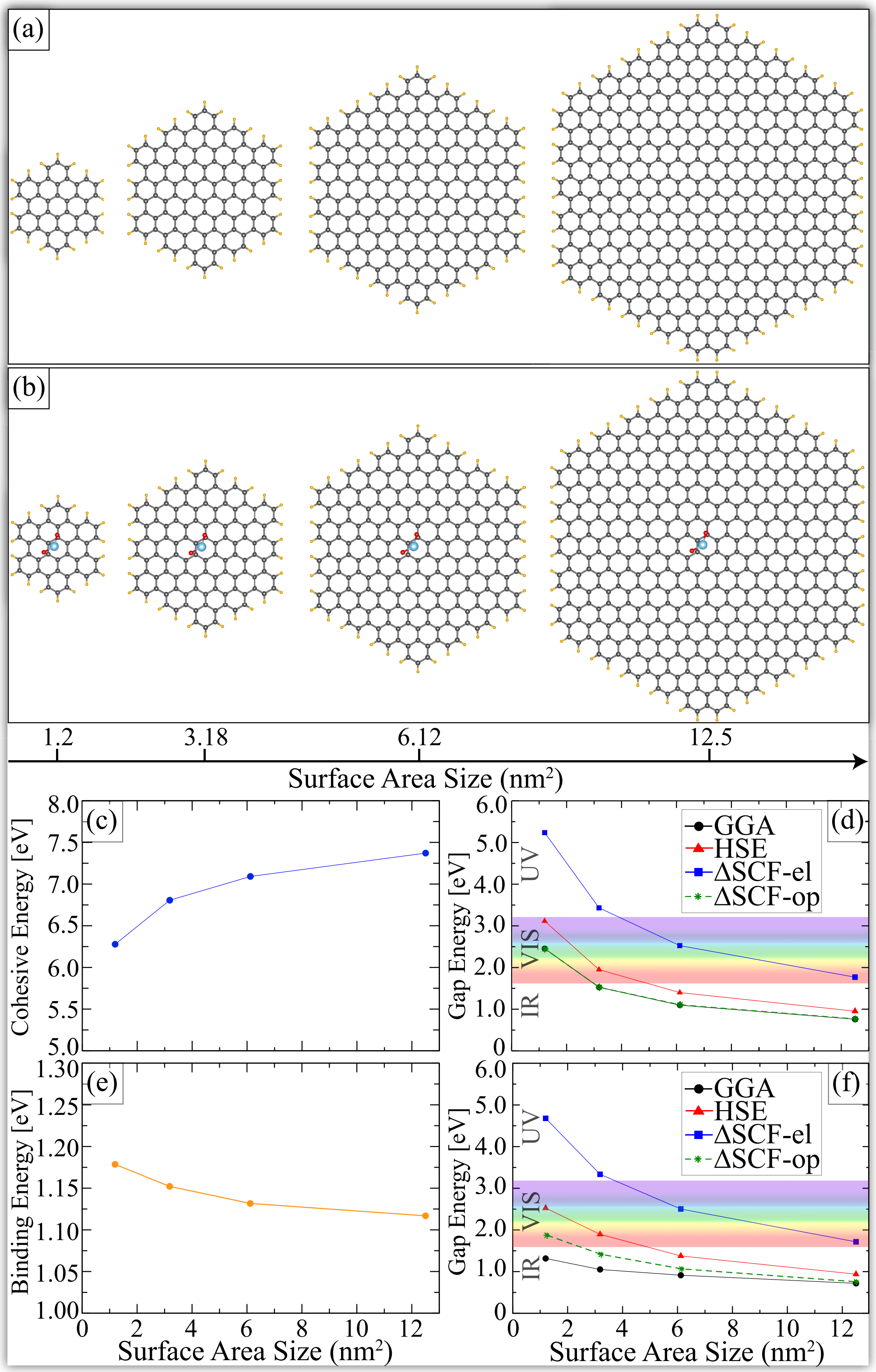

Figure A.6: The top views of (a) optimised hexagonal GQDs with armchair edges and (b) the most favourable $(TiO_2)_1$ adsorption configuration on the respective GQDs. Blue, red, dark grey, and orange spheres represent Ti, O, C, and H atoms, respectively. (c) The cohesive energy per atom and (d) the HOMO-LUMO energy gap and the optical gap of GQDs. (e) The $(TiO_2)_1$ bonding energy on the GQD and (f) the HOMO-LUMO energy gap and the optical gap of $(TiO_2)_1$ decorated GQDs. For comparison, the spectral energy of visible light (1.59-3.26 eV) is indicated.

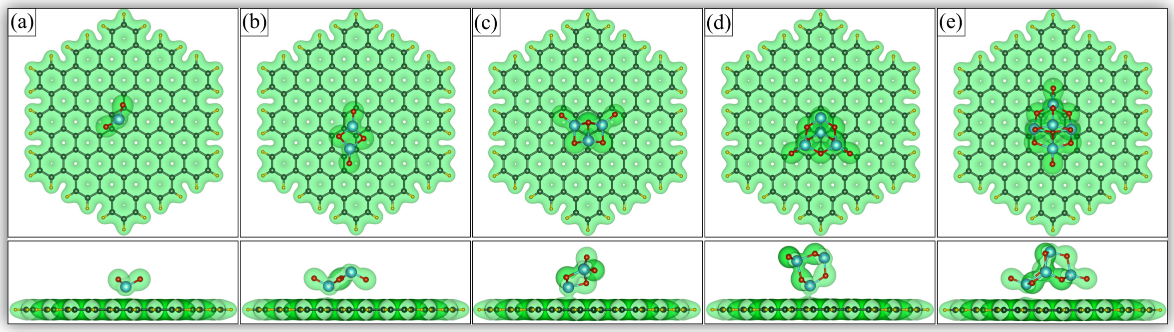

Figure A.7: The top and side views of the total charge density of $(TiO_2)_n$ clusters on the surface of GQD at (a) n=1, (b) n=2, (c) n=3, (d) n=4, and (e) n=5. The isosurface level of charge density is taken to be that at 0.169 $e^-/Å^3$ (0.025 $e^-/Bohr^3$).

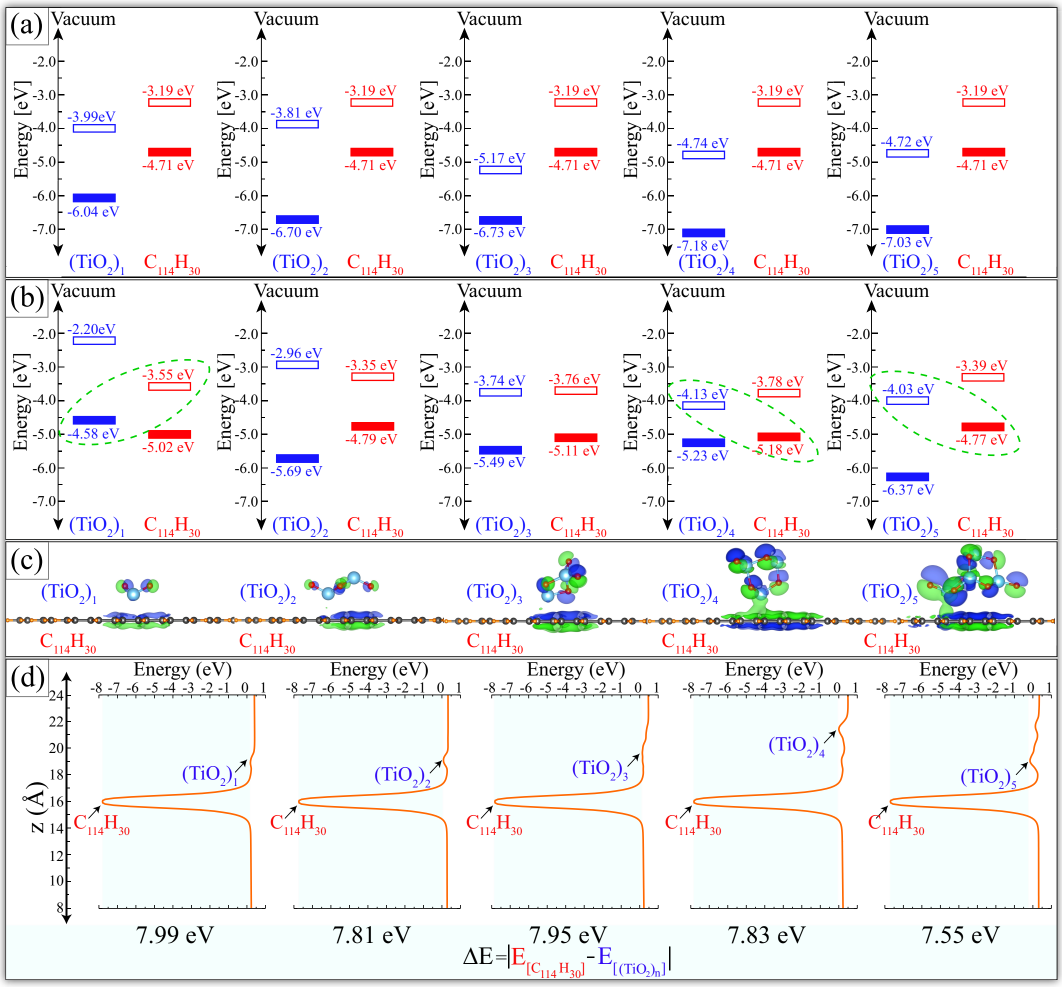

Figure A.8: HOMO-LUMO energy levels for (a) isolated and (b) combined $(TiO_2)_n$/GQD systems calculated on the DFT-GGA level of theory. The charge density difference distribution $\Delta\rho$ between GQD and TiO_2 clusters. The green and blue colours represent the charge accumulation and depletion, respectively. The isosurface level of charge density is taken to be that at 0.067 $e^-/Å^3$ (0.01 $e^-/Bohr^3$). (d) Local electrostatic potential diagrams versus combine $(TiO_2)_n$/GQD systems. ΔE is the electrostatic potential difference.

C Computational and Supporting Details on Molecular Catalyst

This part is to provide the computational and supporting details on Molecular Catalyst, as discussed in Section 4.3.

C.1 Computational Details

The experimental results were complemented by DFT[36–38] and TDDFT[108] calculations. The calculations were performed with the ORCA[129] using the def2-TZVP[141] basis set combined with the RIJCOSX[441] auxiliary basis set. In both ground and excited-state calculations, Grimme's DFT-D3 approach with Becke-Johnson damping[167] was employed to account for dispersion interactions, and the conductor-like polarisable continuum model within the self-consistent reaction field theory was used to treat bulk solvent effects of Acetonitrile.[b][442]

Table A.2: TDDFT calculations: Influence of XC functionals; E_g is HOMO-LUMO energy gap; λ_{abs} is HOMO-LUMO charge transfer energy.

Functional	E_g (eV)	λ_{abs} (nm)
PBE	1.37	1023
HF	8.40	301
B3LYP	2.58	599
PBE0	2.89	544
TPSSh	2.00	716
ωB97	6.66	385
ωB97X	7.09	337
CAM-B3LYP	5.02	452

In order to verify whether the absorption properties of the new dyes obtained by quantum computations correspond to our expectations, it was necessary to compare the absorption properties obtained theoretically with those obtained experimentally to select a reasonable XC functional for TDDFT calculation. For this purpose, several XC functionals (PBE, HF, B3LYP, PBE0, TPSSh, ωB97, ωB97X and CAM-B3LYP) were tested on the reference dye 4a: TBtdT-BPNO, see Table A.2 and Figure A.9. In here, the LR-corrected hybrid functional CAM-B3LYP tends to outperform all other approaches.

In particular, CAM-B3LYP functional result is in good agreement with the experimentally obtained value. Generally, CAM-B3LYP performs well for simulating charge-transfer excitation in the organic D-π-A dyes, which is the expected result based on previously reported results.[427–431] Both ground and excited-state properties were studied using optimised ground-state geometries without any constraint. In order to save computational time, the two-unit hexafluorophosphate anion (PF_6) in the 1d, 2d and 3d dyes was replaced by the total charge equal $2e^-$ due to its negligible effect on the electronic and geometrical structures of the dyes. Bader charge analysis of dyes also confirms that 1d, 2d, and 3d dyes with $2PF_6$ lose exactly $2e^-$ charge.

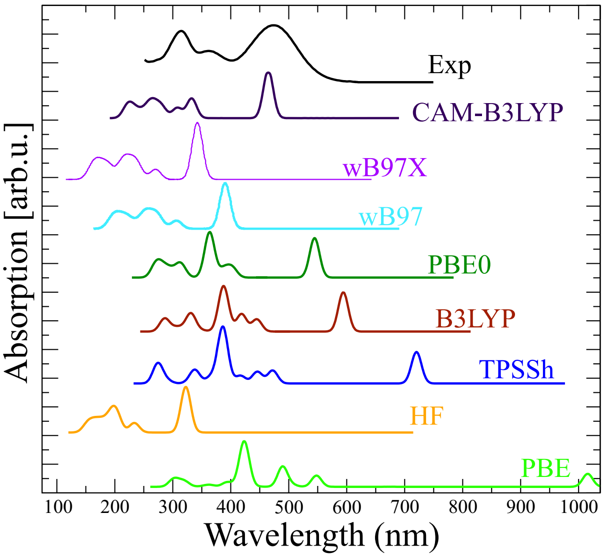

Figure A.9: Absorption spectra of 4a: TBtdT-BPNO dye calculated with TDDFT as function of different functional.

The excited state lifetime of a dye can be calculated using the following equation:

$$\tau = \frac{1.499}{\mathrm{f} \cdot \mathrm{E}^2}, \tag{A.4}$$

where E is the excitation energy of the different electronic states (cm^{-1}) and f is the oscillator strength of the respective electronic state.[431]

---

[b] It was considered as solvent in analogy with the experimental measurements.

C.2 Supporting Details

The redox potentials were analysed utilising cyclic voltammetric techniques.[c] The reduction of the 1d-3d dyes exhibited a reversible two-step reduction consistent with the formation of radical cations and neutral species. With first and second reduction potentials of around -0.16 V and -0.55 V, the substrate scope for catalytic reductions of organic molecules would be constrained. Nevertheless, oxidative quenching is conceivable by O_2. 1d: TPT-DQ dye's oxidation potential was measured to be roughly +1.6 V, sufficient to allow the oxidation of electron-rich organic compounds. 2d: TT-DQ dye's oxidation potential was not observed in cyclic voltammetric measurement under the selected circumstances, but it should be larger than that of 1d: TPT-DQ dye. Due to the strong electron-donating properties of the TPA, 3d: TPA-TPT-DQ dye has a significantly lower oxidation potential of roughly +1.09 V, whereas the second oxidation occurs at +1.26 V. 4a: TBtdT-BPNO dye exhibited two-step oxidation, with oxidation potentials of +1.31 V and +1.47 V, respectively. Multiple reductions are also recorded at around -0.86 V, -1.44 V, and -1.70 V, which is particularly interesting. With these redox potentials, 4a dye has the potential to catalyse both the oxidation and reduction of extremely electron-rich and electron-deficient molecules, respectively.

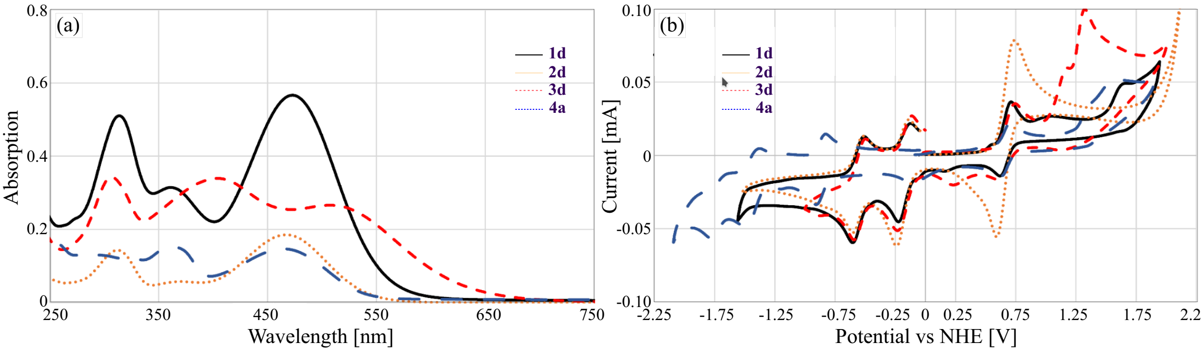

Figure A.10: (a) Experimental absorption spectra of dyes, measured at 10^5 mol/L in MeCN and (b) Cyclic voltammogram measurement of the dyes, with NBu_4PF_6 as electrolyte and ferrocene as standard at +0.66 V. Data was provided by A. Meier and Prof. R. Wilhelm.

---

[c] A. Meier and Prof. R. Wilhelm provided it.

Bibliography

[1] J. Harris, Ecol. Econ **50**, 315 (2004).

[2] D. Gielen, F. Boshell, D. Saygin, M. D. Bazilian, N. Wagner, and R. Gorini, Energy Strategy Rev. **24**, 38 (2019).

[3] G. W. Crabtree and N. S. Lewis, Phys. Today **60**, 37 (2007).

[4] N. Armaroli and V. Balzani, Chem. Eur. J. **22**, 32 (2016).

[5] N. S. Lewis, Science **351**, aad1920 (2016).

[6] D. S. Mallapragada, N. A. Sepulveda, and J. D. Jenkins, Appl. Energy **275**, 115390 (2020).

[7] J. Kosco, S. Gonzalez-Carrero, C. T. Howells, T. Fei, Y. Dong, R. Sougrat, G. T. Harrison, Y. Firdaus, R. Sheelamanthula, B. Purushothaman, F. Moruzzi, W. Xu, L. Zhao, A. Basu, S. De Wolf, T. D. Anthopoulos, J. R. Durrant, and I. McCulloch, Nat. Energy **7**, 340 (2022).

[8] B. C. Tashie-Lewis and S. G. Nnabuife, Chem. Eng. J. Adv. **8**, 100172 (2021).

[9] G. Ciamician, Science **36**, 385 (1912).

[10] A. Fujishima and K. Honda, Nature **238**, 37 (1972).

[11] R. I. Bickley and R. K. M. Jayanty, Faraday Discuss. Chem. Soc. **58**, 194 (1974).

[12] J. H. Carey, J. Lawrence, and H. M. Tosine, Bull. Environ. Contam. Toxicol. **16**, 697 (1976).

[13] S. N. Frank and A. J. Bard, J. Phys. Chem. **81**, 1484 (1977).

[14] T. Inoue, A. Fujishima, S. Konishi, and K. Honda, Nature **277**, 637 (1979).

[15] S. Yamagata, S. Nakabayashi, K. M. Sancier, and A. Fujishima, Bull. Chem. Soc. Jpn **61**, 3429 (1988).

[16] R. Wang, K. Hashimoto, A. Fujishima, M. Chikuni, E. Kojima, A. Kitamura, M. Shimohigoshi, and T. Watanabe, Nature **388**, 431 (1997).

[17] D. M. Schultz and T. P. Yoon, Science **343**, 1239176 (2014).

[18] M. H. Shaw, J. Twilton, and D. W. MacMillan, J. Org. Chem. **81**, 6898 (2016).

[19] K. Hashimoto, H. Irie, and A. Fujishima, Jpn. J. Appl. Phys. **44**, 8269 (2005).

[20] Q. Wang and K. Domen, Chem. Rev. **120**, 919 (2020).

[21] C. Gao, J. Low, R. Long, T. Kong, J. Zhu, and Y. Xiong, Chem. Rev. **120**, 12175 (2020).

[22] M.-Y. Qi, M. Conte, M. Anpo, Z.-R. Tang, and Y.-J. Xu, Chem. Rev. **121**, 13051 (2021).

[23] A. Kudo and Y. Miseki, Chem. Soc. Rev. **38**, 253 (2009).

[24] Y. Guo, H. Li, W. Ma, W. Shi, Y. Zhu, and W. Choi, Carbon Energy **2**, 308 (2020).

[25] Z. Zafar, S. Yi, J. Li, C. Li, Y. Zhu, A. Zada, W. Yao, Z. Liu, and X. Yue, Environ. Mater. **5**, 68 (2022).

[26] C. Dong, C. Lian, S. Hu, Z. Deng, J. Gong, M. Li, H. Liu, M. Xing, and J. Zhang, Nat. Commun. **9**, 1252 (2018).

[27] C. Chen, Y. Kuang, S. Zhu, I. Burgert, T. Keplinger, A. Gong, T. Li, L. Berglund, S. J. Eichhorn, and L. Hu, Nat. Rev. Mater. **5**, 642 (2020).

[28] S. Surnev, A. Fortunelli, and F. P. Netzer, Chem. Rev. **113**, 4314 (2013).

[29] J. C. Tan and A. K. Cheetham, Chem. Soc. Rev. **40**, 1059 (2011).

[30] S. Ling, W. Chen, Y. Fan, K. Zheng, K. Jin, H. Yu, M. J. Buehler, and D. L. Kaplan, Prog. Polym. Sci. **85**, 1 (2018).

[31] S. Shevlin, B. Castro, and X. Li, Nat. Mater. **20**, 727 (2021).

[32] J. K. Nørskov, T. Bligaard, J. Rossmeisl, and C. H. Christensen, Nat. Chem. **1**, 37 (2009).

[33] A. Jain, Y. Shin, and K. A. Persson, Nat. Rev. Mater. **1**, 15004 (2016).

[34] P. Gorai, V. Stevanović, and E. S. Toberer, Nat. Rev. Mater. **2**, 17053 (2017).

[35] S. G. Louie, Y.-H. Chan, F. H. da Jornada, Z. Li, and D. Y. Qiu, Nat. Mater. **20**, 728 (2021).

[36] P. Hohenberg and W. Kohn, Phys. Rev. **136**, B864 (1964).

[37] W. Kohn and L. J. Sham, Phys. Rev. **140**, A1133 (1965).

[38] W. Kohn, Rev. Mod. Phys. **71**, 1253 (1999).

[39] M. Z. Hasan, G. Chang, I. Belopolski, G. Bian, S.-Y. Xu, and J.-X. Yin, Nat. Rev. Mater. **6**, 784 (2021).

[40] B. A. Bernevig, C. Felser, and H. Beidenkopf, Nature **603**, 41 (2022).

[41] Q. Li, C. X. Trang, W. Wu, J. Hwang, D. Cortie, N. Medhekar, S.-K. Mo, S. A. Yang, and M. T. Edmonds, Adv. Mater. **34**, 2107520 (2022).

[42] J. Dong, L. Zhang, X. Dai, F. Ding, and S. O. Valenzuela, Nat. Commun. **11**, 5862 (2020).

[43] M. K. Svendsen, Y. Kurman, P. Schmidt, F. Koppens, I. Kaminer, and K. S. Thygesen, Nat. Commun. **12**, 2778 (2021).

[44] Z. Zhang, X. Yang, K. Liu, and R. Wang, Adv. Sci. **9**, 2105201 (2022).

[45] T. Zhang, X. Xu, B. Huang, Y. Dai, and Y. Ma, npj Comput. Mater. **8**, 64 (2022).

[46] R. Ribeiro-Palau, C. Zhang, K. Watanabe, T. Taniguchi, J. Hone, and C. R. Dean, Science **361**, 690 (2018).

[47] M. V. Stern, Y. Waschitz, W. Cao, I. Nevo, K. Watanabe, T. Taniguchi, E. Sela, M. Urbakh, O. Hod, and M. B. Shalom, Science **372**, 1462 (2021).

[48] J. F. Sierra, J. Fabian, R. K. Kawakami, S. Roche, and S. O. Valenzuela, Nat. Nanotechnol. **16**, 856 (2021).

[49] B. H. Drummond, N. Aizawa, Y. Zhang, W. K. Myers, Y. Xiong, M. W. Cooper, S. Barlow, Q. Gu, L. R. Weiss, A. J. Gillett, D. Credgington, Y.-J. Pu, S. R. Marder, and E. W. Evans, Nat. Commun. **12**, 4532 (2021).

[50] T. Körzdörfer and J.-L. Brédas, Acc. Chem. Res. **47**, 3284 (2014).

[51] B. K. Chang, J.-J. Zhou, N.-E. Lee, and M. Bernardi, npj Comput. Mater. **8**, 63 (2022).

[52] D. Wang, X. Liu, Y. Kang, X. Wang, Y. Wu, S. Fang, H. Yu, M. Memon, H. Zhang, W. Hu, Z. Mi, L. Fu, H. Sun, and S. Long, Nat. Electron **4**, 645 (2021).

[53] H. Matsuo, Y. Noguchi, and M. Miyayama, Nat. Commun. **8**, 207 (2017).

[54] H. Chen, S. Teale, B. Chen, Y. Hou, L. Grater, T. Zhu, K. Bertens, S. M. Park, H. Atapattu, Y. Gao, M. Wei, A. Johnston, Q. Zhou, K. Xu, D. Yu, H. Congcong, T. Cui, E. Jung, C. Zhou, and E. Sargent, Nat. Photon. **16**, 352 (2022).

[55] S. Ha, Y. Lee, Y. Kwak, A. Mishra, E. Yu, E. Yu, B. Ryou, and C.-M. Park, Nat. Commun. **11**, 2509 (2020).

[56] P. Verma, A. Singh, F. A. Rahimi, P. Sarkar, S. Nath, S. K. Pati, and T. K. Maji, Nat. Commun. **12**, 7313 (2021).

[57] M. Pfeffer, C. Müller, E. Kastl, A. Mengele, B. Bagemihl, S. Fauth, J. Habermehl, L. Petermann, M. Wächtler, M. Schulz, D. Chartrand, F. Laverdière, P. Seeber, S. Kupfer, S. Graefe, G. Hanan, J. Vos, B. Dietzek-Ivanšić, and S. Rau, Nat. Chem. **14**, 500– (2022).

[58] X. Song, W. Guangfeng, J. Sun, C. Peng, J. Yin, X. Zhang, Y. Jiang, and H. Fei, Nat. Catal. **3**, 1027 (2020).

[59] F. Xu, K. Meng, B. Cheng, S. Wang, J. Xu, and J. Yu, Nat. Commun. **11**, 4613 (2020).

[60] X. Yang, B. Zhang, Y. Gao, C. Liu, G. Li, B. Rao, D. Chu, N. Yan, M. Zhang, and G. He, Adv. Sci. **9**, 2101652 (2022).

[61] M. Born and R. Oppenheimer, Ann. Phys. **389**, 457 (1927).

[62] D. R. Hartree, Math. Proc. Cambridge Philos. Soc. **24**, 89 (1928).

[63] J. C. Slater, Phys. Rev. **35**, 210 (1930).

[64] V. Fock, Z. Physik **61**, 126 (1930).

[65] T. Koopmans, Physica **1**, 104 (1934).

[66] C. David Sherrill and H. F. Schaefer, *The Configuration Interaction Method: Advances in Highly Correlated Approaches*, edited by P.-O. Löwdin, J. R. Sabin, M. C. Zerner, and E. Brändas, Advances in Quantum Chemistry, Vol. 34 (Academic Press, 1999) pp. 143–269.

[67] C. Møller and M. S. Plesset, Phys. Rev. **46**, 618 (1934).

[68] J. Čížek, J. Chem. Phys. **45**, 4256 (1966).

[69] J. Čižek and J. Paldus, Int. J. Quantum Chem. **5**, 359 (1971).

[70] J. Fosso-Tande, T.-S. Nguyen, G. Gidofalvi, and A. E. DePrince, J. Chem. Theory Comput. **12**, 2260 (2016).

[71] B. O. Roos, P. R. Taylor, and P. E. Sigbahn, Chem. Phys. **48**, 157 (1980).

[72] W. L. McMillan, Phys. Rev. **138**, A442 (1965).

[73] R. M. Martin, L. Reining, and D. M. Ceperley, *Interacting Electrons: Theory and Computational Approaches* (Cambridge University Press, 2016).

[74] D. K. W. Mok, R. Neumann, and N. C. Handy, J. Phys. Chem. **100**, 6225 (1996).

[75] L. H. Thomas, Math. Proc. Cambridge Philos. Soc. **23**, 542 (1927).

[76] E. Fermi, Z. Phys. **48**, 73 (1928).

[77] P. A. M. Dirac, Math. Proc. Cambridge Philos. Soc. **26**, 376 (1930).

[78] R. Taton, Rev. hist. sci. **27**, 3 (1974).

[79] R. P. Feynman, Phys. Rev. **56**, 340 (1939).

[80] E. Engel and R. M. Dreizler, *Density Functional Theory* (Springer, Berlin, 2011).

[81] N. D. Mermin, Phys. Rev. **137**, A1441 (1965).

[82] G. Vignale and M. Rasolt, Phys. Rev. Lett. **59**, 2360 (1987).

[83] J. P. Perdew and K. Schmidt, AIP Conf. Proc. **577**, 1 (2001).

[84] J. C. Slater, Phys. Rev. **81**, 385 (1951).

[85] D. M. Ceperley and B. J. Alder, Phys. Rev. Lett. **45**, 566 (1980).

[86] U. von Barth and L. Hedin, J. Phys. C: Solid State Phys. **5**, 1629 (1972).

[87] S. H. Vosko, L. Wilk, and M. Nusair, Can. J. Phys. **58**, 1200 (1980).

[88] O. Gunnarsson and B. I. Lundqvist, Phys. Rev. B **13**, 4274 (1976).

[89] R. O. Jones and O. Gunnarsson, Rev. Mod. Phys. **61**, 689 (1989).

[90] D. C. Langreth and M. J. Mehl, Phys. Rev. B **28**, 1809 (1983).

[91] A. D. Becke, Phys. Rev. A **38**, 3098 (1988).

[92] J. P. Perdew, J. A. Chevary, S. H. Vosko, K. A. Jackson, M. R. Pederson, D. J. Singh, and C. Fiolhais, Phys. Rev. B **46**, 6671 (1992).

[93] C. Lee, W. Yang, and R. G. Parr, Phys. Rev. B **37**, 785 (1988).

[94] A. D. Becke, Phys. Rev. A **38**, 3098 (1988).

[95] A. D. Becke, J. Chem. Phys. **107**, 8554 (1997).

[96] S. K. Ghosh and R. G. Parr, Phys. Rev. A **34**, 785 (1986).

[97] A. D. Becke and M. R. Roussel, Phys. Rev. A **39**, 3761 (1989).

[98] J. P. Perdew, K. Burke, and M. Ernzerhof, Phys. Rev. Lett. **77**, 3865 (1996).

[99] J. P. Perdew, A. Ruzsinszky, G. I. Csonka, O. A. Vydrov, G. E. Scuseria, L. A. Constantin, X. Zhou, and K. Burke, Phys. Rev. Lett. **100**, 136406 (2008).

[100] F. Bechstedt, *Many-Body Approach to Electronic Excitations: Concepts and Applications* (Springer, Berlin, 2015).

[101] D. A. Liberman, Phys. Rev. B **62**, 6851 (2000).

[102] M. Preuss, W. G. Schmidt, K. Seino, J. Furthmüller, and F. Bechstedt, J. Comput Chem. **25**, 112 (2004).

[103] L. E. Ramos, H.-C. Weissker, J. Furthmüller, and F. Bechstedt, Phys. Stat. Sol. (b) **242**, 3053 (2005).

[104] H.-C. Weissker, J. Furthmüller, and F. Bechstedt, Phys. Rev. Lett. **90**, 085501 (2003).

[105] S. V. Badalov, R. Wilhelm, and W. G. Schmidt, J. Comput Chem. **41**, 1921 (2020).

[106] G. Makov and M. C. Payne, Phys. Rev. B **51**, 4014 (1995).

[107] J. Neugebauer and M. Scheffler, Phys. Rev. B **46**, 16067 (1992).

[108] E. Runge and E. K. U. Gross, Phys. Rev. Lett. **52**, 997 (1984).

[109] M. A. Marques, C. A. Ullrich, F. Nogueira, A. Rubio, K. Burke, and E. K. U. Gross, *Time-Dependent Density Functional Theory*, Lecture Notes in Physics, Vol. 34 (Springer Berlin Heidelberg, 2006) pp. XXXIV,555.

[110] R. van Leeuwen, Phys. Rev. Lett. **82**, 3863 (1999).

[111] E. K. U. Gross, J. F. Dobson, and M. Petersilka (Springer Berlin Heidelberg, 1996) pp. 81–172.

[112] F. A. Parpia and W. R. Johnson, J. Phys. B: Atom. Mol. Phys. **17**, 531 (1984).

[113] A. K. Rajagopal, Phys. Rev. A **50**, 3759 (1994).

[114] T. K. Ng and K. S. Singwi, Phys. Rev. Lett. **59**, 2627 (1987).

[115] W. Yang, Phys. Rev. A **38**, 5512 (1988).

[116] S. Botti, A. Schindlmayr, R. D. Sole, and L. Reining, Rep. Prog. Phys. **70**, 357 (2007).

[117] S. L. Adler, Phys. Rev. **126**, 413 (1962).

[118] N. Wiser, Phys. Rev. **129**, 62 (1963).

[119] G. Onida, L. Reining, and A. Rubio, Rev. Mod. Phys. **74**, 601 (2002).

[120] A. J. Cohen, P. Mori-Sánchez, and W. Yang, Science **321**, 792 (2008).

[121] A. J. Cohen, P. Mori-Sánchez, and W. Yang, Chem. Rev. **112**, 289 (2012).

[122] M. S. Hybertsen and S. G. Louie, Phys. Rev. B **34**, 5390 (1986).

[123] J. Lindhard, K. Dan. Vidensk. Selsk. Mat.-Fys. Medd. **28**, 1 (1954).

[124] E. K. U. Gross and W. Kohn, Phys. Rev. Lett. **55**, 2850 (1985).

[125] E. K. U. Gross and W. Kohn, Phys. Rev. Lett. **57**, 923 (1986).

[126] G. Kresse and J. Furthmüller, Phys. Rev. B **54**, 11169 (1996).

[127] P. Giannozzi, S. Baroni, N. Bonini, M. Calandra, R. Car, C. Cavazzoni, D. Ceresoli, G. L. Chiarotti, M. Cococcioni, I. Dabo, A. D. Corso, S. de Gironcoli, S. Fabris, G. Fratesi, R. Gebauer, U. Gerstmann, C. Gougoussis, A. Kokalj, M. Lazzeri, L. Martin-Samos, N. Marzari, F. Mauri, R. Mazzarello, S. Paolini, A. Pasquarello, L. Paulatto, C. Sbraccia, S. Scandolo, G. Sclauzero, A. P. Seitsonen, A. Smogunov, P. Umari, and R. M. Wentzcovitch, J. Phys. Condens. Matter **21**, 395502 (2009).

[128] P. Giannozzi, O. Andreussi, T. Brumme, O. Bunau, M. B. Nardelli, M. Calandra, R. Car, C. Cavazzoni, D. Ceresoli, M. Cococcioni, N. Colonna, I. Carnimeo, A. D. Corso, S. de Gironcoli, P. Delugas, R. A. DiStasio, A. Ferretti, A. Floris, G. Fratesi, G. Fugallo, R. Gebauer, U. Gerstmann, F. Giustino, T. Gorni, J. Jia, M. Kawamura, H.-Y. Ko, A. Kokalj, E. Küçükbenli, M. Lazzeri, M. Marsili, N. Marzari, F. Mauri, N. L. Nguyen, H.-V. Nguyen, A. O. de-la Roza, L. Paulatto, S. Poncé, D. Rocca, R. Sabatini, B. Santra, M. Schlipf, A. P. Seitsonen, A. Smogunov, I. Timrov, T. Thonhauser, P. Umari, N. Vast, X. Wu, and S. Baroni, J. Phys. Condens. Matter **29**, 465901 (2017).

[129] F. Neese, WIREs Comput. Mol. Sci. **8**, e1327 (2018).

[130] J. C. Slater, Phys. Rev. **36**, 57 (1930).

[131] I. Cacelli, R. Moccia, and A. Rizzo, Phys. Rev. A **57**, 1895 (1998).

[132] E. Hückel, Z. Physik **70**, 204 (1931).

[133] R. S. Mulliken, Science **157**, 13 (1967).

[134] O. K. Andersen, Phys. Rev. B **12**, 3060 (1975).

[135] S. Y. Savrasov, Phys. Rev. B **54**, 16470 (1996).

[136] G. Gandus, A. Valli, D. Passerone, and R. Stadler, J. Chem. Phys. **153**, 194103 (2020).

[137] S. Baroni, S. de Gironcoli, A. Dal Corso, and P. Giannozzi, Rev. Mod. Phys. **73**, 515 (2001).

[138] M. Weinert, E. Wimmer, and A. J. Freeman, Phys. Rev. B **26**, 4571 (1982).

[139] P. E. Blöchl, Phys. Rev. B **50**, 17953 (1994).

[140] S. Lehtola, Int. J. Quantum. Chem. **119**, e25968 (2019).

[141] F. Weigend and R. Ahlrichs, Phys. Chem. Chem. Phys. **7**, 3297 (2005).

[142] F. Bloch, Z. Physik **52**, 555 (1929).

[143] P. Pulay, Mol. Phys. **17**, 197 (1969).

[144] A. Baldereschi, Phys. Rev. B **7**, 5212 (1973).

[145] D. J. Chadi and M. L. Cohen, Phys. Rev. B **8**, 5747 (1973).

[146] H. J. Monkhorst and J. D. Pack, Phys. Rev. B **13**, 5188 (1976).

[147] W. E. Pickett, Comput. Phys. Rep. **9**, 115 (1989).

[148] M. C. Payne, M. P. Teter, D. C. Allan, T. A. Arias, and J. D. Joannopoulos, Rev. Mod. Phys. **64**, 1045 (1992).

[149] R. M. Martin, *Electronic Structure: Basic Theory and Practical Methods* (Cambridge Univ. Press, 2004).

[150] D. R. Hamann, M. Schlüter, and C. Chiang, Phys. Rev. Lett. **43**, 1494 (1979).

[151] D. Vanderbilt, Phys. Rev. B **41**, 7892 (1990).

[152] G. Kresse and D. Joubert, Phys. Rev. B **59**, 1758 (1999).

[153] G. B. Bachelet, D. R. Hamann, and M. Schlüter, Phys. Rev. B **26**, 4199 (1982).

[154] L. Kleinman, Phys. Rev. B **21**, 2630 (1980).

[155] G. B. Bachelet, D. R. Hamann, and M. Schlüter, Phys. Rev. B **26**, 4199 (1982).

[156] L. Kleinman and D. M. Bylander, Phys. Rev. Lett. **48**, 1425 (1982).

[157] L. A. Hemstreet, C. Y. Fong, and J. S. Nelson, Phys. Rev. B **47**, 4238 (1993).

[158] T. Bučko, J. Hafner, S. Lebègue, and J. G. Ángyán, J. Phys. Chem. A **114**, 11814 (2010).

[159] F. London, Z. Physik **63**, 245 (1930).

[160] K. Berland, V. R. Cooper, K. Lee, E. Schröder, T. Thonhauser, P. Hyldgaard, and B. I. Lundqvist, Rep. Prog. Phys. **78**, 066501 (2015).

[161] M. Dubecký, L. Mitas, and P. Jurečka, Chem. Rev. **116**, 5188 (2016).

[162] J. Toulouse, I. C. Gerber, G. Jansen, A. Savin, and J. G. Ángyán, Phys. Rev. Lett. **102**, 096404 (2009).

[163] T. Bučko, J. Hafner, S. Lebègue, and J. G. Ángyán, J. Phys. Chem. A **114**, 11814 (2010).

[164] J. F. Dobson and B. P. Dinte, Phys. Rev. Lett. **76**, 1780 (1996).

[165] Y. Andersson, D. C. Langreth, and B. I. Lundqvist, Phys. Rev. Lett. **76**, 102 (1996).

[166] W. Kohn, Y. Meir, and D. E. Makarov, Phys. Rev. Lett. **80**, 4153 (1998).

[167] S. Grimme, S. Ehrlich, and L. Goerigk, J. Comput. Chem. **32**, 1456 (2011).

[168] M. Dion, H. Rydberg, E. Schröder, D. C. Langreth, and B. I. Lundqvist, Phys. Rev. Lett. **92**, 246401 (2004).

[169] H. Rydberg, M. Dion, N. Jacobson, E. Schröder, P. Hyldgaard, S. I. Simak, D. C. Langreth, and B. I. Lundqvist, Phys. Rev. Lett. **91**, 126402 (2003).

[170] S. Grimme, J. Comput. Chem. **25**, 1463 (2004).

[171] F. Ortmann, F. Bechstedt, and W. G. Schmidt, Phys. Rev. B **73**, 205101 (2006).

[172] F. Ortmann, W. G. Schmidt, and F. Bechstedt, Phys. Rev. Lett. **95**, 186101 (2005).

[173] W. Schmidt, K. Seino, M. Preuss, A. Hermann, F. Ortmann, and F. Bechstedt, Appl. Phys. A **85**, 387 (2006).

[174] M. Rohlfing and T. Bredow, Phys. Rev. Lett. **101**, 266106 (2008).

[175] N. Atodiresei, V. Caciuc, P. Lazić, and S. Blügel, Phys. Rev. Lett. **102**, 136809 (2009).

[176] S. Grimme, J. Comput. Chem. **27**, 1787 (2006).

[177] W. Kohn, Y. Meir, and D. E. Makarov, Phys. Rev. Lett. **80**, 4153 (1998).

[178] J. F. Dobson and B. P. Dinte, Phys. Rev. Lett. **76**, 1780 (1996).

[179] M. Lein, J. F. Dobson, and E. K. U. Gross, J. Comput. Chem. **20**, 12 (1999).

[180] E. R. Johnson and A. D. Becke, J. Chem. Phys. **124**, 174104 (2006).

[181] M. Hasegawa and K. Nishidate, Phys. Rev. B **70**, 205431 (2004).

[182] S. Grimme, J. Antony, S. Ehrlich, and H. Krieg, J. Chem. Phys. **132**, 154104 (2010).

[183] M. Cococcioni and S. de Gironcoli, Phys. Rev. B **71**, 035105 (2005).

[184] L. Kronik and S. Kümmel, Phys. Chem. Chem. Phys. **22**, 16467 (2020).

[185] J. P. Perdew and A. Zunger, Phys. Rev. B **23**, 5048 (1981).

[186] A. J. Cohen, P. Mori-Sánchez, and W. Yang, Science **321**, 792 (2008).

[187] X. Zheng, M. Liu, E. R. Johnson, J. Contreras-García, and W. Yang, J. Chem. Phys. **137**, 214106 (2012).

[188] M.-C. Kim, E. Sim, and K. Burke, Phys. Rev. Lett. **111**, 073003 (2013).

[189] E. R. Johnson, A. Otero-de-la Roza, and S. G. Dale, J. Chem. Phys. **139**, 184116 (2013).

[190] J. P. Perdew, R. G. Parr, M. Levy, and J. L. Balduz, Phys. Rev. Lett. **49**, 1691 (1982).

[191] J. P. Perdew and M. Levy, Phys. Rev. Lett. **51**, 1884 (1983).

[192] L. J. Sham and M. Schlüter, Phys. Rev. Lett. **51**, 1888 (1983).

[193] E. Sagvolden and J. P. Perdew, Phys. Rev. A **77**, 012517 (2008).

[194] P. Mori-Sánchez, A. J. Cohen, and W. Yang, J. Chem. Phys. **125**, 201102 (2006).

[195] O. A. Vydrov, G. E. Scuseria, and J. P. Perdew, J. Chem. Phys. **126**, 154109 (2007).

[196] P. Mori-Sánchez, A. J. Cohen, and W. Yang, Phys. Rev. Lett. **100**, 146401 (2008).

[197] J. P. Perdew and M. Levy, Phys. Rev. Lett. **51**, 1884 (1983).

[198] T. Bally and G. N. Sastry, J. Phys. Chem. A **101**, 7923 (1997).

[199] A. Ruzsinszky, J. P. Perdew, G. I. Csonka, O. A. Vydrov, and G. E. Scuseria, J. Chem. Phys. **126**, 104102 (2007).

[200] M. J. G. Peach, A. M. Teale, T. Helgaker, and D. J. Tozer, J. Chem. Theory Comput **11**, 5262 (2015).

[201] I. G. Austin and N. F. Mott, Science **168**, 71 (1970).

[202] J. Hubbard, Proc. Roy. Soc. Lond. A **276**, 238 (1963).

[203] D. D. O'Regan, N. D. M. Hine, M. C. Payne, and A. A. Mostofi, Phys. Rev. B **85**, 085107 (2012).

[204] V. I. Anisimov and O. Gunnarsson, Phys. Rev. B **43**, 7570 (1991).

[205] V. I. Anisimov, J. Zaanen, and O. K. Andersen, Phys. Rev. B **44**, 943 (1991).

[206] V. I. Anisimov, I. V. Solovyev, M. A. Korotin, M. T. Czyżyk, and G. A. Sawatzky, Phys. Rev. B **48**, 16929 (1993).

[207] I. V. Solovyev, P. H. Dederichs, and V. I. Anisimov, Phys. Rev. B **50**, 16861 (1994).

[208] A. I. Liechtenstein, V. I. Anisimov, and J. Zaanen, Phys. Rev. B **52**, R5467 (1995).

[209] W. E. Pickett, S. C. Erwin, and E. C. Ethridge, Phys. Rev. B **58**, 1201 (1998).

[210] S. L. Dudarev, G. A. Botton, S. Y. Savrasov, C. J. Humphreys, and A. P. Sutton, Phys. Rev. B **57**, 1505 (1998).

[211] T. R. Paudel and W. R. L. Lambrecht, Phys. Rev. B **77**, 205202 (2008).

[212] M. J. Han, T. Ozaki, and J. Yu, Phys. Rev. B **73**, 045110 (2006).

[213] H. Hsu, K. Umemoto, M. Cococcioni, and R. Wentzcovitch, Phys. Rev. B **79**, 125124 (2009).

[214] H. Hsu, P. Blaha, M. Cococcioni, and R. M. Wentzcovitch, Phys. Rev. Lett. **106**, 118501 (2011).

[215] F. Zhou, C. A. Marianetti, M. Cococcioni, D. Morgan, and G. Ceder, Phys. Rev. B **69**, 201101 (2004).

[216] V. L. C. Jr and M. Cococcioni, J. Phys. Condens. Matter **22**, 055602 (2010).

[217] I. Timrov, N. Marzari, and M. Cococcioni, Phys. Rev. B **103**, 045141 (2021).

[218] A. D. Becke, J. Chem. Phys. **98**, 1372 (1993).

[219] J. P. Perdew, M. Ernzerhof, and K. Burke, J. Chem. Phys. **105**, 9982 (1996).

[220] A. D. Becke, J. Chem. Phys. **98**, 5648 (1993).

[221] P. J. Stephens, F. J. Devlin, C. F. Chabalowski, and M. J. Frisch, J. Phys. Chem. **98**, 11623 (1994).

[222] C. Adamo and V. Barone, J. Chem. Phys. **110**, 6158 (1999).

[223] M. Ernzerhof and G. E. Scuseria, J. Chem. Phys. **110**, 5029 (1999).

[224] S. Kossmann, B. Kirchner, and F. Neese, Molecular Physics **105**, 2049 (2007).

[225] T. Leininger, H. Stoll, H.-J. Werner, and A. Savin, Chem. Phys. Lett. **275**, 151 (1997).

[226] R. Baer and D. Neuhauser, Phys. Rev. Lett. **94**, 043002 (2005).

[227] O. A. Vydrov and G. E. Scuseria, J. Chem. Phys. **125**, 234109 (2006).

[228] O. A. Vydrov, J. Heyd, A. V. Krukau, and G. E. Scuseria, J. Chem. Phys. **125**, 074106 (2006).

[229] J. Heyd, G. E. Scuseria, and M. Ernzerhof, J. Chem. Phys. **118**, 8207 (2003).

[230] A. V. Krukau, O. A. Vydrov, A. F. Izmaylov, and G. E. Scuseria, J. Chem. Phys. **125**, 224106 (2006).

[231] J. Heyd and G. E. Scuseria, J. Chem. Phys. **120**, 7274 (2004).

[232] J. Heyd and G. E. Scuseria, J. Chem. Phys. **121**, 1187 (2004).

[233] M. Li, J. R. Reimers, M. J. Ford, R. Kobayashi, and R. D. Amos, J. Chem. Phys. **42**, 1486 (2021).

[234] T. Yanai, D. P. Tew, and N. C. Handy, Chem. Phys. Lett. **393**, 51 (2004).

[235] J.-D. Chai and M. Head-Gordon, J. Chem. Phys. **128**, 084106 (2008).

[236] Y. Tawada, T. Tsuneda, S. Yanagisawa, T. Yanai, and K. Hirao, J. Chem. Phys. **120**, 8425 (2004).

[237] P. Dev, S. Agrawal, and N. J. English, J. Chem. Phys. **136**, 224301 (2012).

[238] J. Sun, C.-W. Lee, A. Kononov, A. Schleife, and C. A. Ullrich, Phys. Rev. Lett. **127**, 077401 (2021).

[239] M. Casanova-Páez and L. Goerigk, J. Chem. Theory Comput. **17**, 5165 (2021).

[240] M. Casanova-Páez and L. Goerigk, J. Chem. Phys. **153**, 064106 (2020).

[241] F. A. Grant, Rev. Mod. Phys. **31**, 646 (1959).

[242] R. G. Breckenridge and W. R. Hosler, Phys. Rev. **91**, 793 (1953).

[243] M. Fujihira, Y. Satoh, and T. Osa, Nature **293**, 206 (1981).

[244] J. Schneider, M. Matsuoka, M. Takeuchi, J. Zhang, Y. Horiuchi, M. Anpo, and D. W. Bahnemann, Chem. Rev. **114**, 9919 (2014).

[245] M. R. Hoffmann, S. T. Martin, W. Choi, and D. W. Bahnemann, Chem. Rev. **95**, 69 (1995).

[246] S. U. M. Khan, M. Al-Shahry, and W. B. Ingler, Jr., Science **297**, 2243 (2002).

[247] E. Wahlström, E. K. Vestergaard, R. Schaub, A. Rønnau, M. Vestergaard, E. Lægsgaard, I. Stensgaard, and F. Besenbacher, Science **303**, 511 (2004).

[248] S. Wang, L. Pan, J.-J. Song, W. Mi, J.-J. Zou, L. Wang, and X. Zhang, J. Am. Chem. Soc. **137**, 2975 (2015).

[249] R. Asahi, T. Morikawa, T. Ohwaki, K. Aoki, and Y. Taga, Science **293**, 269 (2001).

[250] U. Bach, D. Lupo, P. Comte, J. E. Moser, F. Weissörtel, J. Salbeck, H. Spreitzer, and M. Grätzel, Nature **395**, 583 (1998).

[251] N.-G. Park, G. Schlichthörl, J. van de Lagemaat, H. M. Cheong, A. Mascarenhas, and A. J. Frank, J. Phys. Chem. B **103**, 3308 (1999).

[252] J. J. Yang, M. D. Pickett, X. Li, D. A. A. Ohlberg, D. R. Stewart, and R. S. Williams, Nat. Nanotechnol. **3**, 429 (2008).

[253] D.-H. Kwon, K. M. Kim, J. H. Jang, J. M. Jeon, M. H. Lee, G. H. Kim, X.-S. Li, G.-S. Park, B. Lee, S. Han, M. Kim, and C. S. Hwang, Nat. Nanotechnol. **5**, 148 (2009).

[254] H. Y. Jeong, J. Y. Lee, and S.-Y. Choi, Adv. Funct. Mater. **20**, 3912 (2010).

[255] S.-D. Mo and W. Y. Ching, Phys. Rev. B **51**, 13023 (1995).

[256] D. Dambournet, I. Belharouak, and K. Amine, Chem. Mater. **22**, 1173 (2010).

[257] M. Landmann, E. Rauls, and W. G. Schmidt, J. Phys. Condens. Matter **24**, 195503 (2012).

[258] T. Zhu and S.-P. Gao, J. Phys. Chem. C **118**, 11385 (2014).

[259] Y. Tezuka, S. Shin, T. Ishii, T. Ejima, S. Suzuki, and S. Sato, J. Phys. Soc. Jpn. **63**, 347 (1994).

[260] E. Baldini, L. Chiodo, A. Dominguez, M. Palummo, S. Moser, M. Yazdi-Rizi, G. Auböck, B. Mallett, H. Berger, A. Magrez, C. Bernhard, M. Grioni, A. Rubio, and M. Chergui, Nat. Commun. **8**, 13 (2017).

[261] G. Xiong, R. Shao, T. Droubay, A. Joly, K. Beck, S. Chambers, and W. Hess, Adv. Funct. Mater. **17**, 2133 (2007).

[262] J. Pascual, J. Camassel, and H. Mathieu, Phys. Rev. B **18**, 5606 (1978).

[263] A. Amtout and R. Leonelli, Phys. Rev. B **51**, 6842 (1995).

[264] D. Reyes-Coronado, G. Rodríguez-Gattorno, M. E. Espinosa-Pesqueira, C. Cab, R. de Coss, and G. Oskam, Nanotechnology **19**, 145605 (2008).

[265] L. Kavan, M. Grätzel, S. E. Gilbert, C. Klemenz, and H. J. Scheel, J. Am. Chem. Soc. **118**, 6716 (1996).

[266] H. Tang, F. Lévy, H. Berger, and P. E. Schmid, Phys. Rev. B **52**, 7771 (1995).

[267] D.-H. Kim, W.-S. Kim, S. Kim, and S.-H. Hong, ACS Appl. Mater. Interfaces **6**, 11817 (2014).

[268] A. Mattsson and L. Österlund, J. Phys. Chem. C **114**, 14121 (2010).

[269] S. Selcuk and A. Selloni, Nat. Mater. **15**, 1107 (2016).

[270] R. Rousseau, V.-A. Glezakou, and A. Selloni, Nat. Rev. Mater. **5**, 460 (2020).

[271] T. A. Pham, Y. Ping, and G. Galli, Nat. Mater. **16**, 401 (2017).

[272] B.-H. Lee, S. Park, M. Kim, A. K. Sinha, S. C. Lee, E. Jung, W. J. Chang, K.-S. Lee, J. H. Kim, S.-P. Cho, H. Kim, K. T. Nam, and T. Hyeon, Nat. Mater. **18**, 620 (2019).

[273] J. Greeley, T. F. Jaramillo, J. Bonde, I. Chorkendorff, and J. K. Nørskov, Nat. Mater. **5**, 909 (2006).

[274] I. E. Castelli, F. Hüser, M. Pandey, H. Li, K. S. Thygesen, B. Seger, A. Jain, K. A. Persson, G. Ceder, and K. W. Jacobsen, Adv. Energy Mater. **5**, 1400915 (2015).

[275] C. David, Materials (Basel) **12**, 1332 (2019).

[276] S. Selcuk, X. Zhao, and A. Selloni, Nat. Mater. **17**, 923 (2018).

[277] A. Georges, G. Kotliar, W. Krauth, and M. J. Rozenberg, Rev. Mod. Phys. **68**, 13 (1996).

[278] G. Kotliar, S. Y. Savrasov, K. Haule, V. S. Oudovenko, O. Parcollet, and C. A. Marianetti, Rev. Mod. Phys. **78**, 865 (2006).

[279] Z. Hu and H. Metiu, J. Phys. Chem. C **115**, 5841 (2011).

[280] L. A. Agapito, S. Curtarolo, and M. Buongiorno Nardelli, Phys. Rev. X **5**, 011006 (2015).

[281] M. T. Curnan and J. R. Kitchin, J. Phys. Chem. C **119**, 21060 (2015).

[282] M. Samat, A. Ali, M. Taib, O. Hassan, and M. Yahya, Results Phys. **6**, 891 (2016).

[283] J. Li, S. Meng, L. Qin, and H. Lu, Chin. Phys. B **26**, 087101 (2017).

[284] J. J. Brown and A. J. Page, J. Chem. Phys. **153**, 224116 (2020).

[285] E. Finazzi, C. Di Valentin, G. Pacchioni, and A. Selloni, J. Chem. Phys. **129**, 154113 (2008).

[286] G. Mattioli, P. Alippi, F. Filippone, R. Caminiti, and A. Amore Bonapasta, J. Phys. Chem. C **114**, 21694 (2010).

[287] S.-H. Lee and Y.-W. Son, Phys. Rev. Research **2**, 043410 (2020).

[288] C. E. Patrick and F. Giustino, J. Phys. Condens. Matter **24**, 202201 (2012).

[289] C. Persson and A. Ferreira da Silva, Appl. Phys. Lett. **86**, 231912 (2005).

[290] O. K. Orhan and D. D. O'Regan, Phys. Rev. B **101**, 245137 (2020).

[291] N. E. Kirchner-Hall, W. Zhao, Y. Xiong, I. Timrov, and I. Dabo, Appl. Sci. **11**, 2395 (2021).

[292] G. Mattioli, F. Filippone, P. Alippi, and A. Amore Bonapasta, Phys. Rev. B **78**, 241201 (2008).

[293] M. Gerosa, C. E. Bottani, L. Caramella, G. Onida, C. Di Valentin, and G. Pacchioni, Phys. Rev. B **91**, 155201 (2015).

[294] J. Muscat, A. Wander, and N. Harrison, Chem. Phys. Lett **342**, 397 (2001).

[295] P. Deák, B. Aradi, and T. Frauenheim, Phys. Rev. B **86**, 195206 (2012).

[296] A. Janotti, J. B. Varley, P. Rinke, N. Umezawa, G. Kresse, and C. G. Van de Walle, Phys. Rev. B **81**, 085212 (2010).

[297] M. Lazzeri, A. Vittadini, and A. Selloni, Phys. Rev. B **63**, 155409 (2001).

[298] K. C. Ko, O. Lamiel-Garcıa, J. Y. Lee, and F. Illas, Phys. Chem. Chem. Phys. **18**, 12357 (2016).

[299] F. Viñes, O. Lamiel-García, K. Chul Ko, J. Yong Lee, and F. Illas, J. Comput. Chem **38**, 781 (2017).

[300] P. Basera, S. Saini, and S. Bhattacharya, J. Mater. Chem. C **7**, 14284 (2019).

[301] K. Yu and E. A. Carter, J. Chem. Phys. **140**, 121105 (2014).

[302] H. Zhang and J. F. Banfield, J. Phys. Chem. B **104**, 3481 (2000).

[303] Y. Wang, L. Li, X. Huang, Q. Li, and G. Li, RSC Adv. **5**, 34302 (2015).

[304] J. K. Burdett, T. Hughbanks, G. J. Miller, J. W. Richardson, and J. V. Smith, J. Am. Chem. Soc. **109**, 3639 (1987).

[305] M. Horn and C. Schwerdtfeger, Z. Krystallog. **136**, 273 (1972).

[306] M. A. Reddy, M. S. Kishore, V. Pralong, U. V. Varadaraju, and B. Raveau, Electrochem. Solid-State Lett. **10**, A29 (2007).

[307] D. T. Cromer and K. Herrington, J. Am. Chem. Soc. **77**, 4708 (1955).

[308] W. H. Baur, Acta Cryst. **14**, 214 (1961).

[309] J. C. Woicik, E. J. Nelson, L. Kronik, M. Jain, J. R. Chelikowsky, D. Heskett, L. E. Berman, and G. S. Herman, Phys. Rev. Lett. **89**, 077401 (2002).

[310] S. Hüfner and G. K. Wertheim, Phys. Rev. B **8**, 4857 (1973).

[311] Z. Zhang, S.-P. Jeng, and V. E. Henrich, Phys. Rev. B **43**, 12004 (1991).

[312] R. H. Tait and R. V. Kasowski, Phys. Rev. B **20**, 5178 (1979).

[313] R. Sanjinés, H. Tang, H. Berger, F. Gozzo, G. Margaritondo, and F. Lèvy, J. Appl. Phys. **75**, 2945 (1994).

[314] Y.-f. Zhang, W. Lin, Y. Li, K.-n. Ding, and J.-q. Li, J. Phys. Chem. B **109**, 19270 (2005).

[315] A. Janotti, J. B. Varley, P. Rinke, N. Umezawa, G. Kresse, and C. G. Van de Walle, Phys. Rev. B **81**, 085212 (2010).

[316] T. E. Tiwald and M. Schubert, Proc. SPIE **4103**, 19 (2000).

[317] N. Hosaka, T. Sekiya, C. Satoko, and S. Kurita, J. Phys. Soc. Jpn **66**, 877 (1997).

[318] N. Tiwale, A. Subramanian, Z. Dai, S. Sikder, J. T. Sadowski, and C.-Y. Nam, Commun. Mater **1**, 94 (2020).

[319] M. Fukuhara, T. Kuroda, and F. Hasegawa, Sci. Rep. **6**, 35870 (2016).

[320] L. S. Hsu, R. Rujkorakarn, J. R. Sites, and C. Y. She, J. Appl. Phys. **59**, 3475 (1986).

[321] D. Reyes-Coronado, G. Rodríguez-Gattorno, M. E. Espinosa-Pesqueira, C. Cab, R. de Coss, and G. Oskam, Nanotechnology **19**, 145605 (2008).

[322] H. Zhang, B. Chen, J. F. Banfield, and G. A. Waychunas, Phys. Rev. B **78**, 214106 (2008).

[323] X. Chen and S. S. Mao, Chem. Rev. **107**, 2891 (2007).

[324] M. L. Grilli, M. Yilmaz, S. Aydogan, and B. B. Cirak, Ceram. Int. **44**, 11582 (2018).

[325] O. Durante, C. Di Giorgio, V. Granata, J. Neilson, R. Fittipaldi, A. Vecchione, G. Carapella, F. Chiadini, R. DeSalvo, F. Dinelli, V. Fiumara, V. Pierro, I. M. Pinto, M. Principe, and F. Bobba, Nanomaterials **11** (2021), 10.3390/nano11061409.

[326] O. M. Ylivaara, A. Langner, X. Liu, D. Schneider, J. Julin, K. Arstila, S. Sintonen, S. Ali, H. Lipsanen, T. Sajavaara, S.-P. Hannula, and R. L. Puurunen, Thin Solid Films **732**, 138758 (2021).

[327] K. Eufinger, D. Poelman, H. Poelman, R. De Gryse, and G. Marin, Appl. Surf. Sci. **254**, 148 (2007).

[328] M. Zhang, G. Lin, C. Dong, and L. Wen, Surf. Coat. Technol. **201**, 7252 (2007).

[329] J. Saari, H. Ali-Löytty, K. Lahtonen, M. Hannula, L. Palmolahti, A. Tukiainen, and M. Valden, J. Phys. Chem. C **126**, 15357 (2022).

[330] D. Yan, M. Topsakal, S. Selcuk, J. L. Lyons, W. Zhang, Q. Wu, I. Waluyo, E. Stavitski, K. Attenkofer, S. Yoo, M. S. Hybertsen, D. Lu, D. J. Stacchiola, and M. Liu, Nano Lett. **19**, 3457 (2019).

[331] V. Van Hoang, Phys. Status Solidi B **244**, 1280 (2007).

[332] L. B. Reutergådh and M. Iangphasuk, Chemosphere **35**, 585 (1997).

[333] Z. Wang and X. Lang, Appl. Catal. B Environ. **224**, 404 (2018).

[334] M. J. Abeledo-Lameiro, A. Reboredo-Fernández, M. I. Polo-López, P. Fernández-Ibáñez, E. Ares-Mazás, and H. Gómez-Couso, Catal. Today **280**, 132 (2017).

[335] E. A. Serna-Galvis, J. Silva-Agredo, A. L. Giraldo, O. A. Flórez-Acosta, and R. A. Torres-Palma, Sci. Total Environ. **541**, 1431 (2016).

[336] Y. He, N. B. Sutton, H. H. H. Rijnaarts, and A. A. M. Langenhoff, Appl. Catal. B Environ. **182**, 132 (2016).

[337] K. Sornalingam, A. McDonagh, J. L. Zhou, M. A. H. Johir, and M. B. Ahmed, Sci. Total Environ. **610–611**, 521 (2018).

[338] G. Rothenberger, J. Moser, M. Graetzel, N. Serpone, and D. K. Sharma, J. Am. Chem. Soc. **107**, 8054 (1985).

[339] K. S. Novoselov, A. K. Geim, S. V. Morozov, D. Jiang, Y. Zhang, S. V. Dubonos, I. V. Grigorieva, and A. A. Firsov, Science **306**, 666 (2004).

[340] A. K. Geim and K. S. Novoselov, Nat. Mater. **6**, 183 (2007).

[341] A. K. Geim, Science **324**, 1530 (2009).

[342] Q. Bao and K. P. Loh, ACS Nano **6**, 3677 (2012).

[343] B. O'Regan and M. Grätzel, Nature **353**, 737 (1991).

[344] X. Fu, W. A. Zeltner, and M. A. Anderson, Appl. Catal. B Environ. **6**, 209 (1995).

[345] J. M. Jung, M. Wang, E. J. Kim, C. Park, and S. H. Hahn, Appl. Catal. B Environ. **84**, 389 (2008).

[346] S. Sakthivel and H. Kisch, Angew. Chem. Int. Ed. **42**, 4908 (2003).

[347] Y. Gai, J. Li, S.-S. Li, J.-B. Xia, and S.-H. Wei, Phys. Rev. Lett. **102**, 036402 (2009).

[348] O. V. Makarova, T. Rajh, M. C. Thurnauer, A. Martin, P. A. Kemme, and D. Cropek, Environ. Sci. Technol. **34**, 4797 (2000).

[349] I. Beinik, A. Bruix, Z. Li, K. C. Adamsen, S. Koust, B. Hammer, S. Wendt, and J. V. Lauritsen, Phys. Rev. Lett. **121**, 206003 (2018).

[350] D. B. Warheit and S. C. Brown, Toxicol. Lett. **302**, 42 (2019).

[351] N. Xu, Z. Shi, Y. Fan, J. Dong, J. Shi, and M. Z.-C. Hu, Ind. Eng. Chem. Res. **38**, 373 (1999).

[352] C. Yu, J. C. Yu, and M. Chan, J. Solid State Chem. **182**, 1061 (2009).

[353] S. Hwang, M. C. Lee, and W. Choi, Appl. Catal. B Environ. **46**, 49 (2003).

[354] K. Naoi, Y. Ohko, and T. Tatsuma, J. Am. Chem. Soc. **126**, 3664 (2004).

[355] B. Tryba, A. Morawski, and M. Inagaki, Appl. Catal. B Environ. **41**, 427 (2003).

[356] W. Wang, P. Serp, P. Kalck, and J. L. Faria, Appl. Catal. B Environ. **56**, 305 (2005).

[357] F. Loske and A. Kühnle, Appl. Phys. Lett. **95**, 043110 (2009).

[358] H. Zhang, X. Lv, Y. Li, Y. Wang, and J. Li, ACS Nano **4**, 380 (2010).

[359] Y. Zhang, Z.-R. Tang, X. Fu, and Y.-J. Xu, ACS Nano **4**, 7303 (2010).

[360] J. Yu, T. Ma, G. Liu, and B. Cheng, Dalton Trans. **40**, 6635 (2011).

[361] W.-J. Ong, M. M. Gui, S.-P. Chai, and A. R. Mohamed, RSC Adv. **3**, 4505 (2013).

[362] H. Adamu, P. Dubey, and J. A. Anderson, Chem. Eng. J. **284**, 380 (2016).

[363] Q. Xiang, B. Cheng, and J. Yu, Angew. Chem. Int. Ed. **54**, 11350 (2015).

[364] X. Wan, Y. Huang, and Y. Chen, Acc. Chem. Res. **45**, 598 (2012).

[365] X. Huang, X. Qi, F. Boey, and H. Zhang, Chem. Soc. Rev. **41**, 666 (2012).

[366] M.-Q. Yang, N. Zhang, M. Pagliaro, and Y.-J. Xu, Chem. Soc. Rev. **43**, 8240 (2014).

[367] S. Y. Lim, W. Shen, and Z. Gao, Chem. Soc. Rev. **44**, 362 (2015).

[368] N. Zhang, S. Yang, Min-Quan amd Liu, Y. Sun, and Y.-J. Xu, Chem. Rev. **115**, 10307 (2015).

[369] L.-W. Zhang, H.-B. Fu, and Y.-F. Zhu, Adv. Funct. Mater. **18**, 2180 (2008).

[370] N. S. McIntyre, K. R. Thompson, and W. Weltner Jr, J. Phys. Chem. **75**, 3243 (1971).

[371] H. Wu and L.-S. Wang, J. Chem. Phys. **107**, 8221 (1997).

[372] H.-J. Zhai and L.-S. Wang, J. Am. Chem. Soc. **129**, 3022 (2007).

[373] D. L. Hildenbrand, Chem. Phys. Lett. **44**, 281 (1976).

[374] G. Balducci, G. Gigli, and M. Guido, J. Chem. Phys. **83**, 1913 (1985).

[375] Z.-W. Qu and G.-J. Kroes, J. Phys. Chem. B **110**, 8998 (2006).

[376] N. Marom, M. Kim, and J. R. Chelikowsky, Phys. Rev. Lett. **108**, 106801 (2012).

[377] D. Çakır and O. Gülseren, J. Phys.: Condens. Matter **24**, 305301 (2012).

[378] S. M. Woodley, S. Hamad, J. A. Mejías, and C. R. A. Catlow, J. Mater. Chem. **16**, 1927 (2006).

[379] M. I. Rojas and E. P. M. Leiva, Phys. Rev. B **76**, 155415 (2007).

[380] W. Geng, H. Liu, and X. Yao, Phys. Chem. Chem. Phys. **15**, 6025 (2013).

[381] B. Bukowski and N. A. Deskins, Phys. Chem. Chem. Phys. **17**, 29734 (2015).

[382] J. M. T. A. Fischer, M. Hankel, and D. J. Searles, J. Phys. Chem. C **119**, 29044 (2015).

[383] S. Zhuo, M. Shao, and S.-T. Lee, ACS Nano **6**, 1059 (2012).

[384] G. Guidetti, E. A. A. Pogna, L. Lombardi, F. Tomarchio, I. Polishchuk, R. R. M. Joosten, A. Ianiro, G. Soavi, N. A. J. M. Sommerdijk, H. Friedrich, B. Pokroy, A. K. Ott, M. Goisis, F. Zerbetto, G. Falini, M. Calvaresi, A. C. Ferrari, G. Cerullo, and M. Montalti, Nanoscale **11**, 19301 (2019).

[385] V. Jauja-Ccana, A. V. Córdova Huamán, G. T. Feliciano, and A. La Rosa-Toro Gómez, Comput. Mater. Sci. **195**, 110503 (2021).

[386] M. Anpo and J. M. Thomas, Chem. Commun. , 3273 (2006).

[387] J. Speight, *Lange's Handbook of Chemistry, 16th ed.* (McGraw-Hill Education: New York, 2005).

[388] X. Wang, X. Wang, J. Huang, S. Li, A. Meng, and Z. Li, Nat. Commun. **12**, 4112 (2021).

[389] X. Chen, J. Wang, Y. Chai, Z. Zhang, and Y. Zhu, Adv. Mater. **33**, 2007479 (2021).

[390] Z. Luo, X. Ye, S. Zhang, S. Xue, C. Yang, Y. Hou, W. Xing, R. Yu, J. Sun, Z. Yu, and X. Wang, Nat. Commun. **13**, 2230 (2022).

[391] Y. Guo, Q. Zhou, J. Nan, W. Shi, F. Cui, and Y. Zhu, Nat. Commun. **13**, 2067 (2022).

[392] V. Georgakilas, J. A. Perman, J. Tucek, and R. Zboril, Chem. Rev. **115**, 4744 (2015).

[393] V. Barone, O. Hod, and G. E. Scuseria, Nano Lett. **6**, 2748 (2006).

[394] H. Shi, A. S. Barnard, and I. K. Snook, Nanotechnology **23**, 065707 (2012).

[395] F. Liu, M.-H. Jang, H. D. Ha, J.-H. Kim, Y.-H. Cho, and T. S. Seo, Adv. Mater. **25**, 3657 (2013).

[396] J. Wu, W. Pisula, and K. Müllen, Chem. Rev. **107**, 718 (2007).

[397] Y. Yan, J. Chen, N. Li, J. Tian, K. Li, J. Jiang, J. Liu, Q. Tian, and P. Chen, ACS Nano **12**, 3523 (2018).

[398] Y. Li, H. Shu, S. Wang, and J. Wang, J. Phys. Chem. C **119**, 4983 (2015).

[399] T. L. Thompson and J. T. Yates, Chem. Rev. **106**, 4428 (2006).

[400] J. M. R. Narayanam and C. R. J. Stephenson, Chem. Soc. Rev. **40**, 102 (2011).

[401] D. Ravelli, S. Protti, and M. Fagnoni, Chem. Rev. **116**, 9850 (2016).

[402] J. Yang, P. Ganesan, J. Teuscher, T. Moehl, Y. J. Kim, C. Yi, P. Comte, K. Pei, T. W. Holcombe, M. K. Nazeeruddin, J. Hua, S. M. Zakeeruddin, H. Tian, and M. Grätzel, J. Am. Chem. Soc. **136**, 5722 (2014).

[403] S. S. Shin, J. H. Suk, B. J. Kang, W. Yin, S. J. Lee, J. H. Noh, T. K. Ahn, F. Rotermund, I. S. Cho, and S. I. Seok, Energy Environ. Sci. **12**, 958 (2019).

[404] Y. Ren, D. Sun, Y. Cao, H. N. Tsao, Y. Yuan, S. M. Zakeeruddin, P. Wang, and M. Grätzel, J. Am. Chem. Soc. **140**, 2405 (2018).

[405] B. G. McCarthy, R. M. Pearson, C.-H. Lim, S. M. Sartor, N. H. Damrauer, and G. M. Miyake, J. Am. Chem. Soc. **140**, 5088 (2018).

[406] B. J. Coe, J. Fielden, S. P. Foxon, J. A. Harris, M. Helliwell, B. S. Brunschwig, I. Asselberghs, K. Clays, J. Garín, and J. Orduna, J. Am. Chem. Soc. **132**, 10498 (2010).

[407] Z. Mi, T. Zhou, W. Weng, J. Unruangsri, K. Hu, W. Yang, C. Wang, K. A. I. Zhang, and J. Guo, Angew. Chem. Int. Ed. **60**, 9642 (2021).

[408] A. Kumari, I. Mondal, and U. Pal, New J. Chem. **39**, 713 (2015).

[409] M. Watanabe, H. Hagiwara, Y. Ogata, A. Staykov, S. R. Bishop, N. H. Perry, Y. J. Chang, S. Ida, K. Tanaka, and T. Ishihara, J. Mater. Chem. A **3**, 21713 (2015).

[410] N. Manfredi, M. Monai, T. Montini, M. Salamone, R. Ruffo, P. Fornasiero, and A. Abbotto, Sustain. Energy Fuels **1**, 694 (2017).

[411] H. Lai, X. Liu, F. Zeng, G. Peng, J. Li, and Z. Yi, ACS Omega **5**, 2027 (2020).

[412] J. Lee, J. Kwak, K. C. Ko, J. H. Park, J. H. Ko, N. Park, E. Kim, D. H. Ryu, T. K. Ahn, J. Y. Lee, and S. U. Son, Chem. Commun. **48**, 11431 (2012).

[413] M. Watanabe, H. Hagiwara, A. Iribe, Y. Ogata, K. Shiomi, A. Staykov, S. Ida, K. Tanaka, and T. Ishihara, J. Mater. Chem. A **2**, 12952 (2014).

[414] B. Cecconi, N. Manfredi, R. Ruffo, T. Montini, I. Romero-Ocaña, P. Fornasiero, and A. Abbotto, ChemSusChem **8**, 4216 (2015).

[415] N. Manfredi, M. Monai, T. Montini, F. Peri, F. De Angelis, P. Fornasiero, and A. Abbotto, ACS Energy Lett. **3**, 85 (2018).

[416] S. K. Choi, H. S. Yang, J. H. Kim, and H. Park, Appl. Catal. B: Environ. **121-122**, 206 (2012).

[417] W.-S. Han, K.-R. Wee, H.-Y. Kim, C. Pac, Y. Nabetani, D. Yamamoto, T. Shimada, H. Inoue, H. Choi, K. Cho, and S. O. Kang, Chem. Eur. J. **18**, 15368 (2012).

[418] A. Dessì, M. Monai, M. Bessi, T. Montini, M. Calamante, A. Mordini, G. Reginato, C. Trono, P. Fornasiero, and L. Zani, ChemSusChem **11**, 793 (2018).

[419] X. Zhang, T. Peng, L. Yu, R. Li, Q. Li, and Z. Li, ACS Catal. **5**, 504 (2015).

[420] R. A. Irgashev, A. A. Karmatsky, S. A. Kozyukhin, V. K. Ivanov, A. Sadovnikov, V. V. Kozik, V. A. Grinberg, V. V. Emets, G. L. Rusinov, and V. N. Charushin, Synth. Met. **199**, 152 (2015).

[421] R. Abe, K. Shinmei, K. Hara, and B. Ohtani, Chem. Commun. , 3577 (2009).

[422] R. Abe, K. Shinmei, N. Koumura, K. Hara, and B. Ohtani, J. Am. Chem. Soc. **135**, 16872 (2013).

[423] F. Yu, Z. Wang, S. Zhang, K. Yun, H. Ye, X. Gong, J. Hua, and H. Tian, Appl. Catal. B: Environ. **237**, 32 (2018).

[424] Y. Li, C. Sun, P. Song, F. Ma, N. Kungwan, and M. Sun, Sci. Rep. **8**, 10089 (2018).

[425] D. Jacquemin, E. A. Perpète, G. E. Scuseria, I. Ciofini, and C. Adamo, J. Chem. Theory Comput. **4**, 123 (2008).

[426] D. Casanova, F. P. Rotzinger, and M. Grätzel, J. Chem. Theory Comput. **6**, 1219 (2010).

[427] V. V. Divya and C. H. Suresh, New J. Chem. **44**, 7200 (2020).

[428] J. Preat, J. Phys. Chem. C **114**, 16716 (2010).

[429] B. Camino, M. De La Pierre, and A. M. Ferrari, J. Mol. Struct **1046**, 116 (2013).

[430] S. Jungsuttiwong, R. Tarsang, T. Sudyoadsuk, V. Promarak, P. Khongpracha, and S. Namuangruk, Org. Electron. **14**, 711 (2013).

[431] B. Xu, Y. Li, P. Song, F. Ma, and M. Sun, Sci. Rep. **7**, 45688 (2017).

[432] S. Meng, J. Ren, and E. Kaxiras, Nano Lett. **8**, 3266 (2008).

[433] J. Preat, D. Jacquemin, C. Michaux, and E. A. Perpète, Chem. Phys. **376**, 56 (2010).

[434] B. E. Hardin, H. J. Snaith, and M. D. McGehee, Nat. Photon. **6**, 162 (2012).

[435] P. H. Hahn, W. G. Schmidt, and F. Bechstedt, Phys. Rev. Lett. **88**, 016402 (2001).

[436] A. Marini, C. Hogan, M. Grüning, and D. Varsano, Comput. Phys. Commun. **180**, 1392 (2009).

[437] D. Sangalli, A. Ferretti, H. Miranda, C. Attaccalite, I. Marri, E. Cannuccia, P. Melo, M. Marsili, F. Paleari, A. Marrazzo, G. Prandini, P. Bonfà, M. O. Atambo, F. Affinito, M. Palummo, A. Molina-Sánchez, C. Hogan, M. Grüning, D. Varsano, and A. Marini, J. Phys. Condens. Matter **31**, 325902 (2019).

[438] G. Henkelman, A. Arnaldsson, and H. Jónsson, Comput. Mater. Sci. **36**, 354 (2006).

[439] C.-L. Fu and K.-M. Ho, Phys. Rev. B **28**, 5480 (1983).

[440] P. E. Blöchl, O. Jepsen, and O. K. Andersen, Phys. Rev. B **49**, 16223 (1994).

[441] R. Izsák and F. Neese, J. Chem. Phys. **135**, 144105 (2011).

[442] Y. Takano and K. N. Houk, J. Chem. Theory Comput. **1**, 70 (2005).

Publication

Articles in Scientific Journals

This thesis-related publications are marked by ‡

- ‡ A. Meier, **S. V. Badalov**, T. Biktagirov, R. Wilhelm, and W. G. Schmidt, Diquat based Dyes: A new Class of Photoredox Catalysts. (Submitted)
- ‡ **S. V. Badalov**, A Bocchini, A. L. Kozub, R. Wilhelm, U. Gerstmann, and W. G. Schmidt, Rutile, anatase, brookite and titania thin film from Hubbard corrected and Hybrid DFT. (Submitted)
- ‡ **S. V. Badalov**, R. Wilhelm, and W. G. Schmidt, Photocatalytic properties of graphene-supported titania clusters from density-functional theory. *J. Comput. Chem.* ***41**, 1921– 1930 (2020)*.
- **S. V. Badalov,** M. Yagmurcukardes, F. M. Peeters, and H. Sahin, Enhanced Stability of Single-Layer w-Gallenene through Hydrogenation. *The Journal of Physical Chemistry C* ***122** (49), 28302-28309 (2018)*.
- **S. V. Badalov**, A. Kandemir, H. Sahin, Monolayer AsTe$_2$: Stable Robust Metal in 2D, 1D and 0D. *ChemPhysChem*, ***19***, 2176 (2018).
- A. Kandemir, B. Akbali, Z. Kahraman, **S. V. Badalov**, M. Ozcan, F. Iyikanat, and H Sahin, Structural, electronic and phononic properties of PtSe$_2$: from monolayer to bulk. *Semicond. Sci. Technol.* **33** 085002 (2018).
- T. Ivek, R. Beyer, **S. Badalov**, M. Čulo, S. Tomić, J. A. Schlueter, E. I. Zhilyaeva, R. N. Lyubovskaya, and M. Dressel, Metal-insulator transition in the dimerized organic conductor κ−(BEDT-TTF)$_2$Hg(SCN)$_2$Br. *Phys. Rev. B* ***96**, 085116 (2017)*.
- A. I. Ahmadov, Sh. M. Nagiyev, C. Aydin, V. A. Tarverdiyeva, M. Sh. Orujova, and **S.V. Badalov**, Bound state solutions of Dirac equation: spin and pseudo-spin symmetry in the presence of the combined Manning-Rosen and Yukawa tensor potentials. *Eur. Phys. J. Plus* 137, 1075 (2022).
- V. H. Badalov and **S. V. Badalov**, Generalised *tanh*-shaped hyperbolic potential: Klein-Gordon equation's bound state solution. (Submitted)
- A. I. Ahmadov, S. M. Aslanova, M. Sh. Orujova, **S. V. Badalov**, Analytical Bound State Solutions of the Klein-Fock-Gordon Equation for the Sum of Hulthén and Yukawa Potential within SUSY Quantum Mechanics, *Adv. High Energy Phys.,* ***2021**, 8830063, (2021)*.
- A. I. Ahmadov, S. M. Aslanova, M. Sh. Orujova, **S. V. Badalov**, Sh. -H-. Dong, Approximate bound state solutions of the Klein-Gordon equation with the linear combination of Hulthén and Yukawa potentials. *Phys. Lett. A* ***383**, 24, 3010-3017 (2019)*.
- V. H. Badalov, H. I. Ahmadov, **S. V. Badalov**, Any l - state analytical solutions of the Klein-Gordon equation for the Woods-Saxon potential, *Int. J. Mod. Phys. E.* ***19**, 1463-14755, (2010)*.